Field observations of structurally-controlled rip currents on the west coast of Vancouver Island

by

Jamie Daniel
B.Sc., University of Victoria, 2023

A Thesis Submitted in Partial Fulfillment of the
Requirements for the Degree of

MASTER OF SCIENCE

in the School of Earth and Ocean Sciences

We acknowledge and respect the Lək̓ʷəŋən (Songhees and Xʷsepsəm/Esquimalt) Peoples on whose territory the university stands, and the Lək̓ʷəŋən and W̱SÁNEĆ Peoples whose historical relationships with the land continue to this day.

Field observations of structurally-controlled rip currents on the west coast of Vancouver Island

by

Jamie Daniel
B.Sc., University of Victoria, 2023

Supervisory Committee

Dr. Johannes Gemmrich, Co-Supervisor
(School of Earth and Ocean Sciences)

Dr. Jody M. Klymak, Co-Supervisor
(School of Earth and Ocean Sciences)

Dr. Stan Dosso, Outside Committee Member
(School of Earth and Ocean Sciences)

ABSTRACT

Rip currents are strong seaward-directed flows generated by the action of breaking waves on beaches. They are considered to be one of the most dangerous coastal hazards due to their ability to quickly transport swimmers and surfers into deeper waters. Since 1936, rip currents have been studied worldwide through a variety of methods including field observations, numerical modelling, and laboratory experiments. One location in Canada where rip currents occur is the Long Beach Unit of Pacific Rim National Park Reserve on the west coast of Vancouver Island. The Long Beach Unit is a popular surfing destination and rip currents at this location have necessitated water rescues and have been responsible for injuries and deaths. In spite of the hazard they pose, rip currents have been under-researched on Canada's west coast.

Field observations of rip currents were made at two locations in Pacific Rim National Park Reserve where rip currents are controlled by the presence of rock features: Long Beach and Wickaninnish Beach. Results from visual, Eulerian, and Lagrangian datasets are combined to examine the influence of the wave field and tide on rip current occurrence, speed, and perceived strength. It is found that significant wave height has the greatest effect on structurally-controlled rip current flow, followed by mean wave period. All three rip current characteristics increase with higher and longer waves, revealing the importance of incident wave energy and increased wave set-up in driving rip current flow. These waves can be represented by two non-standard wave parameters: wave factor W_f and a proxy variable for wave energy flux. Mean wave direction and directional spread show some influence on the rip currents at both locations, in that, during the observation periods, waves favourable for increased rip current speed and strength tended to approach the beaches from certain directions. At Wickaninnish Beach higher waves approached from west-southwest with greater directional spread; while at Long Beach higher and longer waves approached from the south with narrow directional spread. Tidal elevation and motion showed little influence on rip current characteristics at Wickaninnish Beach. Results from this research will contribute to general understanding of structurally-controlled rip currents, and can be used to further improve beach safety in Pacific Rim National Park Reserve.

Contents

List of Tables

List of Figures

ACKNOWLEDGEMENTS

I am extremely grateful for the support and guidance of my co-supervisors Dr. Johannes Gemmrich and Dr. Jody Klymak, and committee member Dr. Stan Dosso. I would also like to thank the Parks Canada Visitor Safety Team at Pacific Rim National Park Reserve, especially Randy Mercer and Alison Stacey, as well as Nick Haisch and Matt Beneka for all of their valuable knowledge and assistance with field work.

I am thankful for the love and support from my parents and my partner Ben during this process. A very special thanks to fellow grad students Becky Brooks, Lauryn Talbot, and Hayden Amidon for the amazing memories.

This research was funded through the Public Safety Canada Search and Rescue New Initiatives Fund (SAR NIF) and by Pacific Rim Ocean Data Mobilization and Technology (PRODIGY).

DEDICATION

To my parents, for encouraging my love of science.

Chapter 1

Introduction

1.1 Motivation

Rip currents are strong, seaward directed flows that begin near the shoreline and extend offshore through the surf zone. They can quickly transport surfers and swimmers into deeper waters and, as a result, are considered one of the most dangerous coastal hazards. It is estimated that from the years 1997 - 2016, rip currents were responsible for 81.9% of rescues on surfing beaches in the United States and for more than 100 fatal drownings each year (Brewster et al., 2019). Rip currents occur on beaches that are exposed to breaking waves and, as such, are found nearly worldwide (Austin et al., 2012; Gallop et al., 2018; Kim et al., 2011; Winter et al., 2014).

Observations and measurements of rip current flow have been made since 1936 (Shepard, 1936), and rip current field studies have since been conducted worldwide (Austin et al., 2012; Brander and Short, 2001; MacMahan et al., 2005). However, no field study examining rip current flow has been conducted on Canada's west coast. The Long Beach Unit of Pacific Rim National Park Reserve (PRNPR) in British Columbia consists of long sandy beaches exposed to swell from the Pacific Ocean and, as a result, is a popular year-round surfing destination. Rip currents occur at various locations along the beaches and have been responsible for water rescues, injuries, and deaths. Understanding the influence of the wave field and tidal conditions on rip current flow is important for preventing these incidents.

Historically, the majority of rip current studies have focused on channel rip currents primarily controlled by variations in bathymetry (e.g., Austin et al., 2014; MacMahan et al., 2005, 2010). The beaches in PRNPR are dissipative, long, sandy

beaches with geological features, including rocky outcrops. While multiple rip current types are present along these beaches, this research focuses on two locations in PRNPR where rip currents are controlled by irregular geological structures: a rocky outcrop at Wickaninnish Beach and a circular rock/islet known as Lovekin Rock at Long Beach. Neither of these structures are connected to the shore. Previous research on structurally-controlled rip currents has mainly consisted of regular, shore-connected structures such as groynes or breakwaters (Gourlay, 1974; Liu and Mei, 1976; Olsson and Pattiaratchi, 2009; Pattiaratchi et al., 2009; Scott et al., 2016) or naturally occurring headlands on embayed beaches (Castelle and Coco, 2012, 2013; Mouragues et al., 2020a, 2020b), which differ from the characteristics of the structures in PRNPR. The shadow rip current at Wickaninnish Beach is of particular interest. Although the number of studies examining structurally-controlled rip currents has increased through the 2010's, of the two types of structurally-controlled rip currents, deflection and shadow rips, there have been fewer studies of shadow rip currents in the field (Castelle et al., 2016). The aim of this research is to improve the understanding of structurally-controlled rip current behaviour in PRNPR.

1.2 Theory

1.2.1 Rip Current Generation

The primary mechanism for rip current generation is variation in breaking wave height in the surf zone, which is defined as the region between the first line of breaking waves and the shoreline (Figure 1.1) (Thomson, 1981). As water depth decreases towards shore, waves begin to break and their energy and momentum are dissipated. The motion of the incident surface waves is transformed into small scale turbulence, steady flows, low-frequency waves, and large-scale vortical motions (Battjes, 1988). Rip currents and longshore currents are two of the main features of the surf zone driven by incident wave motion (Peregrine, 1998).

Radiation stress is defined as the 'excess flow of momentum due the presence of waves' (Longuet-Higgins and Stewart, 1964), and is equivalent to the transport of wave-induced momentum (Holthuijsen, 2007). For a coordinate system where x and y are the coordinates perpendicular and parallel to the shoreline, respectively, with x increasing shoreward, the components of the radiation stress tensor S for waves approaching at an angle θ relative to shore-normal are given as

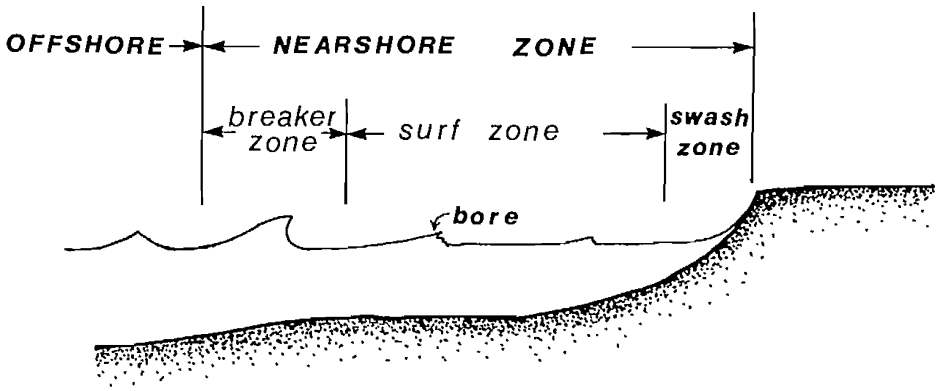

Figure 1.1: Nearshore region including the surf zone and the breaker zone. From Thomson (1981).

$$
\begin{aligned}
S_{xx} &= E\left(n - \frac{1}{2} + n\cos^2\theta\right) \\
S_{yy} &= E\left(n - \frac{1}{2} + n\sin^2\theta\right) \\
S_{xy} &= S_{yx} = En\cos\theta\sin\theta.
\end{aligned} \tag{1.1}
$$

In these equations n is given by

$$
n = \frac{1}{2}(1 + \frac{2kh}{\sinh(2kh)}) \tag{1.2}
$$

where h is the water depth and $k = 2\pi/\lambda$ is the wave number. E is the wave energy density given by:

$$
E = \frac{1}{8}\rho g H^2 \tag{1.3}
$$

where ρ is the water density, g is the acceleration due to gravity, and H is the wave height.

In the shallow-water limit, $kh \to 0$,$n \to 1$. The radiation stress tensor then becomes

$$
\begin{aligned}
S_{xx} &= E\left(\frac{1}{2} + \cos^2\theta\right) \\
S_{yy} &= E\left(\frac{1}{2} + \sin^2\theta\right) \\
S_{xy} &= S_{yx} = E\cos\theta\sin\theta.
\end{aligned} \tag{1.4}
$$

Since momentum transport by waves is equivalent to a stress, horizontal variations in radiation stress act as forces on the water, which can result in mean sea level changes and generate surf zone currents (Holthuijsen, 2007). When waves approach the shore, they shorten, steepen, and break when the ratio of wave height to water depth reaches a critical value γ (Bowen, 1969). A distinction is made between the region outside of the surf zone (the seaward region) and the region inside of the surf zone (the shoreward region). This distinction is justified if the assumption is made that the beach slope is small enough to neglect any energy reflected from the approaching waves (Longuet-Higgins and Stewart, 1964). In the surf zone, energy is dissipated due to breaking waves and S_{xx} decreases towards the shore. In this case, the resulting force is directed towards the shore and is balanced by a raising of the

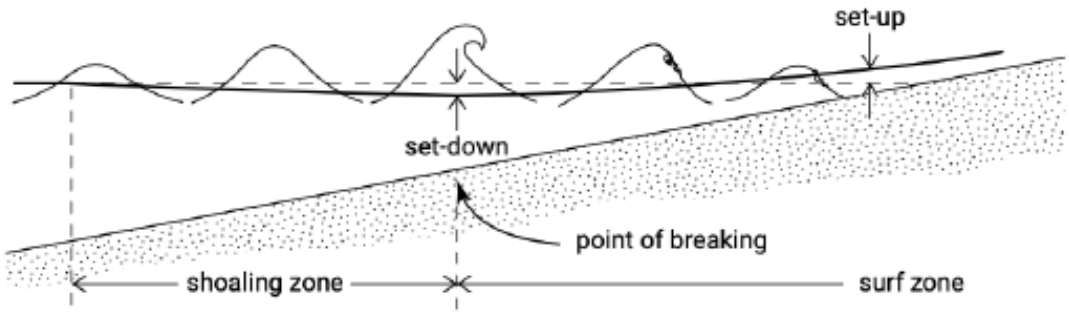

Figure 1.2: Wave set-up and set-down in the nearshore region. The solid line shows the set-down and set-up relative to the mean water level which is shown by the dashed line. From Bosboom and Stive (2023).

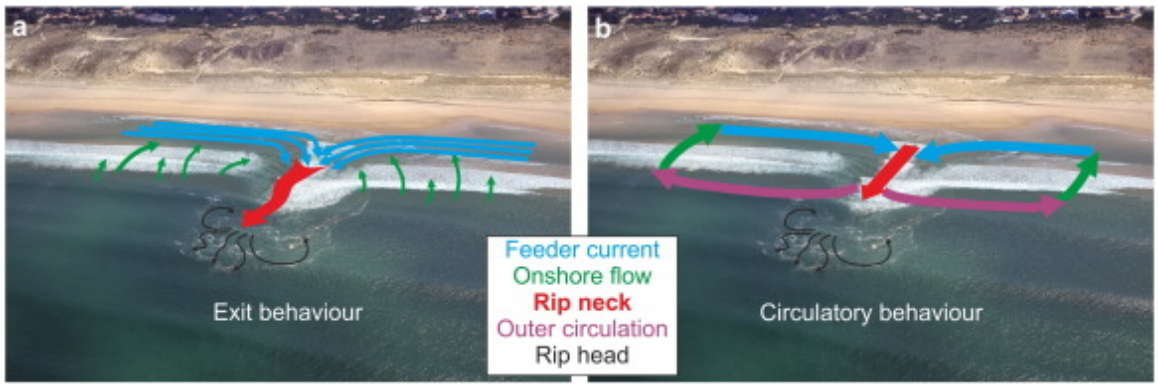

Figure 1.3: Rip current circulation. Exit behaviour is shown in (a) and circulatory behaviour is shown in (b). From Castelle et al. (2016).

mean sea level known as set-up (Figure 1.2) (Bowen, 1969).

Alongshore variations in breaking wave height result in alongshore variations in radiation stress, which causes circulation in the surf zone (Bowen and Inman, 1969; MacMahan et al., 2006). Set-up is related to breaking wave height (Bosboom and Stive, 2023). Regions with higher breaking waves will have higher set-up than regions with lower breaking waves. The resulting longshore pressure gradient causes longshore currents that flow from the regions of high set-up (higher waves) to the regions of lower set-up (lower waves). The longshore currents converge at regions of low waves and then flow offshore through the surf zone as a rip current (Bowen and Inman, 1969; MacMahan et al., 2006) (Figure 1.3).

Rip currents are often visible as gaps between breaking waves, where the water is sometimes darker due to offshore sediment transport (Leatherman, 2017). This seaward-flowing region of water, known as the rip neck (Figure 1.3, red line), can

reach speeds of up to 2 m/s (Short, 1985). From the rip neck, the rip current system can either travel fully through the surf zone and beyond or remain within the surf zone as semi-enclosed vortices (Castelle et al., 2016; Dalrymple et al., 2011). Once a rip current extends beyond the surf zone, the rip neck slows and dissipates into the rip "head" (Figure 1.3), which often contains foamy water, another identifiable rip current characteristic (Leatherman, 2017).

The variations in breaking wave height that generate rip current flows can be caused by bathymetric variations, hydrodynamic variations, or the presence of structures, resulting in three main rip current types: hydrodynamically-controlled (transient), bathymetrically-controlled, and structurally-controlled (Castelle et al., 2016; Dalrymple et al., 2011).

Rip currents controlled by bathymetry persist in time and location, and usually occur in channels between sandbars on beaches with variable morphology (Castelle et al., 2016). Hydrodynamically-controlled (transient) rip currents tend to occur on beaches that are uniform in the alongshore direction, varying with both time and location (Johnson and Pattiaratchi, 2004). Structurally-controlled rip currents occur along the boundaries of rigid natural (headlands, rock outcrops) or anthropogenic (breakwaters, groynes) structures and are persistent in location (Castelle et al., 2016). Deflection rips occur on the up-wave side of the structure and result from longshore currents that are deflected offshore by the structure (Figure 1.4 bottom). Shadow rips occur on the down-wave side of the structure (Figure 1.4 top). As waves approach the structure and break, wave heights, and the resulting set-up, are much lower in the lee, or shadow, of the structure than outside of this region. This drives a longshore current towards the structure and the resulting rip current flows offshore (Gourlay, 1974; Pattiaratchi et al., 2009). The up-wave and down-wave sides of a specific structure depend on the direction of incident waves relative to the structure. As a rip current persists against a structure, it can create a channel along the structure, resulting in a mixed boundary-channel rip (Castelle et al., 2016).

The traditional view of rip circulation is that of a narrow offshore flow that slows down once beyond the breaking waves. This is known as 'exit behaviour' (Figure 1.3a). The development of global positioning system (GPS) equipped surf zone drifters for observational studies (Johnson and Pattiaratchi, 2004; MacMahan et al., 2010; Schmidt et al., 2003), has allowed improved observations of rip current circulation and shown that rip current flow may also remain in the surf zone as semi-enclosed vortices, known as 'circulatory behaviour' (Figure 1.3b). In this case, the

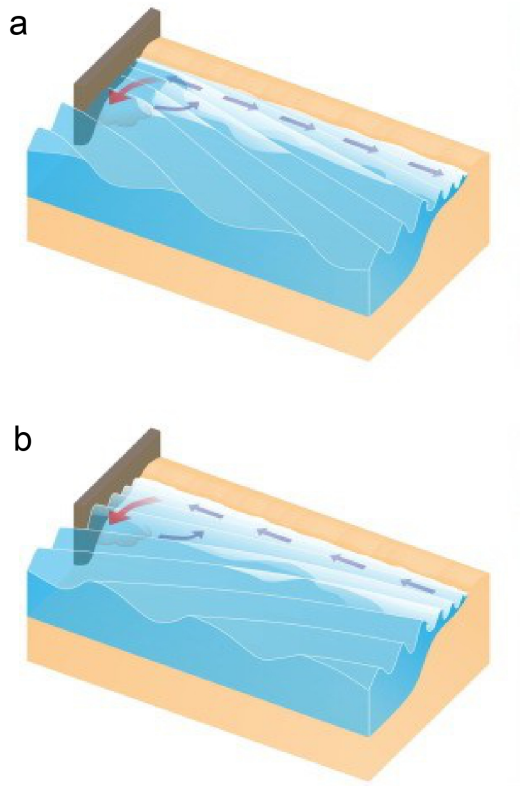

Figure 1.4: Structurally-controlled rip currents. A shadow rip is shown in (a) and a deflection rip is shown in (b). From Castelle et al. (2016).

flow may also occasionally exit the surf zone. Rip behaviour can inform rip escape strategy. When a rip current shows exit behaviour, the traditional escape strategy is to swim perpendicular to the rip (parallel to the beach) (Castelle et al., 2016). With rip currents that show circulatory behaviour, the promoted escape strategy is to float in the rip current until the rip re-circulates back into shallower water (MacMahan et al., 2010). Rip current circulation may vary between exit and circulatory behaviour, which has been found to be controlled by the tidal phase and wave field (Gallop et al., 2018; MacMahan et al., 2010; Mouragues et al., 2020b; Scott et al., 2014).

1.2.2 Wave and Tidal Influences

It has been found that rip current speed or intensity increases with increasing wave height for bathymetrically-controlled (Dusek and Seim, 2013; MacMahan et al., 2005; Moulton et al., 2017; Scott et al., 2018; Winter et al., 2014), transient (Castelle et al., 2014), and structurally-controlled (Pattiaratchi et al., 2009; Scott et al., 2016) rip currents. Increasing peak period values also result in stronger structurally-controlled rips but this influence is less significant than that of increasing wave height (Pattiaratchi et al., 2009). Wave height can also influence rip circulation behaviour, with higher waves resulting in more circulatory cell behaviour (Gallop et al., 2018; MacMahan et al., 2010).

The intensity of bathymetrically-controlled (Criado-Sudau et al., 2019; Dusek and Seim, 2013; MacMahan et al., 2005; Moulton et al., 2017) and transient (Johnson and Pattiaratchi, 2004; Scott et al., 2018) rips increases when waves approach the beach more shore-normal. For structurally-controlled rips, however, Scott et al. (2016) found that rip current flow along a groyne was stronger when waves approached from a larger angle relative to shore-normal; however, this influence was less than that of increasing wave height. Incident wave angle may also control the rip circulation. Mouragues et al. (2020b) found that a headland rip showed mainly exit behaviour when waves approached the beach shore-normal. When the waves approached at oblique angles, the rip was either a deflection rip against the headland or showed circulatory behaviour. Castelle and Coco (2012) found that the presence of a headland rip on an embayed beach increased with greater directional spreading of the wave field.

The influence of the tide on bathymetrically-controlled rip currents has been well documented, with the strongest rip current speeds occurring at or around low-tide (Austin et al., 2012; Brander and Short, 2001; MacMahan et al., 2005; Moulton

et al., 2017). On beaches with bar-rip morphology, low-tide conditions tend to expose sandbars to wave breaking, maximizing wave dissipation over the sandbars and driving stronger rip flow (Austin et al., 2010; Winter et al., 2014). Tidal modulation of transient rip currents has also been observed. Castelle et al. (2014) found that transient rip currents were observed more often at low tide and Murray et al. (2013) found a greater number of transient rips occurred during a falling tide than a rising tide. Tidal effects on structurally-controlled rip currents are less well documented. McCarroll et al. (2014) found that on an embayed beach with headland rip currents, rip speed increased towards low tide. Scott et al. (2016) has noted that changes in water level due to tidal phase may influence some key parameters affecting structurally-controlled rip currents such as structure length, surf zone width, or the incoming wave field. In some cases the low-tide water level may leave the structure dry.

Chapter 2

Site and Methods

2.1 Study Location

The Long Beach Unit of Pacific Rim National Park Reserve (PRNPR) is located on the west coast of Vancouver Island between the towns of Tofino and Ucluelet (Figure 2.1), exposed to Pacific Ocean swell. The dominant swell direction varies seasonally and is determined by the prevailing wind direction; with west-northwest swells dominating during the summer and west-southwest swells dominating during the winter (Thomson, 1981). Wave heights are also higher during winter. This region of Vancouver Island's coast experiences a mesotidal semidiurnal mixed tide. The Long Beach Unit of PRNPR is made up of 16 kilometres of dissipative sandy beach and is a popular surfing and tourist destination.

This research focuses on structurally-controlled rip currents at two locations in the Long Beach Unit: Wickaninnish Beach at the south end of the beach and Long Beach at the north end (Figure 2.2). At Wickaninnish Beach, a shadow rip current occurs along a group of offshore rocks at the far south end of the beach in front of the K^{w}isitis Visitor Centre (KVC) (Figure 2.4). At Long Beach, a rip current occurs in front of and along an offshore circular rock, or islet, known as Lovekin Rock (Figure 2.3). At very low tides, it is briefly possible to walk out to Lovekin Rock. Both structures are natural, irregular structures that are not shore-connected and have been the locations of rip-related rescues, injuries, and deaths.

Figure 2.1: Map showing the study region and locations of Wickaninnish and Long Beach in the Long Beach Unit of Pacific Rim National Park Reserve.

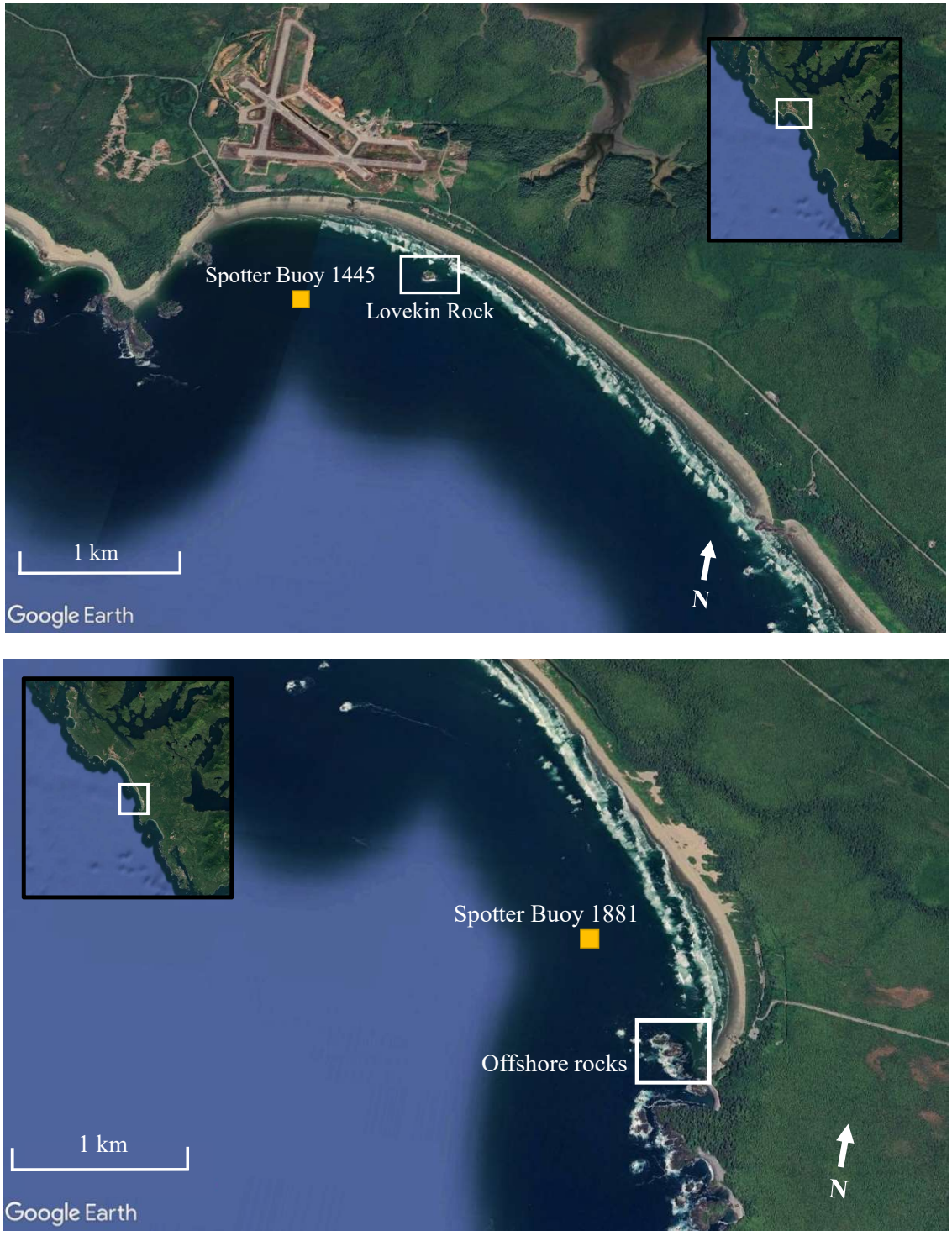

Figure 2.2: Satellite images of Long Beach (top) and Wickaninnish Beach (bottom). The orange squares show the locations of the Spotter wave buoys. The locations of Lovekin Rock and the offshore rock at Wickaninnish Beach are also shown.

Figure 2.3: Satellite image of Long Beach showing Lovekin Rock. The red arrows show the location of the rip current. The orange square shows the location of Spotter buoy 1445.

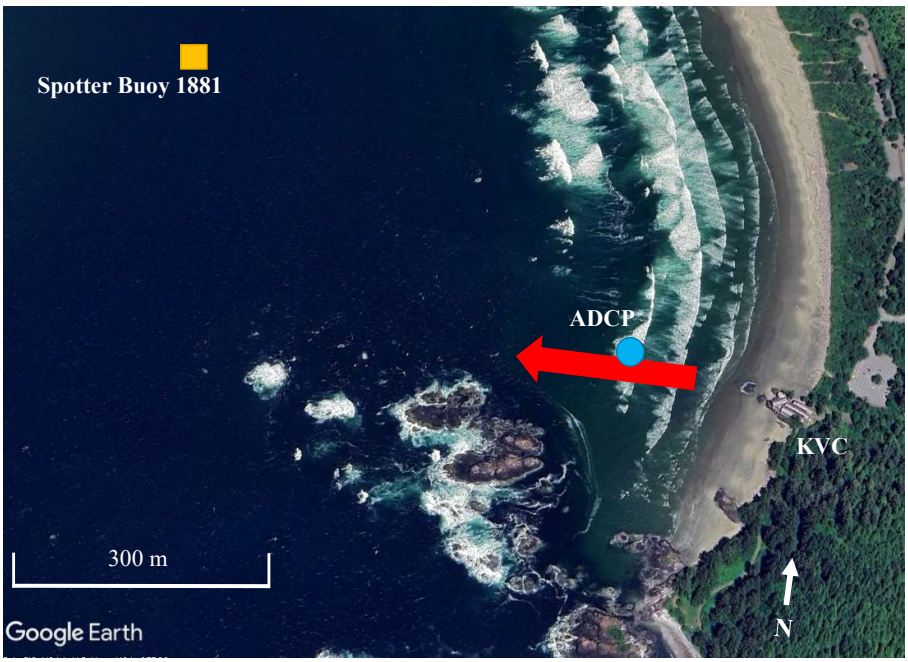

Figure 2.4: Satellite image of Wickaninnish Beach showing the offshore rocks. The red arrow shows the location of the rip current. The orange square shows the location of Spotter buoy 1881 and the blue circle shows the location of the ADCP. The location of the K^{w}isitis Visitor Centre (KVC) is also indicated.

2.2 Methods

Observations at Wickaninnish and Long Beach spanned July 2022 to August 2025 and consisted of visual, Eulerian, and Lagrangian methods. Visual observational methods took place at both locations. At Wickaninnish Beach long-term video observations were made with an infrared camera set up at KVC overlooking the beach, while twice-daily observations of the perceived strength of the Lovekin Rock rip current at Long Beach were provided by the Parks Canada Coastal Steward Program. The two Lagrangian methods also took place at Long Beach. Surf zone drifters were deployed 15 times throughout July 2024 and on 8 August 2025 at Lovekin Rock. The last drifter deployment was also accompanied by a dye release done in close collaboration with Parks Canada. At Wickaninnish Beach a Nortek Signature 1000 Acoustic Doppler Profiler (ADCP) was deployed for three weeks in October and November of 2023 to obtain Eulerian measurements of rip current speed. The location of the ADCP during the deployment is shown in Figure 2.4. Wave parameters were obtained from two Spotter wave buoys (SOFAR Ocean), each located approximately 1 km offshore of Long Beach (Figure 2.2 top) and Wickaninnish Beach (Figure 2.2 bottom) Data coverage of each observational method is shown in Figure 2.5.

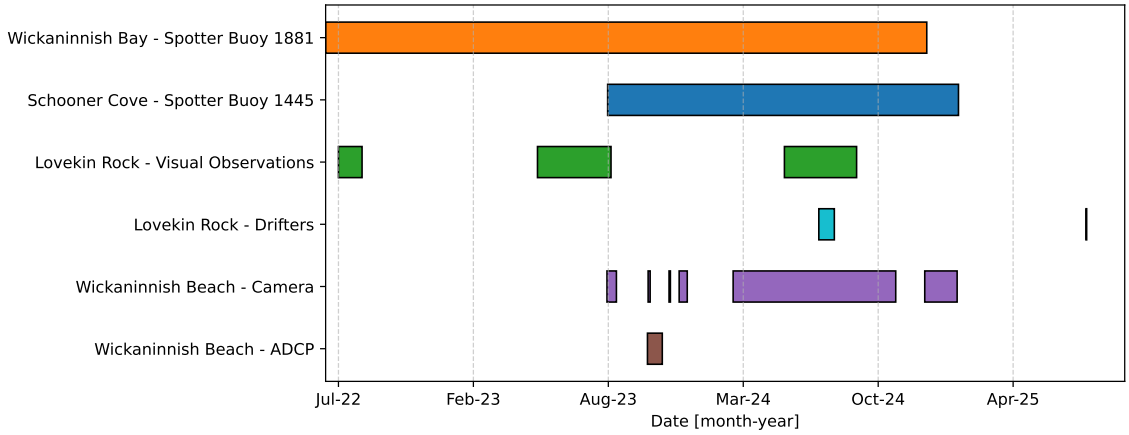

Figure 2.5: Data coverage of the observational methods.

2.2.1 Wave Buoys

Bulk wave parameters were calculated using displacement data from two Spotter buoys (SOFAR Ocean) located at Long Beach (Figure 2.3) and Wickaninnish Beach

(Figure 2.4) in 8 m water depth.

The Spotter buoys sample at 2.5 Hz and output the raw horizontal and vertical displacement data (x, y, z), which are divided into hourly segments. Wave spectra are then calculated for each segment using the Welch method with a Hanning window of length 1024 with a 50% overlap. A low frequency cutoff of 0.04 Hz (25 s) was applied to remove low frequency noise. Significant wave height, peak and mean spectral period, mean direction, directional spread, and wave steepness are then calculated from each hourly spectrum.

2.2.2 Infrared Camera

An infrared camera was mounted on the exterior of KVC overlooking the offshore rocks and the rip current at Wickaninnish Beach (Figure 2.4). Excluding power outages, the camera was recording 24 hours a day. Analysis of the images was based on the time exposure (timex) technique of Lippmann and Holman (1989). Videos were recorded in 10-minute segments. Each segment was then averaged to create one image. Rip currents were visually identified as regions of low intensity between the higher intensity regions of breaking waves.

Each image was examined and then sorted into one of three categories: rip events, non-rip events, and undefined or rejected images. For an image to be considered in the analysis, the offshore rocks, the waterline on shore, and the horizon all had to be clearly visible. If any one of these features were not visible then the image was rejected and not used in further analysis. Figure 2.6 (H-J) shows examples of rejected images. The quality of visibility of the infrared camera is dependent on the difference between the air and water temperatures and, as such, is dependent on the atmospheric conditions. It is likely that the poor image quality in the rejected images is caused by increased relative humidity (RH) during the times when these images occur. In the set of rejected images there were six days that had no usable images: 2024-07-29, 2024-07-30, 2024-08-03, 2024-09-18, 2024-09-23, and 2024-09-24. These days all had exceptionally high RH, with the daily average RH exceeding 97%, as recorded at the weather station near Tofino airport operated by NAV Canada (ECCC, n.d.). The increased water vapour content in air with high RH absorbs and scatters the infrared signal, which results in reduced image quality. Compared to the full set of images, the rejected images do not appear to occur during specific wave conditions (Figure 2.7).

Images with good visibility were then examined in order to identify rip and non-rip

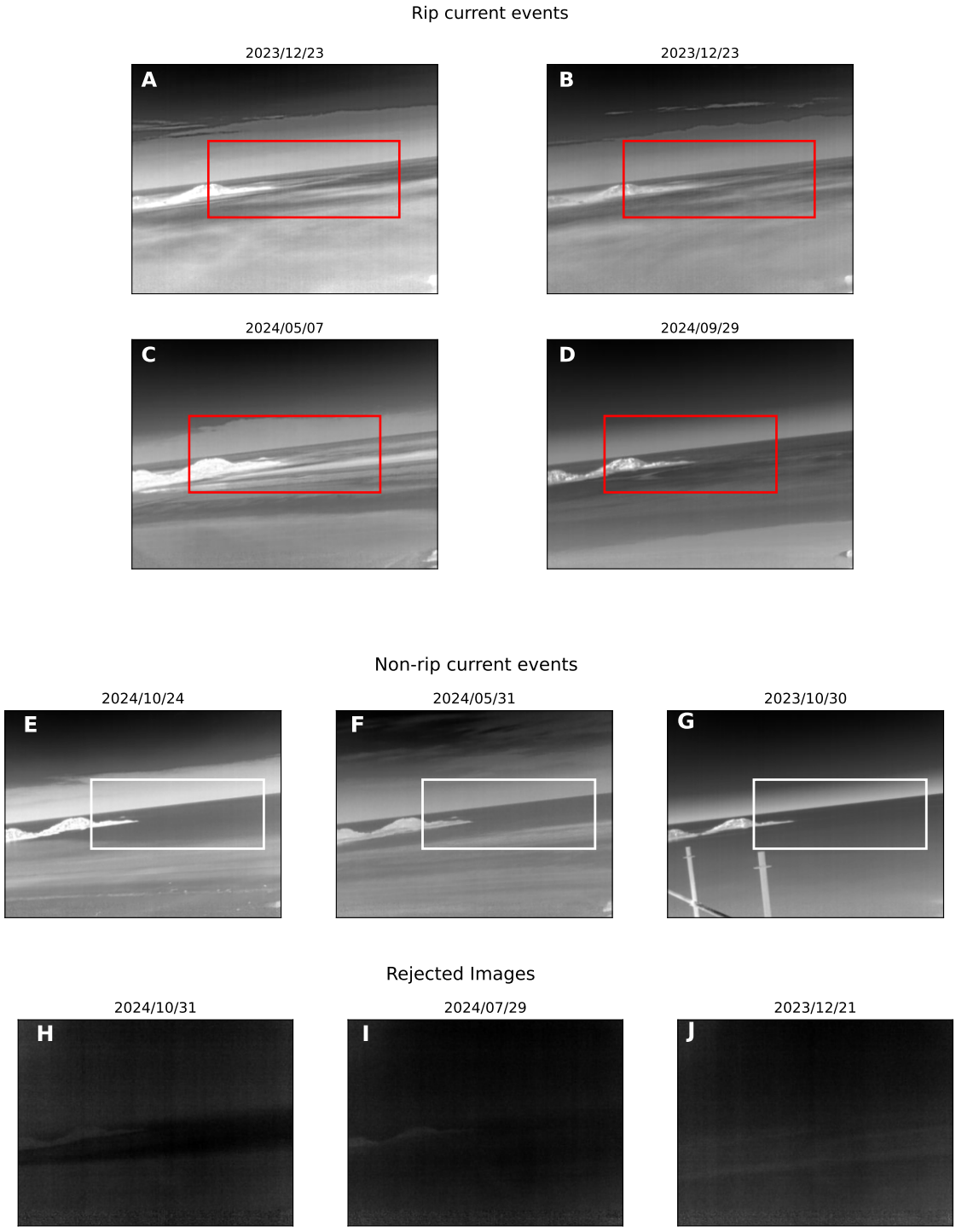

Figure 2.6: Infrared camera images at Wickaninnish Beach from each of the three categories: rip current events (A-D), non-rip current events (E-G), and rejected images (H-J). The red boxes in A-D show regions near the offshore rocks where variations in light intensity indicate the presence of a rip current. The white boxes in E-G show similar regions where no variations in light intensity are seen. Note in G that scaffolding on the side of the KVC is visible in the bottom left of the image, but out of the region of interest.

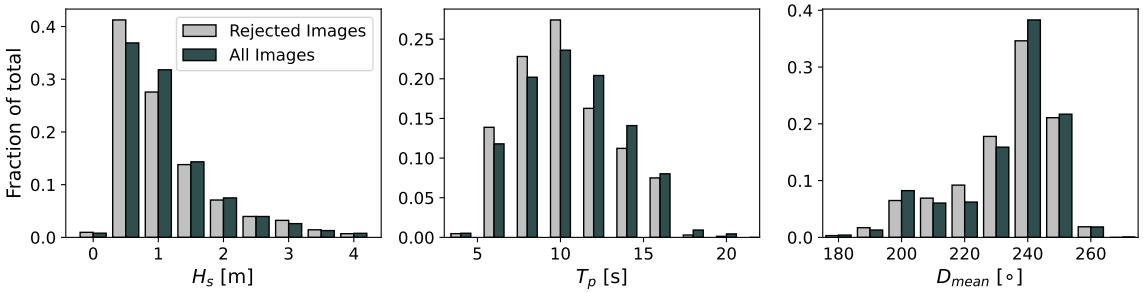

Figure 2.7: Normalised histograms of distributions of the full set of images (dark green) and the rejected images (grey) for significant wave height (left), peak wave period (middle), and mean wave direction (right) from Spotter buoy 1881 at Wickaninnish Beach during the observational period.

events. Since the rip current at Wickaninnish Beach occurs near the offshore rocks, the region alongside and slightly in front of the rocks (shown by the red box in Figure 2.6A-D and the white box in Figure 2.6 E-G) was examined closely for variations in light intensity that would indicate the presence of a rip current. Figure 2.6 (A-D) shows examples of images classified as rip events since variations in light intensity are seen in the region near the rocks that would indicate the presence of a rip current. Figure 2.6 (E-G) shows examples of images classified as non-rip events since no variation in light intensity is seen in the region near the rocks.

Images were collected from late August 2023 to the end of January 2025 with gaps during the following dates: 12 September - 29 October 2023, 1 - 29 November 2023, 1 - 14 December 2023, 24 Dec 2023 - 3 May 2024, and 30 Oct - 12 Dec 2024. Some of these gaps were due to power outages. Approximately 300 days of data were collected, with a total of 33127 images. Since the undefined category consists of 12126 images, 21001 images were left to be used in the analysis.

Rip current occurrence probability P_{rip} was defined as the number of rip events divided by the total number of observations (images). Each wave parameter was divided into N equally weighted bins. In each bin, the number of rip events x_{rip} is represented by the binomial distribution

$$f(x_{rip}) = \binom{n}{x_{rip}} P^{x_{rip}} Q^{n-x_{rip}} \tag{2.1}$$

where n is the number of observations in each bin, P_{rip} is the probability of success (a rip event) in each bin, and $Q = 1 - P_{rip}$ is the probability of failure (a non-rip event) in each bin.

The probability of success P_{rip} is calculated for each bin as

$$P_{rip} = \frac{x_{rip}}{n}. \tag{2.2}$$

The 95% confidence interval CI for each bin is found as

$$CI = P_{rip} \pm 1.96SE \tag{2.3}$$

where SE is the standard error of P_{rip}, which is equal to $\sqrt{Var(P_{rip})}$.

The variance of x_{rip}, the number of success in each bin, is

$$Var(x_{rip}) = nP_{rip}Q = nP_{rip}(1 - P_{rip}). \tag{2.4}$$

The variance of $P_{rip} = \frac{x_{rip}}{n}$ can then be found as

$$Var(P_{rip}) = Var(\frac{1}{n}x_{rip}) = \frac{1}{n^2}Var(x_{rip}) = \frac{1}{n^2}nP_{rip}(1-P_{rip}) = \frac{P_{rip}(1-P_{rip})}{n}. \quad (2.5)$$

The standard error SE is then calculated as

$$SE = \sqrt{Var(P_{rip})} = \sqrt{\frac{P_{rip}(1-P_{rip})}{n}}. \quad (2.6)$$

2.2.3 ADCP

A Nortek Signature 1000 Acoustic Doppler Current Profiler (ADCP) was deployed in the surf zone at Wickaninnish Beach from 29 October to 19 November 2023 (Figure 2.4). During spring tide, the ADCP was dry at low tide and in approximately 3 m deep water at high tide. During the deployment the ADCP gradually sank into the sand and was fully submerged by the time it was retrieved. By comparing the pressure measurements from the ADCP to the tidal data from the WebTide Tidal Prediction Model (Oakey et al., n.d.) it was determined that the ADCP began to sink into the sand after 9 November 2023 (Figure 2.8). Data from 29 October - 9 November 2023 were used in the analysis.

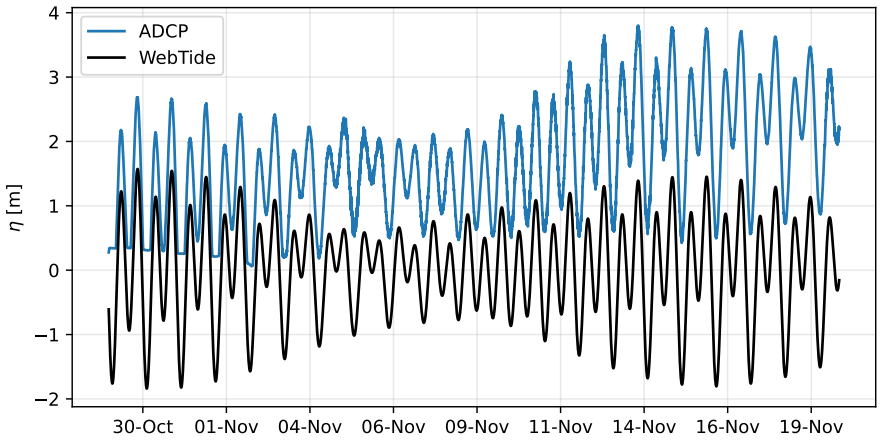

Figure 2.8: Time series of water level η from ADCP and WebTide Tidal Prediction Model for the ADCP deployment. Note that the ADCP is out of the water during the spring low tides.

The ADCP has two different sampling methods. The averaged method samples and averages data across five minutes at the top of the hour, five minutes later, the half hour, and five minutes later. The alt-averaged method samples and averages data across two minutes every five minutes between the averaged format (Figure 2.9). Velocity measurements are made in 20 cm depth bins.

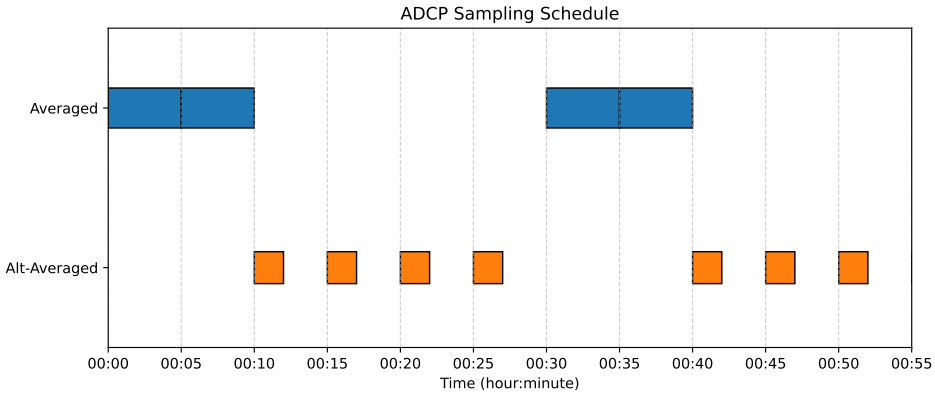

Figure 2.9: ADCP sampling schedule over one hour. The alt-averaged data are sampled at 1 Hz for two minutes. The averaged data are returned as the average over the 5 minutes of sampling.

The data obtained from these two sampling methods were combined to obtain velocity and pressure data with a regular five minute sampling period. Both datasets are measured in compass north and east directions. Data were converted to a beach coordinate system, defined such that x is the alongshore direction (positive north along the beach) and y is the cross-shore direction (positive offshore). The following equations were used to rotate the compass coordinates to the beach coordinate system:

$$u_b = v_c \sin(\theta) - u_c \cos(\theta) \quad v_b = u_c \sin(\theta) + v_c \cos(\theta) \tag{2.7}$$

where u_c and v_c are the east and north velocities in the compass coordinate system, u_b and v_b are the cross-shore and along-shore velocities in the beach coordinate system, and θ is the angle between the along-shore direction and north, which is 18 $^\circ$ for Wickaninnish Beach (Figure 2.10).

The ADCP velocity data were further processed to change the frame of reference. The reference frame for the raw data is such that 0 m is at the seabed where the ADCP is located and the water surface changes with the tidal motion (Figure 2.11A). Measurements above the tidal elevation were removed (Figure 2.11B) and the velocity

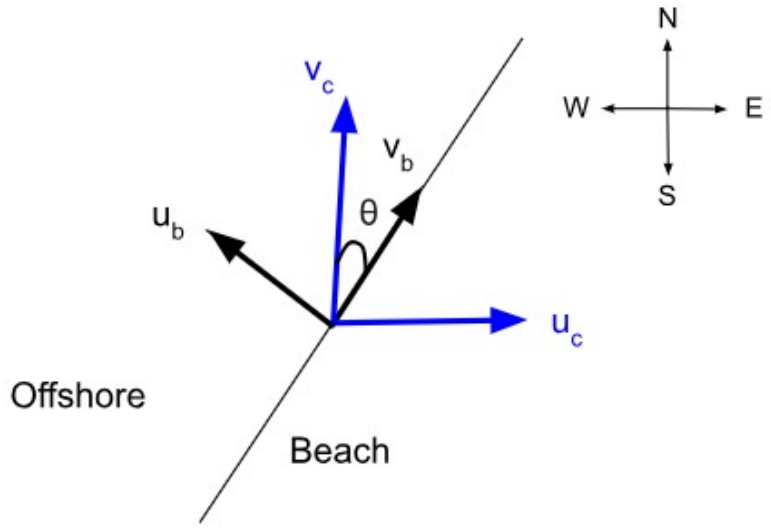

Figure 2.10: ADCP coordinate transformation. v_c and u_c are the horizontal velocities in the compass coordinate system. v_b and v_b are the horizontal velocities in the beach coordinate system. θ is the angle between the coastline of Wickaninnish Beach and north.

measurements were re-mapped so that the water surface is at a constant value of 0 m and depth increases downwards, changing with the tide (Figure 2.11C).

The depth-averaged cross-shore U and alongshore V velocities were calculated for the analysis as

$$U = \frac{1}{h}\sum_{0}^{h} u_z \Delta z \quad V = \frac{1}{h}\sum_{0}^{h} v_z \Delta z \tag{2.8}$$

where h is the water depth, and u_z and v_z are the cross and alongshore velocities in each depth bin, respectively. Δz is the resolution of the depth bins and is 20 cm. The depth range was limited to 0 - 1.6 m.

2.2.4 Observations of Perceived Rip Current Strength

Estimates of rip current strength by lifeguards have been shown by Dusek and Seim (2013) and Reinhart and Pfaff (2016) to be an effective alternative to instrument observations. There are no lifeguards on the beaches in PRNPR; however, the Parks Canada Coastal Stewards are present on the beach during the summer months to promote coastal and visitor safety. As part of the program, observations of the Lovekin Rock rip current are recorded throughout the summer season (May to September).

These observations were provided to this research.

The estimated strength of the rip current was recorded twice daily during the summer months of 2022 - 2024 for a total of 476 observations. The observations are rated on the following scale:

0. Low
1. Moderate
2. Considerable
3. High

Perceived rip current strength is based on several factors, including the visibility of the rip current, how easily people or objects are pulled into the rip current, the number of rescues, and input from local experienced surfers and instructors. The average rip conditions across a three hour period are reported each day. The morning conditions are recorded for 09:00 - 12:00 and the afternoon conditions for 12:00 - 15:00.

The probability of a strong rip current was defined as the probability of the perceived strength rating exceeding moderate, or $P(S_p \geq 2)$. Similarly to the distribution of rip occurrence probability in Section 3.2.1, $P(S_p \geq 2)$ can be represented by a binomial distribution where a success is defined by $S_p \geq 2$ (a considerable-high strength rip current) and a failure is defined as $S_p < 2$ (a low-moderate strength rip current).

Each wave parameter was divided into N equally weighted bins. $P(S_p \geq 2)$ and the 95% confidence interval CI were calculated for each bin as follows:

$$P(S_p \geq 2) = \frac{x_{\geq 2}}{n}, \quad SE = \sqrt{\frac{P(S_p \geq 2)(1 - P(S_p \geq 2))}{n}}, \quad CI = P(S_p \geq 2) \pm 1.96SE \tag{2.9}$$

where n is the number of observations in each bin and $x_{\geq 2}$ is the number of observations of $S_p \geq 2$.

2.2.5 Surf Zone Drifters

Lagrangian surf zone drifters were deployed into the Lovekin Rock rip current to obtain measurements of the rip velocity and map the rip current flow. The drifters

were developed by the UVic Faculty of Science's Electronics Shop, based on the microSWIFT drifters designed and used by Rainville et al. (2023). The majority of the original design elements was kept, with a few changes made due to budgeting or availability of materials. A GPS and inertial measurement unit (IMU) are housed in a Nalgene brand water bottle (Figure 2.12). Raw data files are saved every 20 minutes and stored on an internal SD card so that the data can be downloaded after each drifter deployment. The GPS data is used to map the drifters' location and to calculate their speed in the rip current.

The drifters were deployed at Lovekin Rock throughout July 2024 and on 8 August 2025. In 2024 a total of 15 drifter releases were made, with two days of focused data collection on 30 and 31 July across periods of 6 hours (from 16:00 - 22:00 UTC). The drifters were released directly into the rip current from a surfboard by an experienced surf instructor. Six drifters were released from 16:30 - 18:00 UTC on 8 August 2025. The drifters were released by hand into the surf zone and either washed up on shore or were collected by an experienced surfer.

2.2.6 Dye Releases

In collaboration with Parks Canada, fluorescent dye was released into the rip current at Lovekin Rock on 8 August 2025. The dye was used to visualise the rip current flow around Lovekin Rock, and for comparison with results from the surf zone drifters. Aerial videos of the dye were filmed by a drone.

2.3 Analysis

For each observational method, the correlation of rip current occurrence, speed, and strength with spectral wave parameters and tidal elevation/motion was examined. Wave parameters were provided by the nearshore Spotter wave buoys at Wickaninnish Beach and Schooner Cove. Tidal data were obtained from the WebTide Tidal Prediction Model (Oakey et al., n.d.). The tidal elevation data measured by the ADCP were also used in the analysis of the ADCP data.

The bulk spectral wave parameters examined are listed in Table 2.1.

The moments of the wave spectrum $E(f)$ are defined as

$$m_n = \int_0^\infty f^n E(f) df \quad n = \ ..., -1, 0, 1, ... \tag{2.10}$$

Parameter	Description
H_s	Significant wave height
T_p	Peak wave period
T_{01}	Mean spectral wave period
D_{mean}	Mean wave direction
σ	Directional spreading
H_s/λ_p	Peak wave steepness

Table 2.1: Description of bulk wave parameters tested in analysis.

and significant wave height is calculated using the zeroth moment of the wave spectrum m_0 as

$$H_s = 4\sqrt{m_0}. \tag{2.11}$$

Peak wave period is calculated using the weighted mean method described by Young (1995), with $q = 4$

$$T_p = \frac{\int_0^\infty E^4(f)df}{\int_0^\infty fE^4(f)df}. \tag{2.12}$$

The zeroth m_0 and first m_1 moments of the wave spectrum are used to calculate mean spectral period

$$T_{01} = \frac{m_0}{m_1}. \tag{2.13}$$

The mean wave direction D_m and mean wave directional spread σ are calculated from $\overline{a_1}$ and $\overline{b_1}$, the spectrally-averaged lowest order Fourier moments of the wave spectrum, as

$$D_m = \tan^{-1}\left(\frac{\overline{b_1}}{\overline{a_1}}\right) \quad \sigma = \sqrt{2(1 - \sqrt{\overline{a_1}^2 + \overline{b_1}^2}}. \tag{2.14}$$

Previous studies have found that the above wave parameters and tidal elevation η and motion $\frac{d\eta}{dt}$ influence rip current characteristics (see Section 1.2.3).

The influence of wave steepness on rip current occurrence and speed was examined by including H_s/λ as a parameter in the analysis.

Three non-standard wave parameters were also included in the analysis, and are listed in Table 2.2. The parameter $\sqrt{H_s\lambda}$ has been used in predictions of wave run-up (Stockdon et al., 2006) and was included in this analysis to examine a potential

relation between run-up and rip currents. Wave factor $W_f = H_sT$ was identified by Scott et al. (2014) as a key factor controlling rip current behaviour. Castelle et al. (2024) also saw that rip current hazard increased with H_sT. The last non-standard parameter H_s^2T is a proxy for deep-water wave energy flux (Scott et al., 2011) and was included to examine a potential influence on rip current characteristics.

Parameter	Description
$\sqrt{H_s\lambda}$	Run-up parameter (Stockdon et al., 2006)
H_sT	Wave factor (Scott et al., 2014)
H_s^2T	Proxy for deep-water wave energy flux (Scott et al., 2011)

Table 2.2: Description of non-standard wave parameters tested in analysis. All parameters were calculated using both peak period/wavelength and mean spectral period/wavelength.

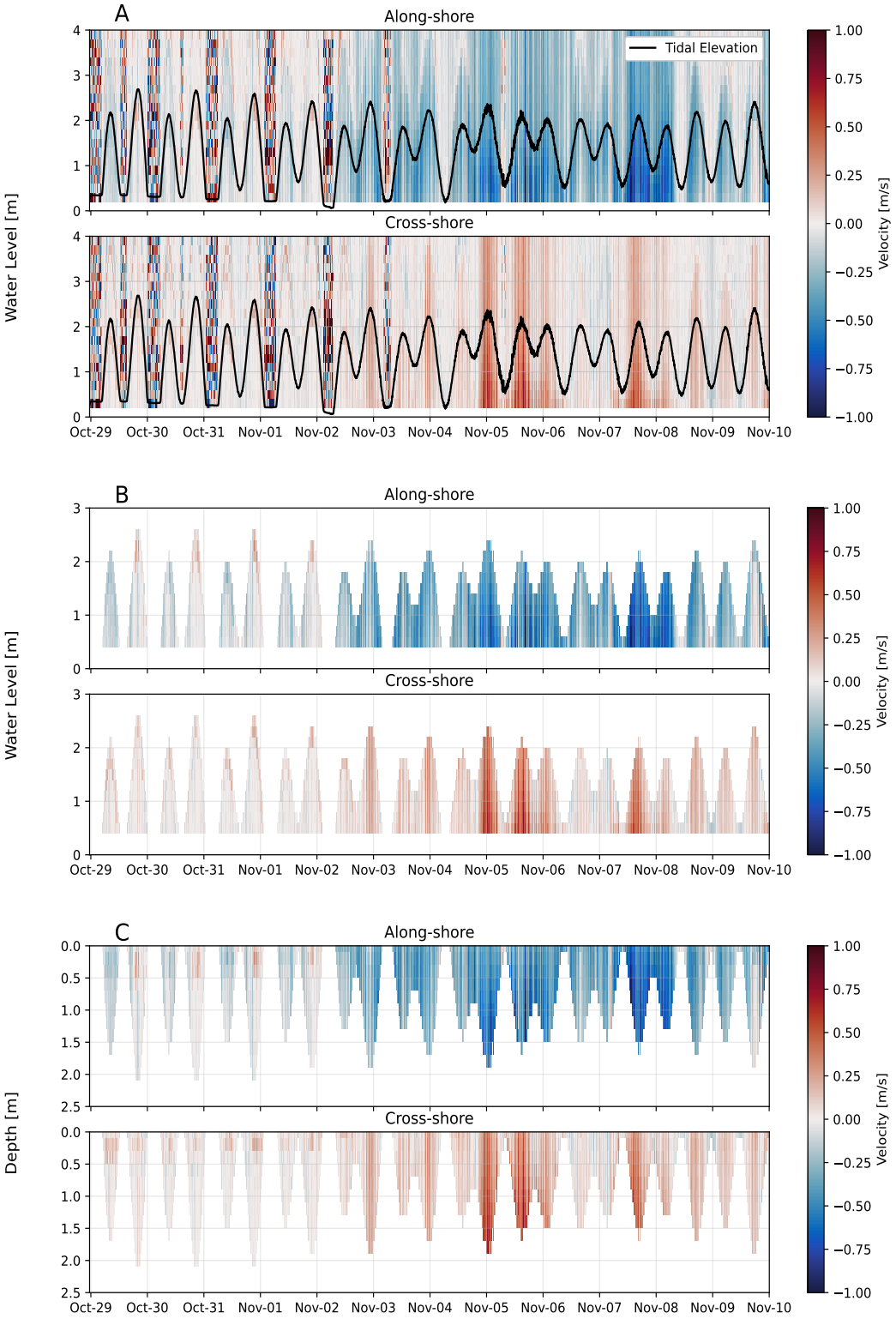

Figure 2.11: Processing of the raw velocity profiles (A). Velocity values above the tidal elevation were removed (B) and the reference frame changed by re-mapping the velocity profiles (C).

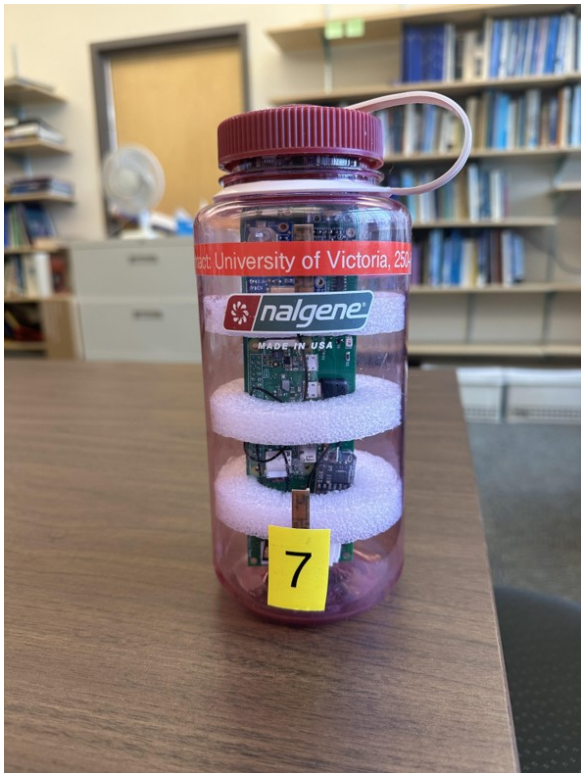

Figure 2.12: Surf zone drifter modified from the design of Rainville et al (2023).

Chapter 3

Results

3.1 Rip Current Occurrence

Long-term camera observations of the rip current at Wickaninnish Beach show that rip current occurrence increases primarily with significant wave height. Since wave height is proportional to wave energy, this suggests that sufficient energy must be transferred from breaking waves in order to drive rip current flow at Wickaninnish Beach. Longer values of mean spectral wave period were found to also result in greater rip occurrence, however, to a lesser extent than significant wave height.

Camera observations at Wickaninnish Beach were made from late August to December 2023, May to October 2024, and December 2024 to the end of January 2025, resulting in a total of 33127 images. After rejecting 12126 images due to poor visibility, 21001 images were left to be used in the analysis. The images were sorted into rip current events and non-rip current events, resulting in 7962 rip events and 13039 non-rip events. Rip current events make up 38% of the usable camera images.

In the observational periods for 2023 and 2024, December had the greatest percentage of rip current events with approximately 65% in 2023 and 45% in 2024 (Figure 3.1). January was the only month from 2025 with observations and had a similar percent occurrence of rip events to December 2025. The period from August to December 2023 is not a continuous five months of data, as power outages in August, October, and November resulted in only three days of observations for each of these months. The dataset is nearly continuous for the majority of the 2024 observations. No observations were made during November and early December 2024.

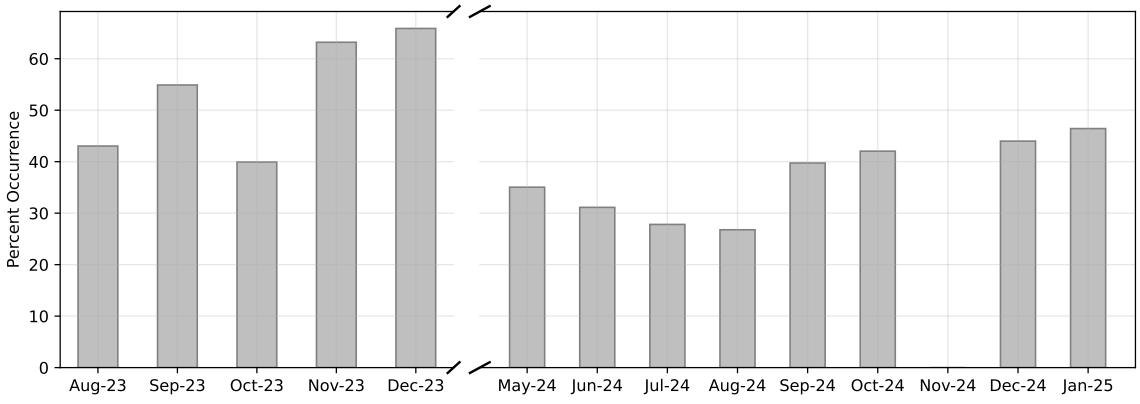

Figure 3.1: Monthly rip current percent occurrence at Wickaninnish Beach as obtained from camera observations. There is a gap in the dataset from the end of December 2023 to the beginning of May 2024. November 2024 had no observations.

3.1.1 Environmental Controls

Wave Field

Normalised histograms for rip (one or more rip current visible in an image) and non-rip (no visible rip currents in an image) events were plotted for each bulk wave parameter from the Spotter wave buoy 1881 at Wickaninnish Beach (Figure 3.2). Differences between the distributions indicate conditions favourable for rip or non-rip events.

The rip event distribution is shifted towards greater values of significant wave height H_s and longer values of mean spectral period T_{01} (Figure 3.2A and C), indicating these values of H_s and T_{01} are more favourable for rip occurrence. More rip current events tend to occur for H_s values greater than 1.5 m and T_{01} values greater than 8 s. The separation between the rip and non-rip distributions is visually greater for H_s than for T_{01}. Little separation is seen between the distributions for peak period T_p, mean direction D_m, directional spreading σ, or peak wave steepness H_s/λ_p (Figure 3.2B, D, E, F).

Although mean wave direction D_m did not show an influence on rip occurrence, Figure 3.2D does show that D_m values range from 180 to 260°, with waves approaching from the south to south-southwest. The rip current at Wickaninnish Beach then occurs in the lee of the incident waves, making it a shadow rip current (Figure 3.3).

The mean value of each wave parameter for the rip and non-rip distributions was found. The percent differences between these values were used to quantitatively

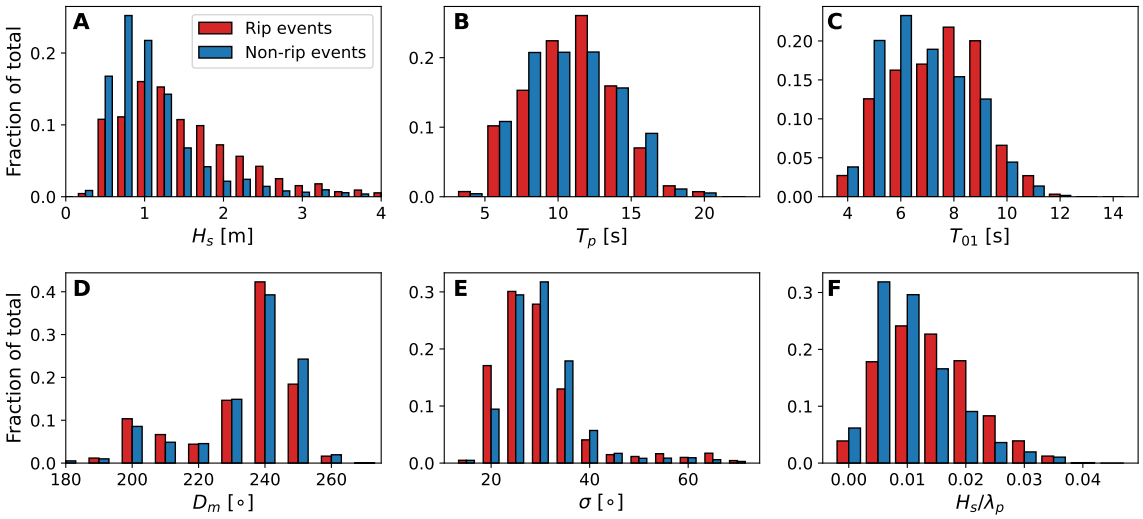

Figure 3.2: Normalised histograms of the rip event (red) and non-rip event (blue) distributions, as obtained from camera observations, for wave parameters from Spotter buoy 1881 at Wickaninnish Beach. The wave parameters plotted are significant wave height (A), peak period (B), mean spectral period (C), mean wave direction (D), directional spreading (E), and peak wave steepness (F).

examine the differences between the distributions (Table 3.1).

The mean values of H_s, T_p, T_{01}, and H_s/λ_p are all greater for the rip events distribution than that of the non-rip events. The greatest percent difference of nearly 26% occurs for H_s. Despite having little visible separation between the distributions in Figure 3.2F, H_s/λ_P has the second greatest percent difference of 22%. T_p, D_m, and σ have percent differences of less than 2%, with the smallest difference occurring for D_m.

The two-dimensional distributions of rip and non-rip events were compared using 2-D density contour plots (Figure 3.4). This avoided the issue of over-plotting on standard scatter plots that can arise from large datasets.

The density contours for rip events are shifted towards greater values of H_s for all the two-dimensional distributions. The density contour plot of rip events for T_{01} vs H_s shows the contours are also shifted towards longer T_{01} values, resulting in a diagonal contour shape (Figure 3.4C). The corresponding plot for non rip events (Figure 3.4D) shows that data are mainly concentrated at smaller H_s and shorter T_{01} values. The rip event contours for T_p vs H_s (Figure 3.4A) are shifted towards greater values than the corresponding plot for non-rip events (Figure 3.4B); however, T_p values span a similar range for rip and non-rip events. This also occurs for D_m vs H_s (Figure 3.4

Wave Parameter	Mean (rip)	Mean (non-rip)	Percent Difference
H_s	1.61 m	1.25 m	25.52%
T_p	12.00 s	11.85 s	1.18%
T_{01}	7.96 s	7.36 s	7.81%
D_m	237°	239°	0.94%
σ	31.7°	32.2°	1.52%
$\frac{H_s}{\lambda_p}$	0.017	0.013	21.86%

Table 3.1: Mean values and percent differences of means for each wave parameter from Spotter buoy 1881 for rip and non-rip events at Wickaninnish Beach.

Figure 3.3: Rip current flow at Wickaninnish Beach. Mean wave directions from the southwest indicates this is a shadow rip current.

E and F). All three relations show that rip events occur with larger values of H_s; however, only the relation with H_s and T_{01} shows a clear separation for rip current events.

Tide

Normalized histograms were plotted of the rip and non-rip distributions for tidal elevation η and tidal motion (Figure 3.5). Tidal motion was defined as the time derivative of tidal elevation, $d\eta/dt$. For a rising (falling) tide, $d\eta/dt$ is positive (negative). The group of rocks at Wickaninnish Beach is never fully exposed at low tide.

There is no clear separation between the rip and non-rip distributions for either tidal elevation or motion (Figure 3.5). Both distributions overlap across the entire range of tidal elevations and motions, and are shifted towards mid-low tide. It does not appear that tidal elevation or motion influence rip occurrence at Wickaninnish Beach.

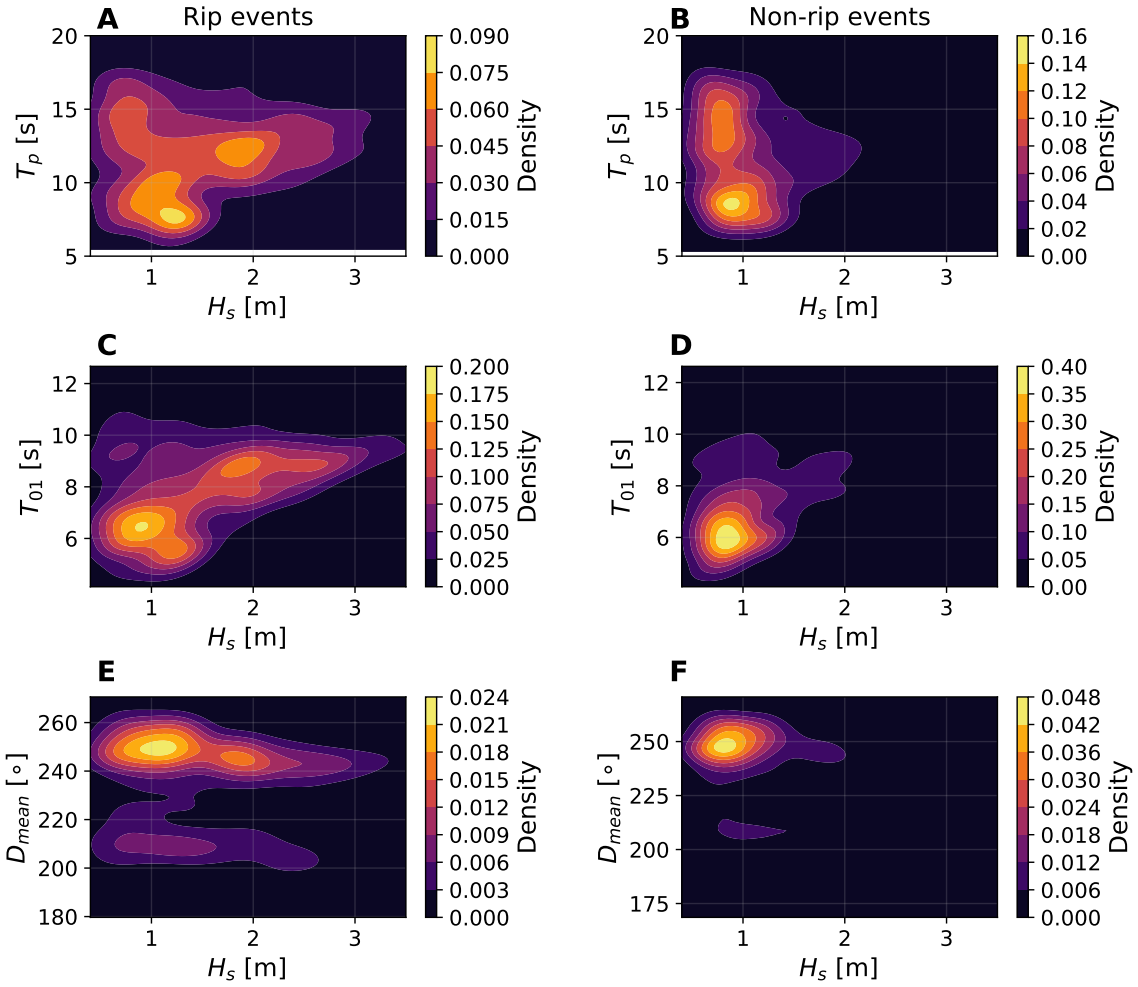

Figure 3.4: 2-D density contour plots for rip (left column) and non-rip (right column) events. Bulk wave parameters are from the Spotter buoy 1881 at Wickaninnish Beach. The relations plotted are peak period vs significant wave height (A, B), mean spectral period vs significant wave height (C, D), and mean wave direction vs significant wave height (E, F).

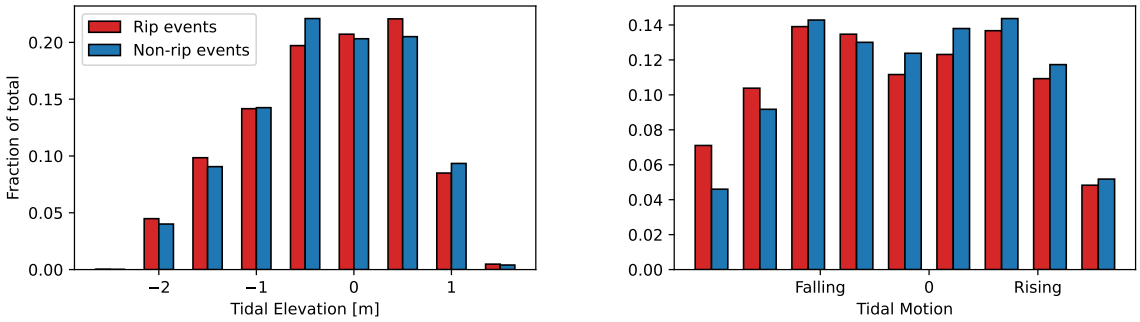

Figure 3.5: Normalized histograms of the rip event (red) and non-rip event (blue) distributions, as obtained from camera observations, for tidal elevation (left) and motion (right). Tidal elevation values are relative to mean sea level (MSL).

3.1.2 Occurrence Probability

The probability P_{rip} of a rip current occurring at Wickaninnish Beach increases with significant wave heights greater than 1 m and exceeds 50% at values greater than or equal to 1.8 m (Figure 3.6A). The maximum P_{rip} value of 63% occurs at an approximate H_s value of 2.1 m. P_{rip} also increases with mean spectral period values greater than 6 s, and reaches a maximum value of 50% for T_{01} values greater than 8.5 s (Figure 3.6C). No clear trend is seen for T_p (Figure 3.6B).

While the normalized histograms for peak wave steepness did not show a separation between the rip and non-rip current distributions, P_{rip} increases with H_s/λ_p, and exceeds 50% at the largest values of H_s/λ_p (Figure 3.6F). This appears to be primarily driven by the increase in P_{rip} with H_s. There is a slight decrease in occurrence probability with increasing mean wave direction, as incident waves approach closer to west-northwest; however, as the difference between the minimum and maximum probability is less than 15%, this decrease does not appear significant (Figure 3.6D). P_{rip} initially decreases from 50% to 30% with increasing values of σ, before increasing very slightly to 40% at the largest σ values (Figure 3.6E). Similarly to D_m, the difference between the maximum and minimum probability, is around 20%. P_{rip} does not show a dependence on tidal elevation or tidal motion, remaining between 30% and 40% across nearly the entire range of both parameters (Figure 3.7).

During any wave or tide conditions there is a non-zero chance of a rip current occurring at Wickaninnish Beach (Figures 3.6 and 3.7). Larger and longer waves result in rip occurrence probabilities that exceed 50%, and can be considered the highest-risk conditions for rip current development at Wickaninnish Beach.

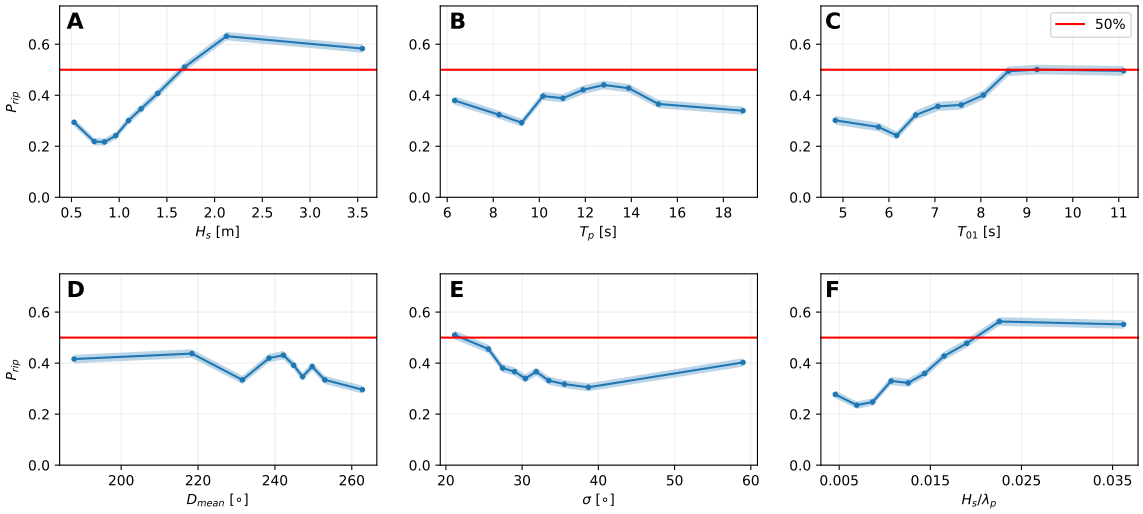

Figure 3.6: Rip current occurrence probability for bulk wave parameters from Spotter buoy 1881 at Wickaninnish Beach. The bulk wave parameters plotted are significant wave height (A), peak period (B), mean spectral period (C), mean wave direction (D), directional spreading (E), and peak wave steepness (F). The 95% confidence interval is shaded and the red line is at a probability of 50%.

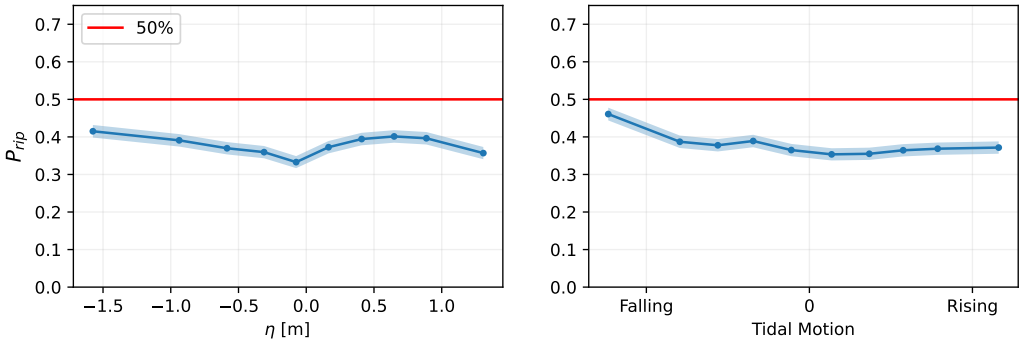

Figure 3.7: Rip current occurrence probability for tidal elevation (left) and motion (right) at Wickaninnish Beach. The 95% confidence interval is shaded and the red line is at a probability of 50%. Tidal elevation values are relative to MSL.

3.2 Eulerian Rip Current Flow

Offshore velocity measurements from the 10-day surf zone ADCP deployment at Wickaninnish Beach show that rip current speed increases with both significant wave height and mean spectral period, with significant wave height having a greater influence. These same wave conditions were also seen to increase rip current occurrence at this location. A strong linear relation was found between offshore rip current velocity and H_s^2, indicating that increasing wave energy results in faster rip current flow at Wickaninnish Beach.

3.2.1 Environmental Controls

Depth-averaged Velocities

Normalised distributions of the depth-averaged cross-shore u_b and alongshore v_b velocities measured by the ADCP have peaks at -0.2 m/s and 0 m/s respectively (Figure 3.8). The mean cross-shore velocity is 0.07 m/s with a tail towards positive (offshore) velocity values (Figure 3.8 left). The longshore current at Wickaninnish Beach mainly flows from north to south, towards the direction of the rock outcrop, as indicated by the mean alongshore velocity values of -0.26 m/s (Figure 3.8 right). The north to south direction of the longshore current fits with the characteristics of a structurally-controlled rip current at this location.

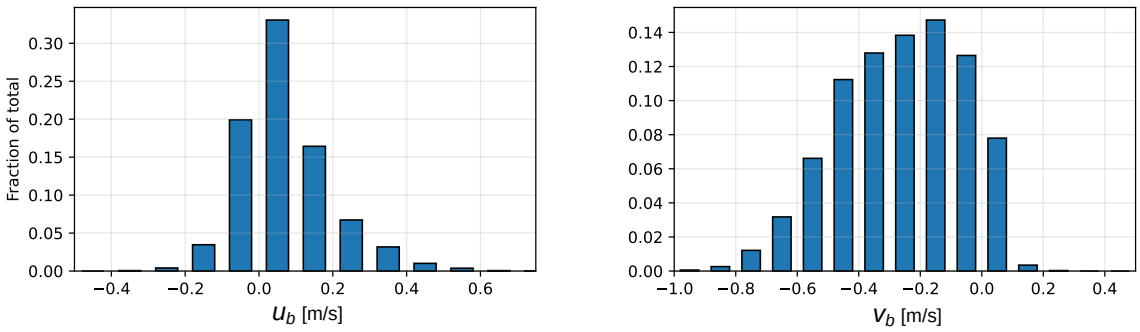

Figure 3.8: Normalized distributions of the depth-averaged cross- (left) and alongshore (right) velocities. Positive cross-shore velocity values are offshore while positive alongshore velocity values are alongshore towards the south.

Wave Field

Although the ADCP data were processed to create a dataset with an averaged velocity value every 5 minutes, wave conditions change over longer timescales. From the depth-averaged cross-shore velocity, two variables were defined to examine rip current velocity over an hourly timescale. V_{max} is the greatest 5 minute averaged velocity value each hour and V_{mean} is the mean value of the three greatest 5 minute averaged velocity values during each hour. Normalized distributions of V_{max} and V_{mean} have peaks in the range of 0 - 0.1 m/s, which make up approximately 29% and 35% of the observations, respectively (Figure 3.9).

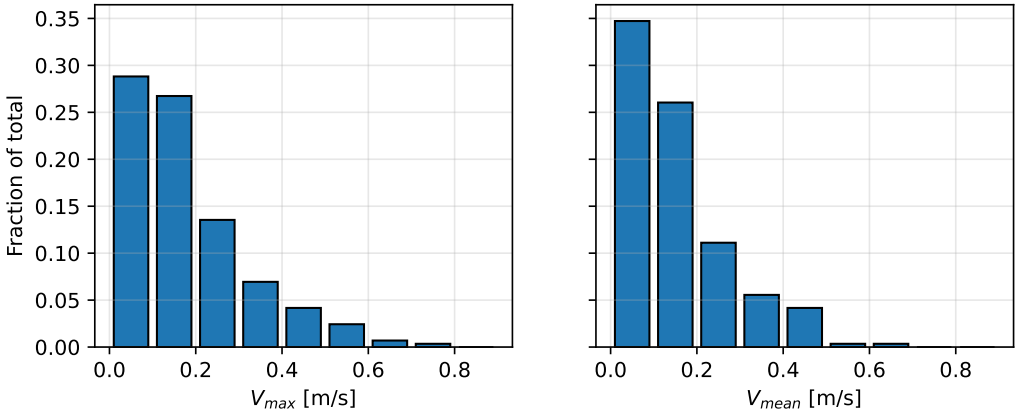

Figure 3.9: Normalized distributions of the hourly maximum (left) and mean (right) depth-averaged offshore velocities.

V_{max} and V_{mean} are fairly similar over the duration of the ADCP deployment (Figure 3.10). During the strongest currents V_{max} does becomes noticeably greater than V_{mean} (Figures 3.11E and 3.10). Due to these similarities, further results will only be shown for V_{max}.

For the first three days of the 10 day ADCP deployment, significant wave height values were less than or equal to 1 m (Figure 3.11B). During this period the offshore velocities were between 0.1 and 0.15 m/s, with no rip activity. After November 2nd, significant wave heights began to increase and reached a maximum value of 4 m on November 5th. This is also when the greatest offshore velocities occur.

Hourly V_{max} values were compared to hourly wave parameters using scatter plots, with linear regressions calculated for each relation. V_{max} was found to increase with H_s (Figure 3.12A). The correlation coefficient of 0.75 indicates that this is a strong correlation; however, the relation appears more quadratic than linear, especially for

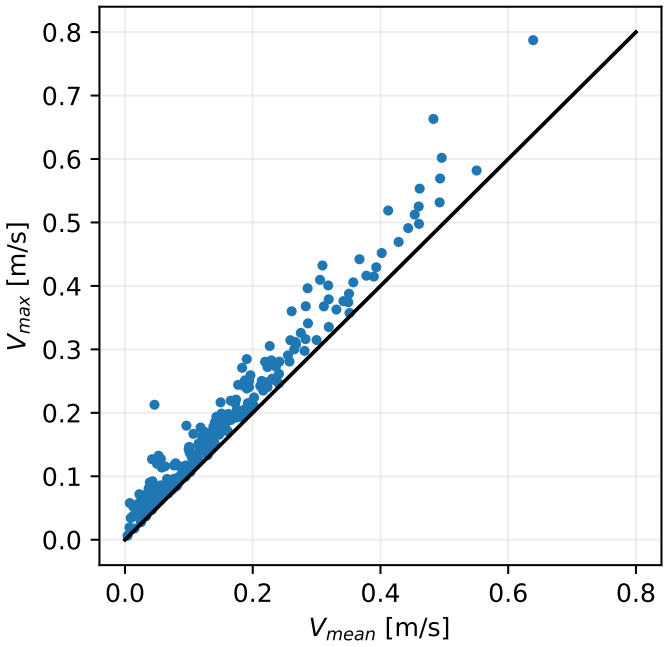

Figure 3.10: Scatter plot of hourly maximum offshore velocity against hourly mean offshore velocity. The black line is the 1:1 line.

H_s values greater than 2.0 m. Plotting V_{max} against H_s^2 improves the correlation coefficient to 0.80. This improved relation indicates that increasing incident wave energy results in greater rip current speed (Figure 3.12B).

The greatest values of V_{max} occur for longer mean spectral periods (Figure 3.12C) and for peak period values in the range of 11 - 14 s (Figure 3.12D). There is a weak linear relation between V_{max} and T_{01} that is not present for T_p. During the ADCP deployment, T_p showed more variation over shorter timescales, especially during the time of low H_s values from 29 October - 2 November (Figure 3.11 B and C). While T_p and T_{01} follow the same overall trend, T_{01} is more stable over shorter timescales and appears to better reflect changes in the wave field.

There are also moderate positive correlations between V_{max} and mean wave direction D_m, directional spread σ, and wave steepness H_s/λ_p (Figure 3.12E, F, G, H). During the ADCP deployment, waves approached from 200 to 260°, or south to west-southwest, resulting in a shadow rip current at Wickaninnish Beach (Figure 3.12E). During this time, waves that approached from directions closer to 260° (west-southwest) tended to have greater H_s values, as did waves with greater directional spread (Figure 3.13). Significant wave height then appears to be the primary

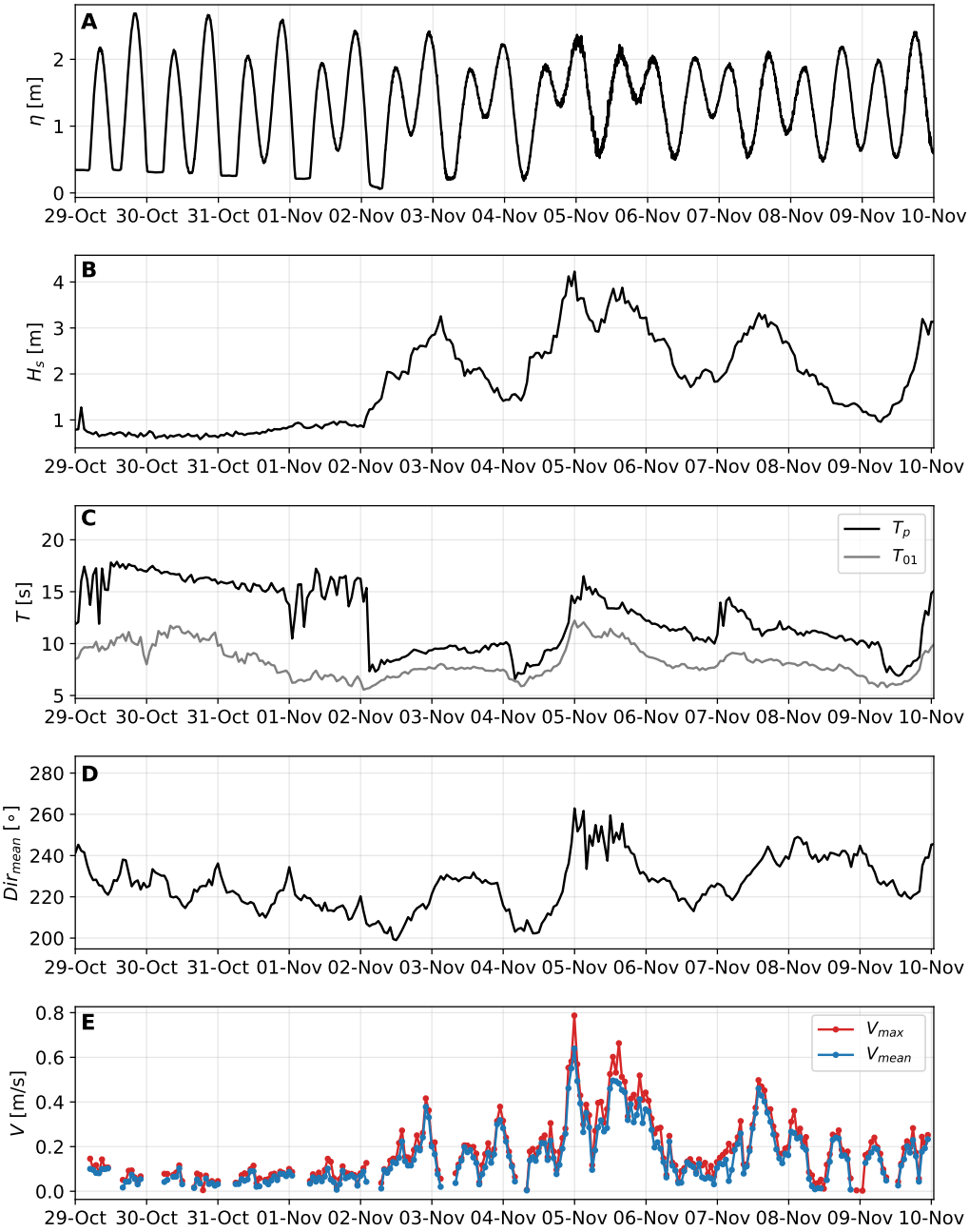

Figure 3.11: Time series of bulk wave parameters from Spotter buoy 1881 (Wickaninnish Beach) and the hourly mean and maximum depth-averaged offshore velocities. From top to bottom: tidal elevation measured by the ADCP (A), significant wave height (B), peak period (black line) and mean spectral period (grey line) (C), mean wave direction (D), and hourly mean (blue line) and maximum (red line) offshore velocities (E). Note that the ADCP is dry during the spring low tides.

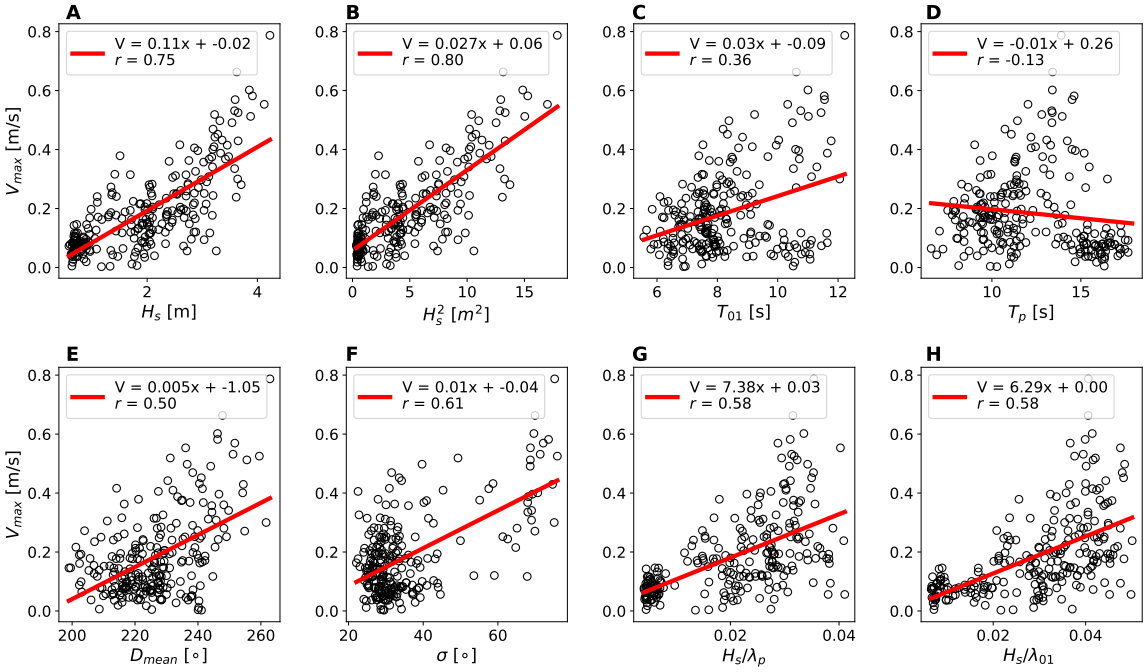

Figure 3.12: Scatter plots of hourly maximum offshore velocity against bulk wave parameters from Spotter buoy 1881 (Wickaninnish Beach) with linear regression lines. The bulk wave parameters plotted are significant wave height (A), significant wave height squared (B), mean spectral period (C), peak period (D), mean wave direction (E), directional spread (F), peak wave steepness (G), and mean wave steepness (H). The slope and intercept of each regression line are labelled along with the correlation coefficient for each relation.

parameter driving increases in offshore rip velocity.

The relationships between offshore velocity and the non-standard wave parameters (the run-up parameter $\sqrt{H_s\lambda}$, wave factor H_sT, and deep-water wave energy flux H_s^2T) were also examined (Figure 3.14). V_{max} increases for all non-standard parameters, with slight improvements in the correlation coefficients for the parameters calculated using mean spectral period instead of peak period (Figure 3.14D, E, F). This reflects the better relationship seen between V_{max} and T_{01} in Figure 3.12C. While $H_s^2T_{01}$ has the greatest correlation coefficient overall, this value is only slightly greater than those calculated for the other relations. Multi-variable regressions were calculated to examine the influence of multiple wave parameters on rip current velocity. Since wave height and period were found to be the most relevant wave parameters in controlling rip current speed, these two parameters were chosen for further examination as part of the four multi-variable regression formulas:

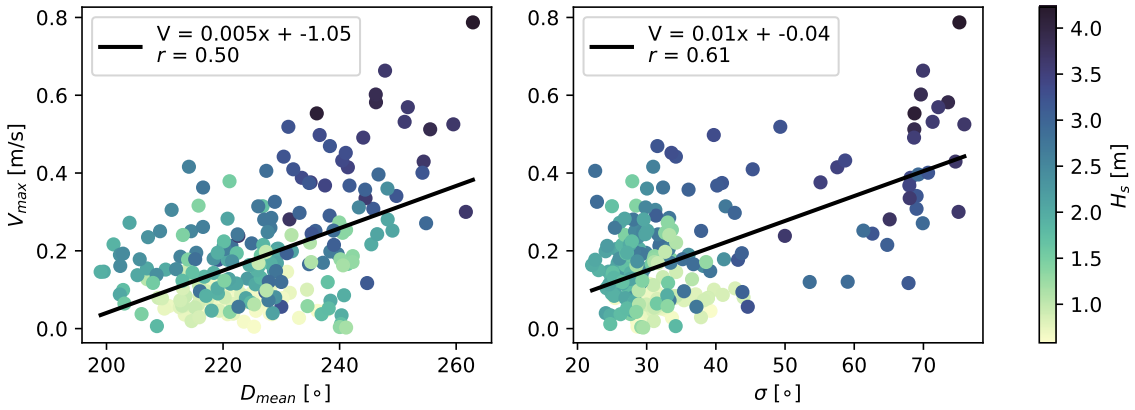

Figure 3.13: Scatter plot of maximum offshore velocity against mean direction (left) and directional spread (right) with linear regression lines. The data points are coloured by significant wave height. The slope and intercept of each regression line are labelled along with the correlation coefficient for each relation.

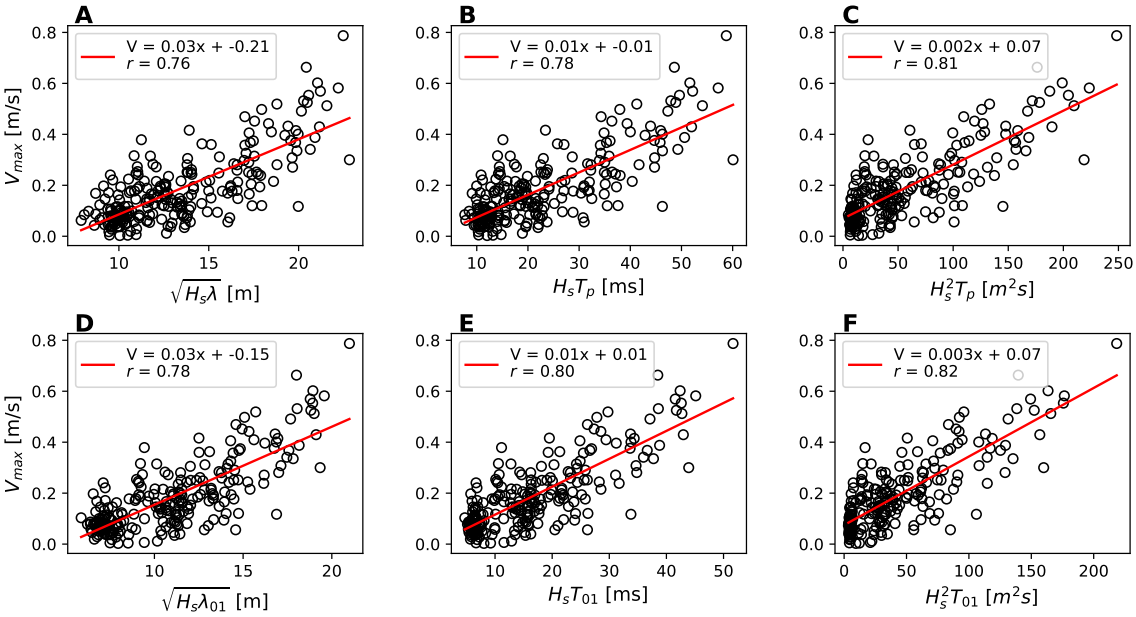

Figure 3.14: Scatter plots of hourly maximum offshore velocity against non-standard wave parameters calculated from Spotter buoy 1881 with linear regression lines. The slope and intercept of each regression line are labelled along with the correlation coefficient for each relation.

$$
\begin{aligned}
V &= AH_s + BT_p + C \\
V &= AH_s + BT_{01} + C \\
V &= AH_s^2 + BT_p + C \\
V &= AH_s^2 + BT_{01} + C
\end{aligned}
\tag{3.1}
$$

where A and B are coefficients and C is the intercept.

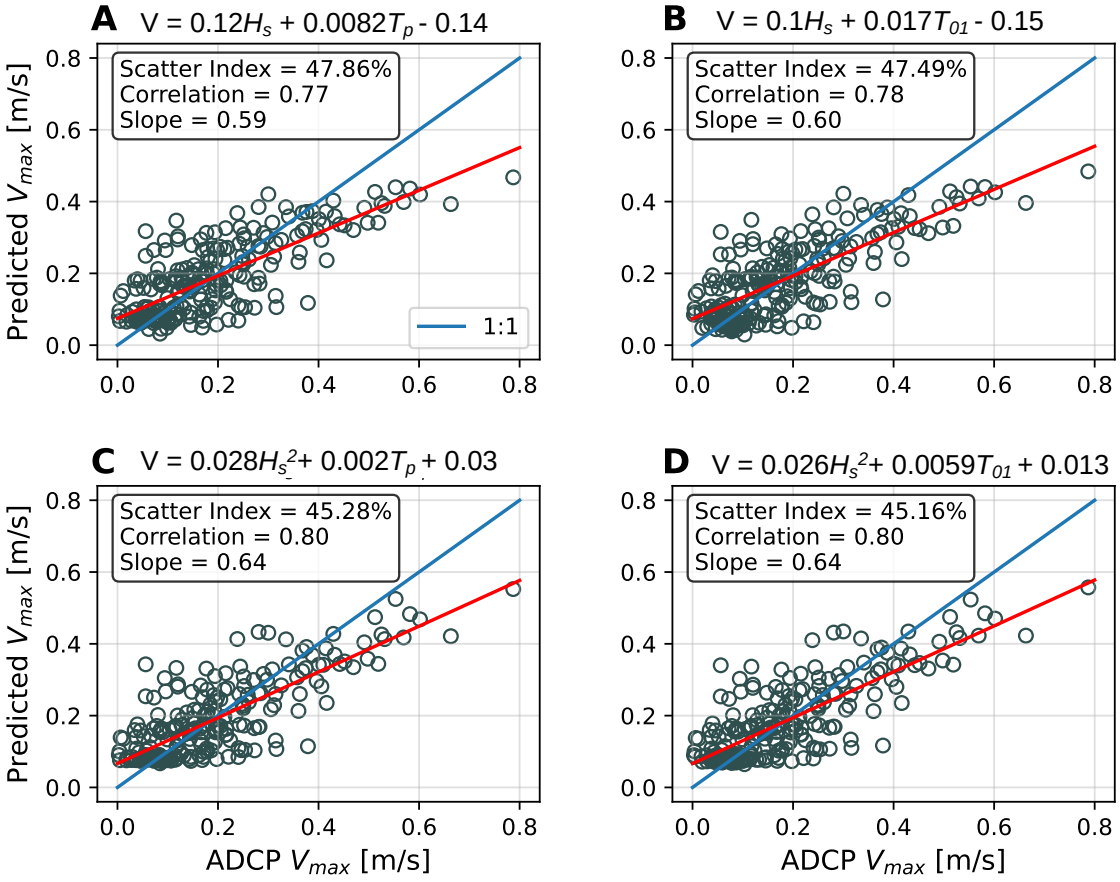

Figure 3.15: Scatter plots of hourly maximum offshore velocity calculated from multi-variable regression against hourly maximum offshore velocity measured by ADCP. The multi-variable regression is labelled at the top of each subplot. The blue line is the 1:1 line and the red line is the linear regression between the two velocities. The scatter index, correlation coefficient, and slope for the linear regression are labelled.

The predicted offshore velocity from each relation was plotted against the hourly offshore velocity as measured by the ADCP (Figure 3.15). A regression line was calculated along with the correlation coefficient, slope, and scatter index for the comparison of the two velocities. The criteria for evaluating the goodness of each fit is as follows: a correlation coefficient close to 1.0, a slope close to 1.0, and a low scatter index. The multi-variable regressions that use H_s^2 (Figures 3.15 C and D) show very slight improvements compared to the regressions that H_s (Figures 3.15 A and B), reflecting the slightly stronger relationship seen between H_s^2 and offshore velocity in Figure 3.12. However, it is not clear if these slight differences are of significance.

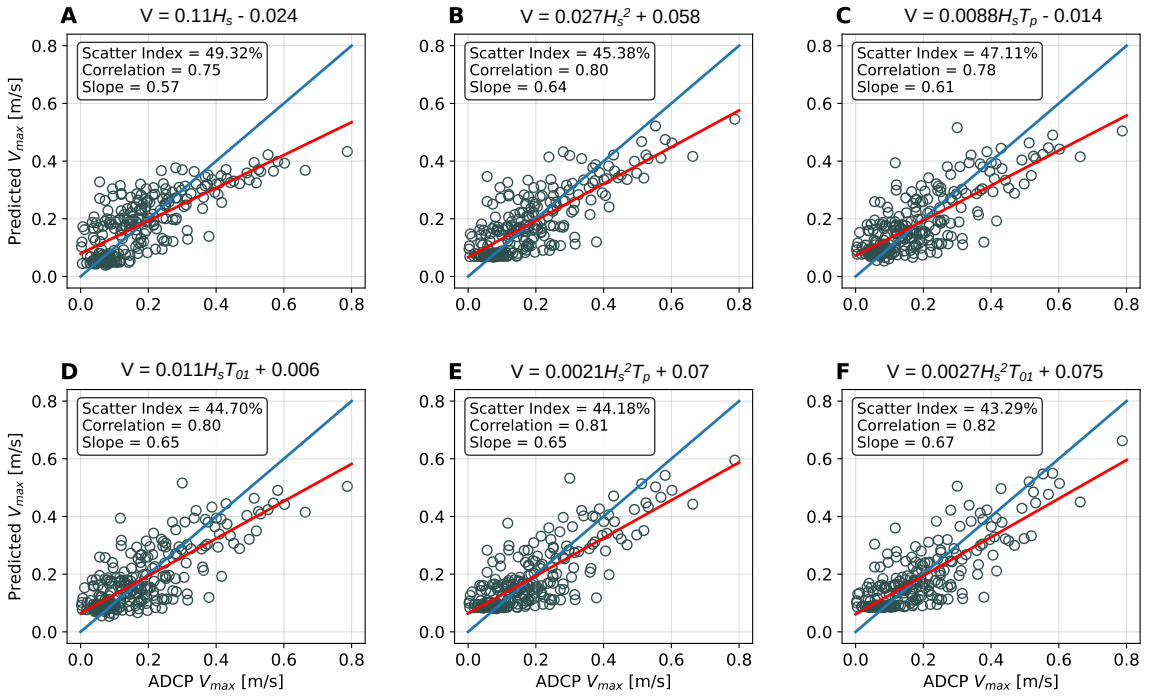

Figure 3.16: Scatter plots of hourly maximum offshore velocity calculated from single-variable regression against hourly maximum offshore velocity measured by ADCP. The single-variable regression is labelled at the top of each subplot. The blue line is the 1:1 line and the red line is the linear regression between the two velocities. The scatter index, correlation coefficient, and slope for the linear regression are labelled.

Similar plots were made for the single variable regressions with the greatest correlation coefficients, as found previously (Figure 3.16). As was the case in Figure 3.15, the differences between the regressions are very small and it is not clear if these differences are significant. Any parameter used in the regressions in Figure 3.16 would likely be a good predictor of rip current speed. The strong relationships between V_{max} and parameters that include wave height and period show that an increased rate of wave energy transfer also drives an increase in rip current speed.

Tide

No strong linear correlations were found between hourly V_{max} and tidal elevation or motion. Stronger V_{max} values tend to occur around high tides (Figure 3.17 left); however, this is due to a greater amount of water over the ADCP during these times, as during spring low tides the ADCP is out of the water. Stronger velocities also appear to occur when the tidal motion is near zero (Figure 3.17 right). Based on

Figure 3.17 (left), these higher velocities occur when the tide is transitioning from rising to falling (high tide), rather than from falling to rising (low tide).

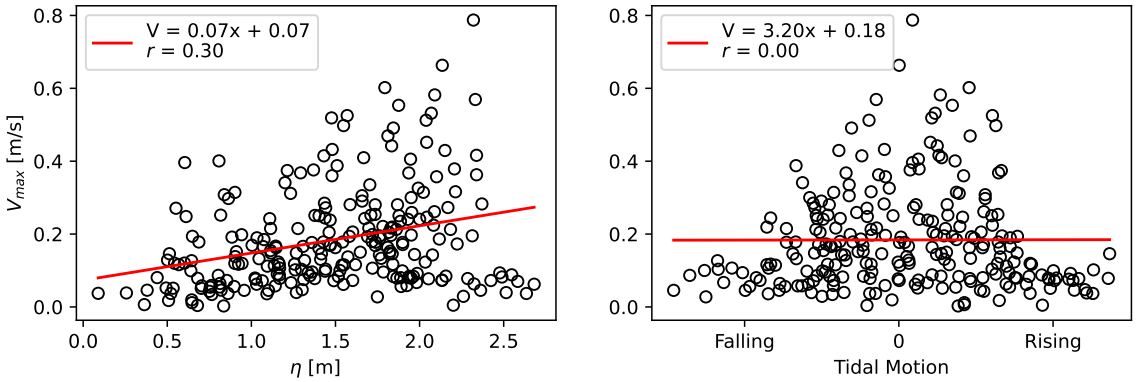

Figure 3.17: Scatter plots of hourly maximum offshore velocity against tidal elevation (left) and motion (right) measured by the ADCP at Wickaninnish Beach. The slope and intercept of each linear regression line are labelled along with the correlation coefficient for each relation. Note that the ADCP is dry during the spring low tides.

3.2.2 Vertical structure

Rip current events were identified from the cross-shore velocity time series to investigate the vertical structure of rip current flow. Rip events were defined as extended periods of time when the depth-averaged offshore flow exceeded the background mean velocity. For both V_{max} and V_{mean} this threshold value was set at 0.15 m/s.

Eight rip events were identified, all occurring after November 2 (Figure 3.18). The longest rip event occurred from November 4 - 6 for a duration of 50 hours and had the highest maximum offshore velocity of all rip events (Table 3.2), occurring when nearshore significant wave heights were at a maximum (Figure 3.18).

The vertical distributions of the cross-shore velocities during rip events are, for the most part, uniform with depth (Figure 3.19). The strongest rip events have offshore velocities close to 1.0 m/s. For the majority of the rip events, offshore velocity dominates; however, Events 4 and 8 have periods of occasional onshore flow (Figure 3.19D, H). For Event 8, this onshore flow occurs once in between weakening of the offshore rip current flow and lasts approximately one hour (Figure 3.19H). During Event 4, the on and offshore flows initially alternate before the onshore flow dominates for approximately two hours (Figure 3.19D). Although the depth-averaged offshore velocity exceeded to threshold value of 0.15 m/s for Event 4, the dominant onshore velocity

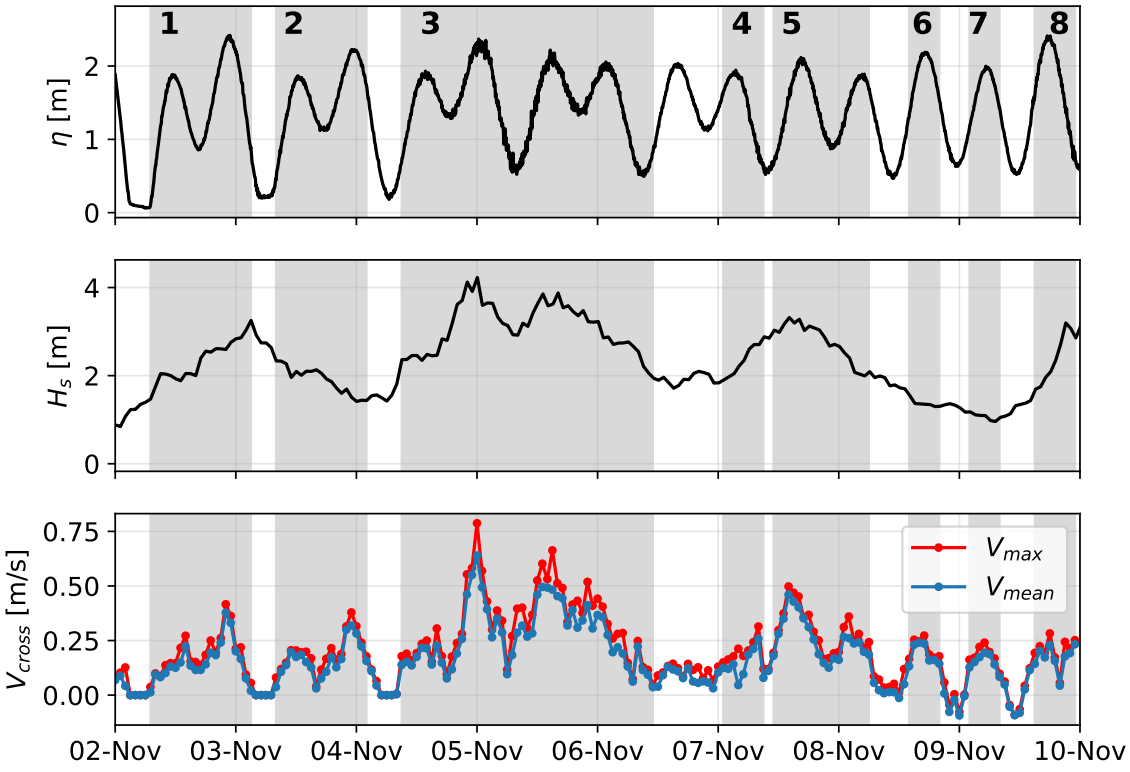

Figure 3.18: Time series of tidal elevation as measured by the ADCP (top), significant wave height (middle), and hourly mean (blue) and maximum (red) offshore velocities (bottom) for identified rip current events (shaded grey). Note that the ADCP is dry during spring low tides.

and weak offshore flow in Figure 3.19 would seem to indicate the Event 4 should not be labelled a rip event, and is excluded from further analysis.

Events 3 and 5 had the strongest offshore velocities (Figure 3.19C, E). The profiles during these events show a slight vertical shear, with stronger offshore velocities occurring at depth during the strongest rip current flow.

Time-averaging the cross-shore velocities over the duration of each rip event further shows that the dominant flow is offshore and depth-uniform for the first 1.0 m of the water column (Figure 3.20). Events 1, 2, 3, and 5 show vertical shear in the offshore velocity at depths greater than 1.0 m (Figure 3.20A, B, C, D). While a slight shear was observed for these rip events in Figure 3.19, there may be a bias towards greater velocities at depth. These events occurred over at least one tidal cycle, so fewer measurements were taken at the greater depths, introducing a potential bias when the profiles are averaged over longer rip events.

Event	Duration [hours]	V_{max} [m/s]
1	20	0.41
2	18	0.38
3	50	0.79
4	8	0.31
5	19	0.50
6	6	0.27
7	6	0.24
8	8	0.28

Table 3.2: Duration and maximum velocity of rip current events for 2 - 9 November 2023.

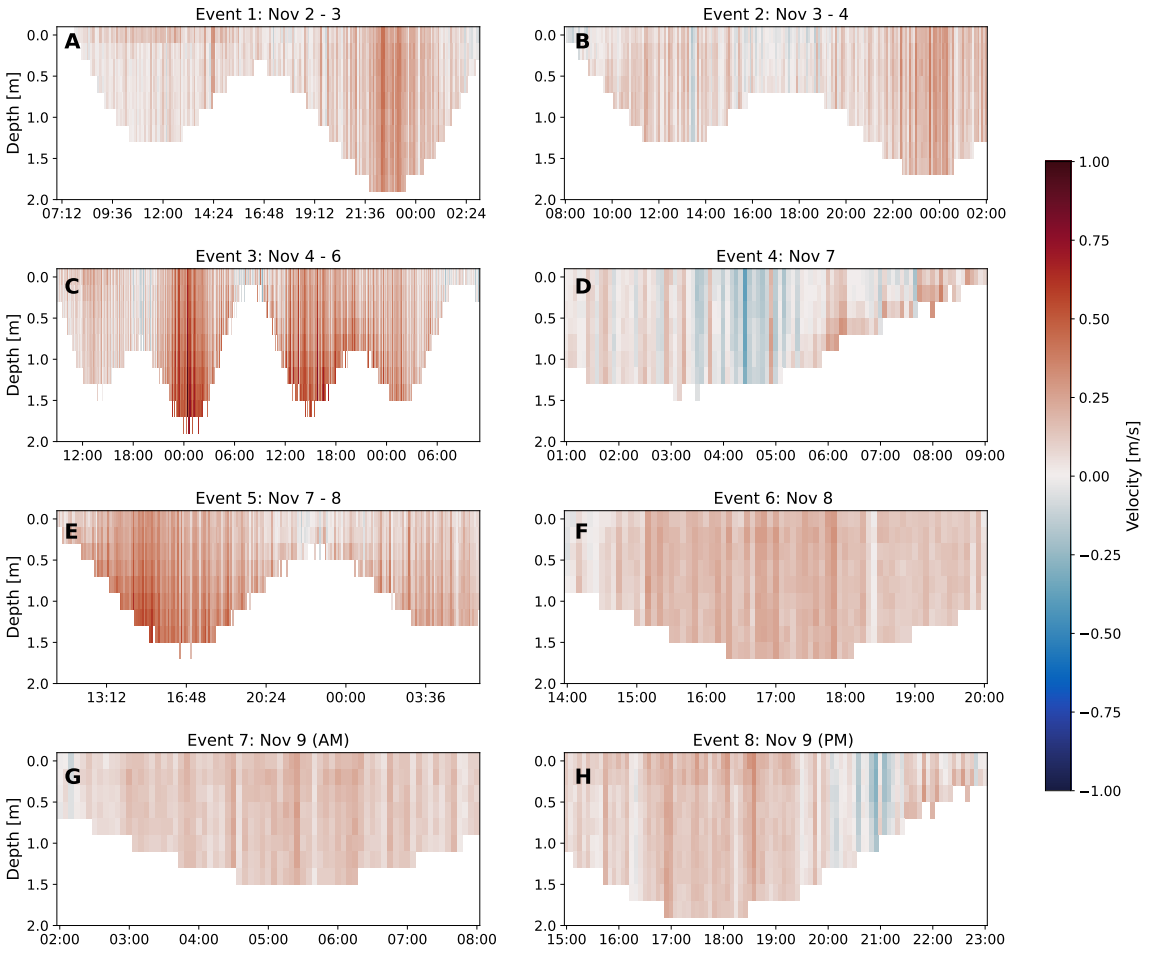

Figure 3.19: Cross-shore velocity profiles for the identified rip current events 1 - 8 (A - H).

The time evolution of the cross-shore velocity profiles do show a slight vertical shear for Events 3 and 5, with the offshore velocity increasing with depth (Fig-

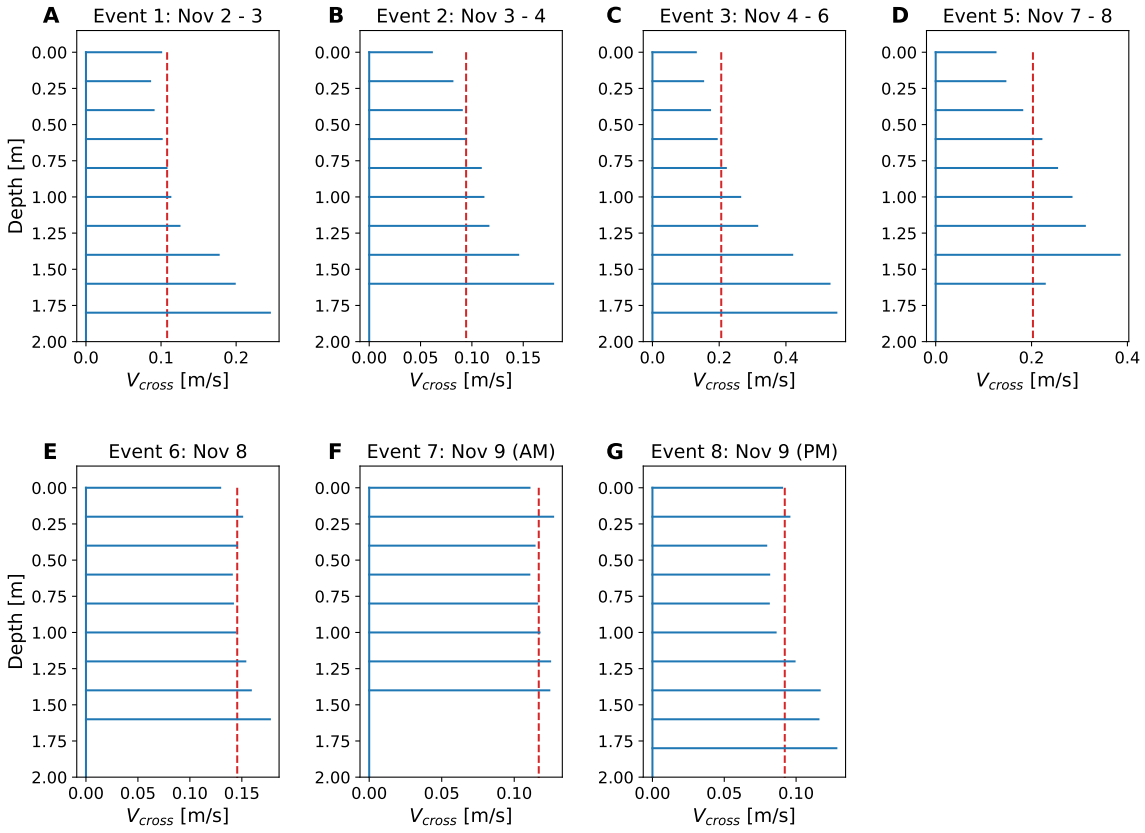

Figure 3.20: Cross-shore velocity profiles time-averaged over the duration of each rip current event (A - H). The vertical blue line is at 0 m/s and a horizontal line to the right indicates offshore velocity. The red-dashed line is the depth- and time-averaged cross-shore velocity for each rip event.

ure 3.21C, D). Significant wave heights during these events are greater than 3 m (Figure 3.11B). It is possible that the increased velocities at depth are the result of undertow, as the profiles for Events 3 and 5 (Figure 3.21C, D) resemble surf zone undertow profiles from Lentz et al. (2008). There is also a possibility that the offshore rip flow is restricted at the surface by the onshore transport of the larger waves during these events.

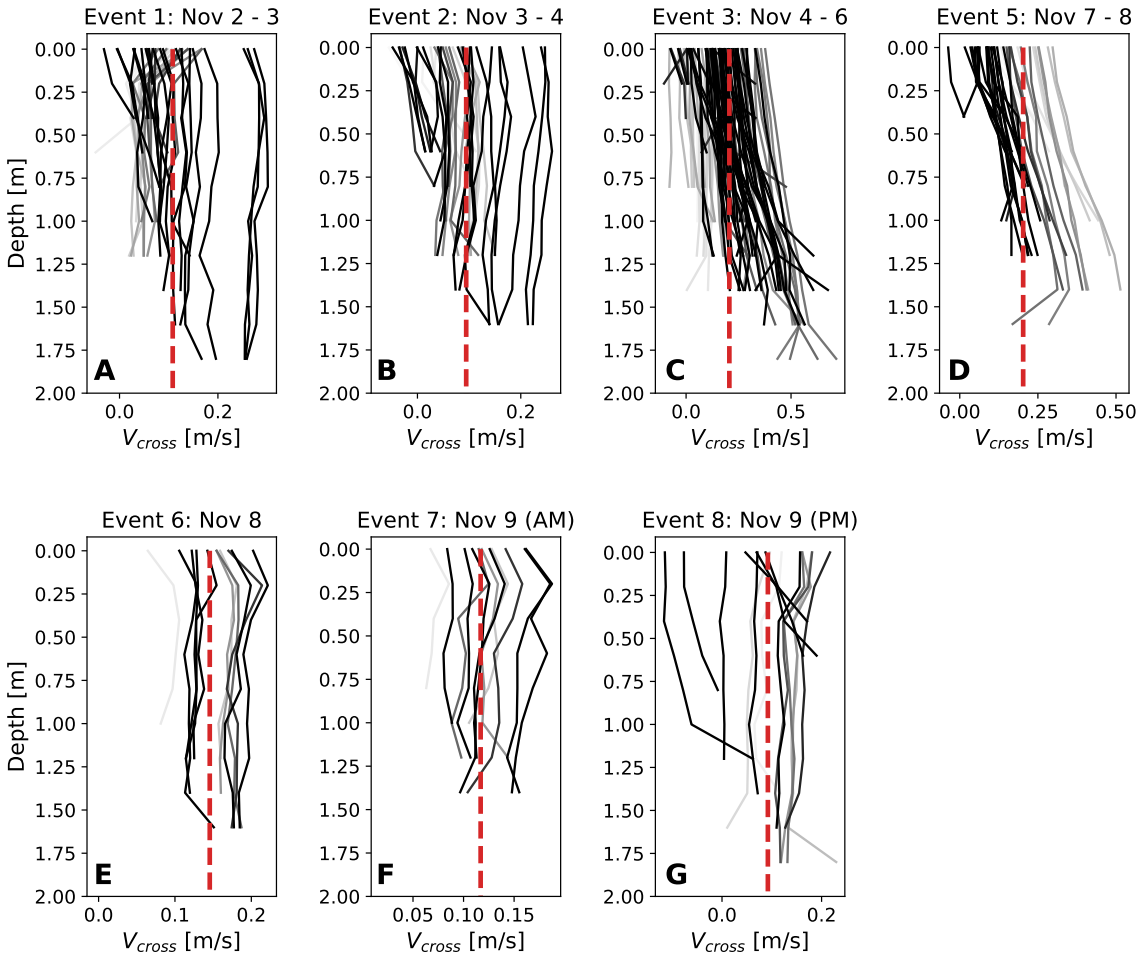

Figure 3.21: Time evolution of 30-minute averaged cross-shore velocity profiles for rip current events 1 - 8 (A - G). The profiles are coloured according to time: increasing in darkness from the beginning of the rip event to the end. The red-dashed line is the depth- and time-averaged cross-shore velocity for each rip event.

3.3 Perceived Rip Current Strength

During the summer seasons (May to September) of 2022 - 2024, the probability of a strong rip current at Lovekin Rock during any sea state is 25% (Figure 3.22). These are rip currents assigned a perceived strength S_p rating of considerable - high, or $S_p \geq 2$. This probability exceeds 50% for increasing values of significant wave height and mean spectral wave period.

Moderate strength rip currents dominate across all summer seasons at Lovekin Rock, making up 66.4% of the 476 total observations, while low strength rip currents occur just over 7% of the time (Figure 3.22). Considerable strength rip currents make

up nearly 22% of the total observations and just over 82% of the observed $S_p \geq 2$ rip currents. High strength rip currents make up the lowest percentage of observations and contribute nearly 18% of the observed strong rip currents.

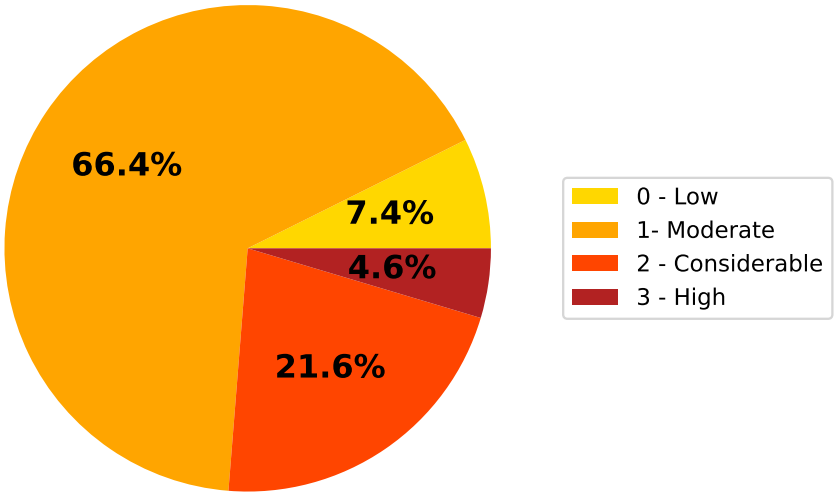

Figure 3.22: Distribution of perceived rip current strength S_p for the rip current at Lovekin Rock during the summer season (May - September) for the years 2022 - 2024. There are 476 total observations.

3.3.1 Wave Conditions

To examine the relation between wave conditions and rip current strength, normalised histograms were plotted against bulk wave parameters from the nearshore Spotter wave buoys for each S_p rating. Differences between the distributions indicate conditions favourable for different rip current strengths.

Strong rip currents tend to occur for greater significant wave heights; the distributions of strong rip currents $S_p \geq 2$ are shifted towards H_s values greater than 0.75 m, while the low and moderate distributions are shifted towards values less than 0.75 m (Figure 3.23A). Strong rip currents also occur more for greater values of mean spectral period (Figure 3.23C). There is a separation between the considerable - high and low - moderate strength distributions at a T_{01} value of 7 s. Stronger rip currents also occur more for longer values of peak period (Figure 3.23B); however, the separation between the distributions is less visible than in the plot for T_{01}. This reflects

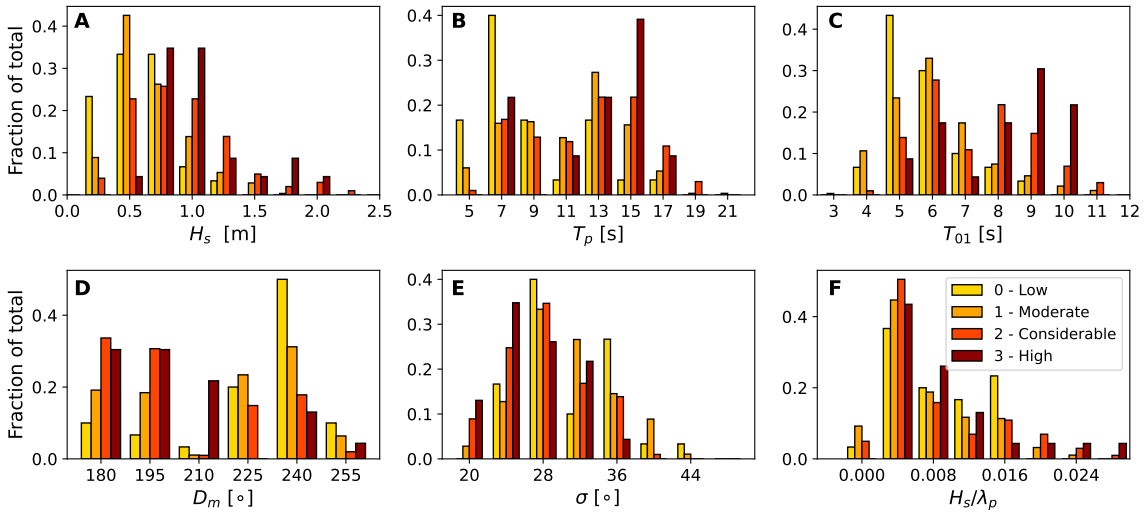

Figure 3.23: Normalised histograms representing the distribution of perceived rip current strength S_p for the rip current at Lovekin Rock (Long Beach) for bulk wave parameters from the nearshore Spotter buoys. Perceived strength observations are for the 2022 - 2024 summer seasons and wave parameters are calculated from the Spotter wave buoy 1445 at Schooner Cove (Sept 2023, May - Aug 2024) and the Spotter wave buoy 1881 at Wickaninnish Beach (Jul - Aug 2022, May - Aug 2023). The wave parameters plotted are significant wave height (A), peak period (B), mean spectral period (C), mean wave direction (D), directional spread (E), and peak wave steepness (F).

the result at Wickaninnish Beach that T_{01} influences rip current flow more than T_p. Stronger rip currents also tend to occur for mean wave directions between 180 and 200° (south-southwest) and for waves with narrow directional spread (Figure 3.23D and E). There is little separation between the distributions for peak wave steepness (Figure 3.23F).

The two-dimensional distributions of strong ($S_p \geq 2$) and weak ($S_p < 2$) rip events were compared using 2-D density contour plots. The density contours for strong rip events are shifted towards greater values of H_s, T_{01}, and T_p than for those of weak rip events (Figure 3.24A, B, C, D). The contours for strong rip events are concentrated around D_m values between 180 and 200 degrees (S - SSW) and are shifted towards greater H_s values than in the corresponding plot for weak rip events (Figure 3.24E and F).

The 2-D density plots for mean wave direction vs wave period show a similar trend. The contours for strong rip events are concentrated at longer values of T_p and T_{01}, and around D_m values of 180 - 200° (Figure 3.25A, C). There are two clusters of

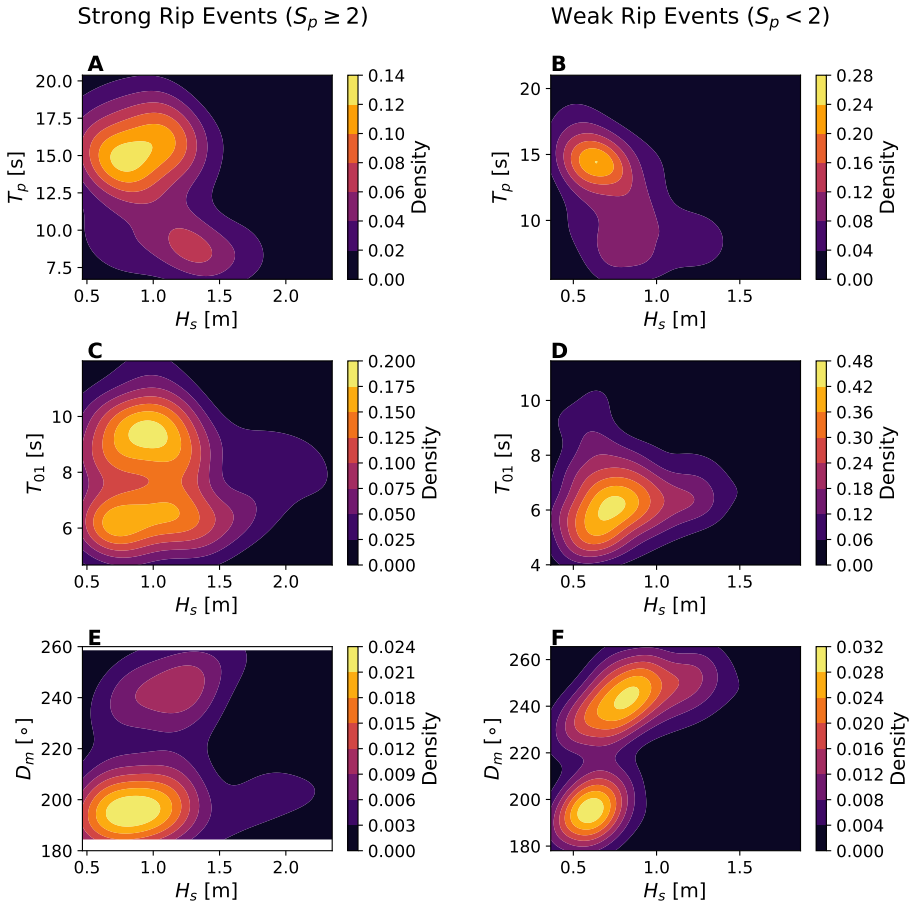

Figure 3.24: 2-D density contour plots for strong rip events (those with $S_p \geq 2$) and weak rip events (those with $S_p < 2$) at Lovekin Rock (Long Beach). Wave parameters are from the nearshore Spotter buoys 1881 (Wickaninnish Beach) and 1445 (Schooner Cove). The distributions of significant wave height with peak period (A and B), mean spectral period (C and D), and mean wave direction (E and F) are shown.

data for weak rip events in the plot of D_m and T_p (Figure 3.25B). The first cluster is in a similar location to the contours for strong rip events, while the second cluster occurs at shorter T_p values and around D_m values between 240 and 260 degrees (NW). In the plot of D_m and T_{01} however, the contours for weak rip events are concentrated only around the location of the second cluster (Figure 3.25D). A clearer separation between weak and strong rip events for T_{01} than T_p was also seen in the histograms in Figure 3.23B and C.

During the summer observational periods, waves of longer and shorter periods arrive from different directions. Longer period waves tend to approach from the south to south-southwest (D_m values between 180 - 200 degrees) (Figure 3.26 D), while

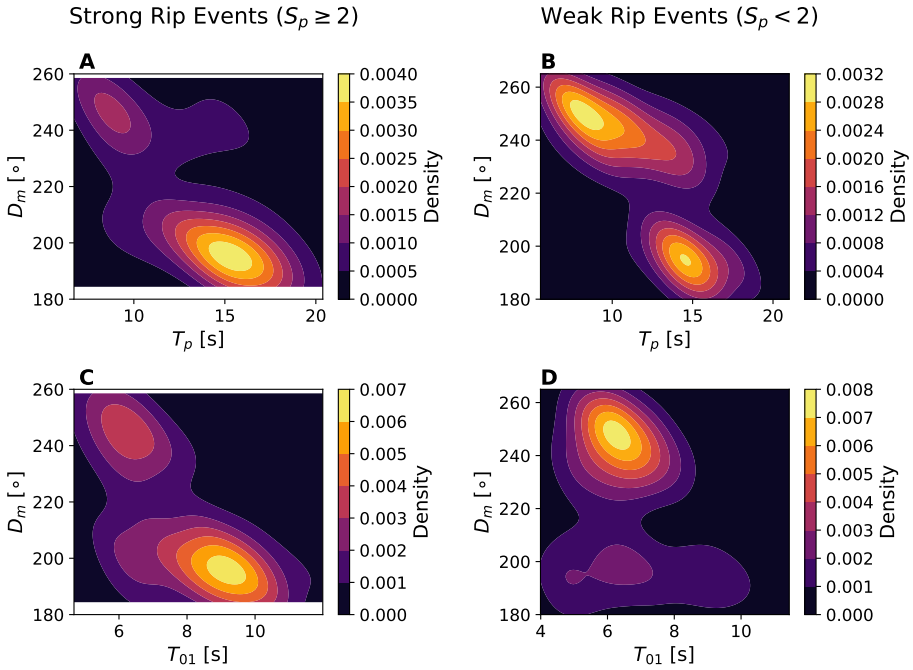

Figure 3.25: 2-D density contour plots for strong rip events (those with $S_p \geq 2$) and weak rip events (those with $S_p < 2$) at Lovekin Rock (Long Beach). Wave parameters are from the nearshore Spotter buoys 1881 (Wickaninnish Beach) and 1445 (Schooner Cove). The distributions of peak wave period with mean wave direction (A and B) and mean wave period with mean wave direction (C and D) are shown .

shorter waves tend to approach from closer to west-southwest (D_m values between 240 - 260 degrees) (Figure 3.26 E). This separation is not seen for mean wave direction vs significant wave height, as waves of all heights approach the beach from directions ranging from south to southwest (Figure 3.26 C). However; there is a slight trend of increasing T_{01} values with increasing H_s (Figure 3.26 B). These higher and longer waves that approach from the south tend to result in stronger rip current events at Lovekin Rock.

3.3.2 Occurrence Probabilities

The occurrence probability of a strong rip current is defined as the probability of the perceived strength rating for a rip current exceeding considerable, or $P(S_p \geq 2)$. $P(S_p \geq 2)$ increases with H_s and exceeds 50% for values greater than 1.5 m (Figure 3.27A). $P(S_p \geq 2)$ also increases with T_{01} and exceeds 50% for values greater than 8 s (Figure 3.27C). Strong rip current probability is greater than 50% for waves that

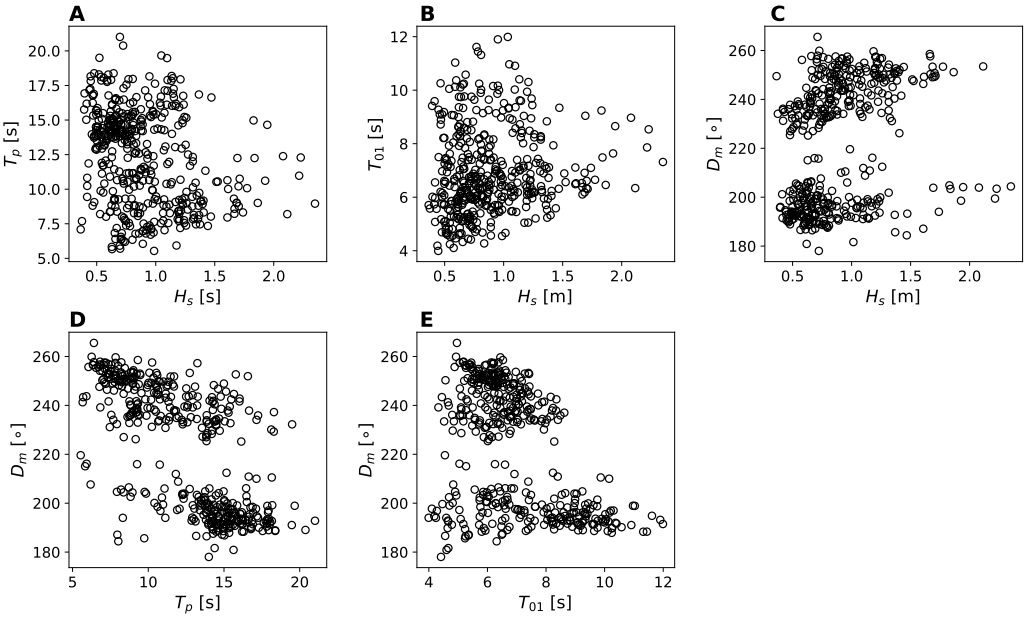

Figure 3.26: Scatter plots of wave parameters from nearshore Spotter buoys 1881 (Wickaninnish Beach) and 1445 (Schooner Cove) during observations of perceived rip current strength S_p at Lovekin Rock (Long Beach). Peak period vs significant wave height (A), mean spectral period vs significant wave height (B), mean wave direction vs significant wave height (C), mean wave direction vs peak period (D), and mean wave direction vs mean spectral period (E).

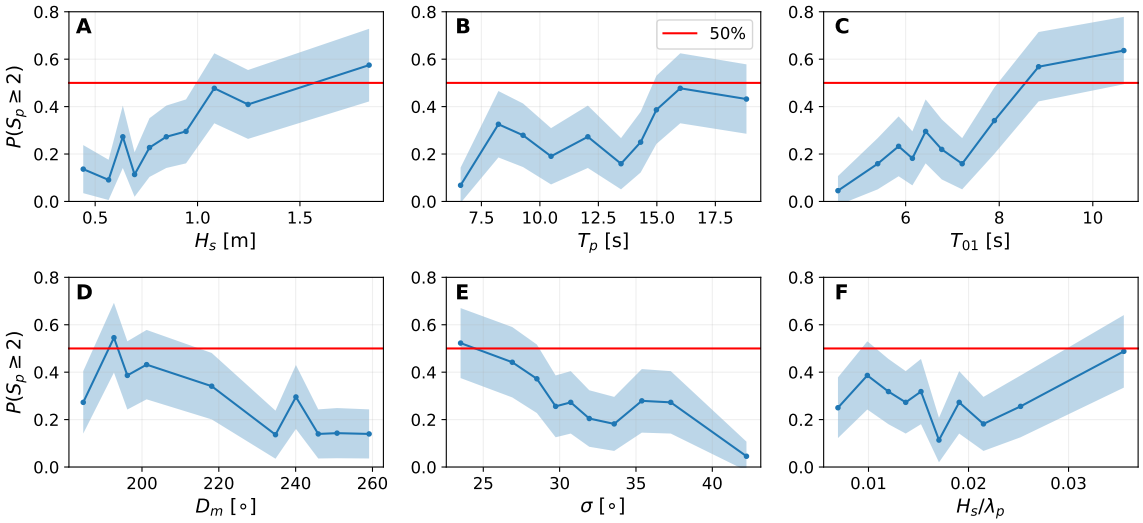

Figure 3.27: Strong rip current occurrence probability $P(S_p \geq 2)$ at Lovekin Rock for the bulk wave parameters calculated from Spotter wave buoys 1881 (Wickaninnish Beach) and 1445 (Schooner Cove). The wave parameters shown are significant wave height (A), peak period (B), mean spectral period (C), mean wave direction (D), directional spread (E), and peak wave steepness (F). The 95% confidence interval is shaded and the horizontal red line is at a probability of 50%.

approach from the south and for waves with narrow directional spread (Figure 3.27D and E). $P(S_p \geq 2)$ then decreases with increasing D_m and σ values.

Waves with larger H_s and T_{01} tend to have narrower directional spread during the observation period (Figure 3.28A, C), with the trend being stronger for mean spectral period. Wave with the narrowest directional spread also arrived from the south (D_m between 180 and 200 degrees) (Figure 3.28E).

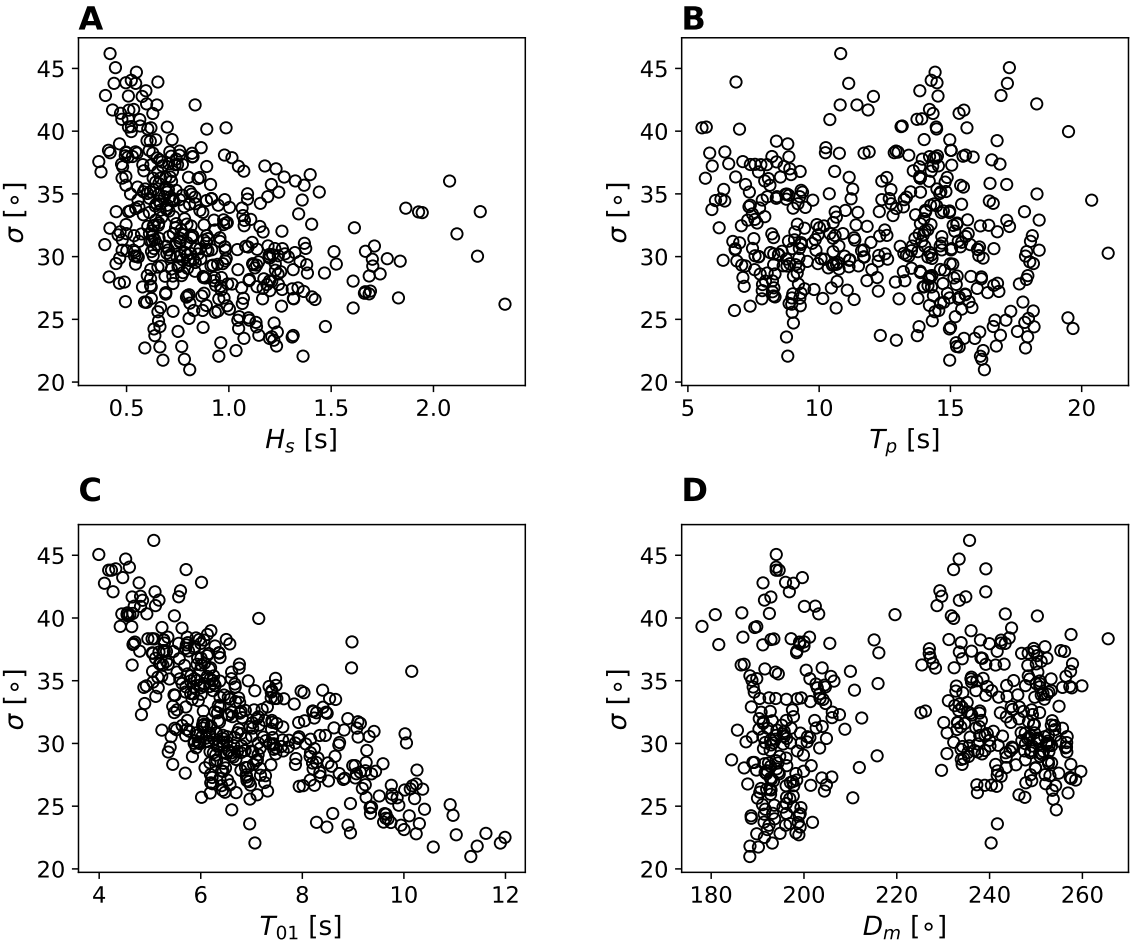

Figure 3.28: Scatter plots of directional spread plotted against significant wave height (A), peak period (B), mean spectral period (C), and mean wave direction (E) from Spotter wave buoys 1881 (Wickaninnish Beach) and 1445 (Schooner Cove) during observations of perceived rip current strength S_p at Lovekin Rock (Long Beach).

The strongest predictors of strong rip occurrence are larger values of H_s and longer values of T_{01}, which are characteristics of waves that tend to approach from the south with narrow directional spread. The influences of wave height and period indicate

that the non-standard wave parameters may also be good predictors of strong rip occurrence.

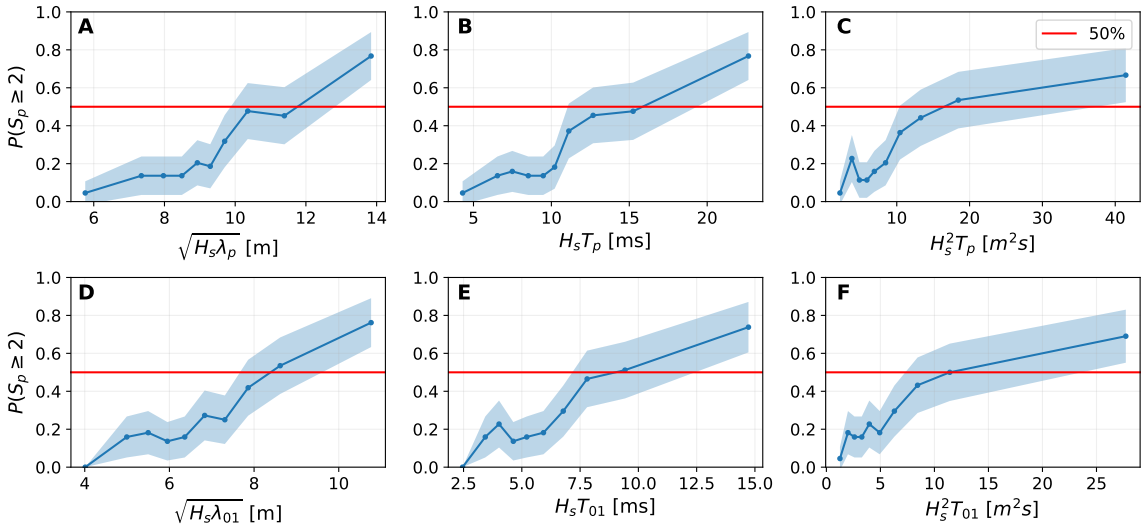

Figure 3.29: Strong rip current occurrence probability $P(S_p \geq 2)$ at Lovekin Rock for the non-standard wave parameters from Spotter wave buoys 1881 (Wickaninnish Beach) and 1445 (Schooner Cove). The parameters shown are the run-up parameter (A, D), wave factor (B, E), and the proxy for deep water wave energy flux (C, F). The 95% confidence interval is shaded and the red horizontal line is at a probability of 50%. Along the top row are the nearshore non-standard parameters calculated using peak period (A - C) and along the bottom row are the parameters calculated using mean spectral period (D - F).

The probability of a strong rip current increases with all six non-standard parameters and exceeds 50% for the greatest values of each (Figure 3.29). The run-up parameter and wave factor have the greatest maximum probability values, with $P(S_p \geq 2)$ reaching approximately 75% for each (Figure 3.29A, B, C, D). The maximum values of $P(S_p \geq 2)$ for wave energy flux are around 67 - 70 %(Figure 3.29C and F). Strong rip current occurrence probability follows a similar trend for each of the non-standard wave parameters and, as a result, any of these parameters would be good predictors of rip current strength

3.4 Lagrangian Rip Current Circulation

Deployments of surf zone drifters took place at Long Beach in July 2024 and August 2025. During both deployments the drifters showed both circulatory and exit behaviour and moved along both sides of Lovekin Rock. Drifter offshore velocities were greatest when they flowed offshore in the rip neck. The dye release in August 2025 showed similar flow behaviour to the drifters in both deployments. Dye released on the north side of the rock exited along the north side, while the dye released on the south side followed a counterclockwise circulation cell on the south side.

3.4.1 Surf Zone Drifters

Low-energy wave conditions occurred for all the drifter releases during July 2024 (Figure 3.30). Significant wave height values did not exceed 1 m for any of the drifter releases (Figure 3.30B). The greatest H_s value during the deployment was 0.7 m for the only drifter release on 8 July, and the second and third releases on 30 July. The lowest H_s value of 0.49 m occurred during the second release on 10 July. Peak wave periods were between 13 and 18 s (Figure 3.30C), and the mean wave directions were between 190 and 200 degrees, or south-southwest (Figure 3.30D). The first four releases took place at either the lower-low tide or the higher-high tide, while the last 11 releases on 30 and 31 July all took place as the tide was falling from the lower-high tide (Figure 3.30A).

Wave conditions for the drifter deployment on 8 August 2025 were similar to the conditions during the July 2024 deployment (Figure 3.31 B - D). The significant wave height was less than or equal to 1 m, the peak period was around 16 s, and the mean wave direction was from 200 degrees or south-southwest. The tide was around mid-tide, rising from low tide (Figure 3.31A).

The dominant drifter trajectory was circulatory which was observed in 17 of the 21 drifter releases (Table 3.3). Drifters that follow this trajectory remain in the surf zone as semi-enclosed vortices (Figures 3.32 and 3.33). Four circulations took place only on the north side of Lovekin Rock, and nine took place only on the south side. Exit behaviour was observed in five of the deployments, with the drifters flowing offshore past the rock and out of the surf zone. Of these five surf zone exits, two of the drifters moved only along the north side of Lovekin Rock and the other two moved only along the south side.

There were three instances in which drifters moved along and exhibited circula-

Date	Trajectory Type	Side of Rock	GPS Track Colour
8 July 2024	Circulatory - loop	North	Blue
10 July 2024	Circulatory - wide radius	South	Light Blue
	Circulatory - narrow radius	North	Light Blue
17 July 2024	Exit	South	Red
30 July 2024	Circulatory - wide radius	South	Blue
	Exit	North	Red
	Circulatory - partial	North	Light Blue
	Circulatory - wide radius	South	Blue
	Circulatory	North	Blue
31 July 2024	Circulatory then exit	South then north	Purple
	Circulatory - partial	South	Light Blue
	Circulatory - wide radius, partial	South	Light Blue
	Circulatory - narrow radius	South	Blue
	Exit	North	Red
	Exit	South	Red
8 Aug 2025	Circulatory	South	Blue
	Circulatory - partial	South	Light Blue
	Circulatory	North then south	Blue
	Circulatory	North then south	Light Blue
	Circulatory	South	Blue
	Circulatory then exit	South then north	Purple

Table 3.3: Summary of drifter circulation at Lovekin Rock rip current during July 2024 and August 2025 surf zone drifter deployments. The type of trajectory (circulatory or exit), the side of Lovekin Rock along which the drifters moved, and the colour of the corresponded GPS track are recorded.

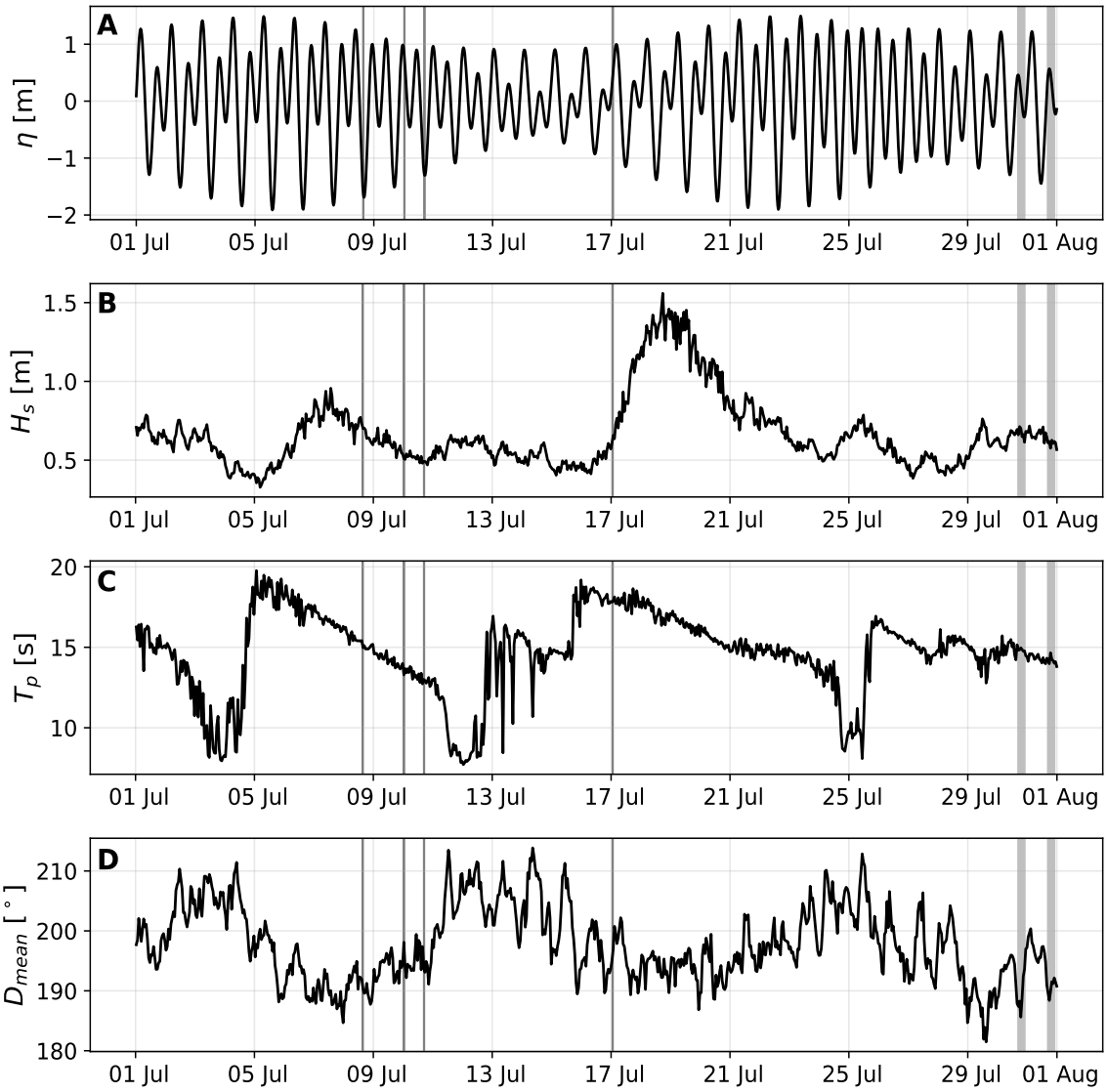

Figure 3.30: Tidal elevation (A), significant wave height (B), peak period (C), and mean wave direction (D) from Spotter buoy 1445 (Schooner Cove) for the July 2024 drifter deployment at Lovekin Rock (Long Beach). The vertical grey lines are at the drifter release times.

tory behaviour on both sides of Lovekin Rock. The first drifter released on July 31st completed a circulation on the south side of the rock before moving offshore in an apparent surf zone exit along the north side (Figure 3.32 right). Similar behaviour was observed three times during the August 2025 deployment. Two drifters released together both flowed offshore towards the Lovekin rock, completed a clockwise circulation on the north side, then changed direction and flowed offshore along the south

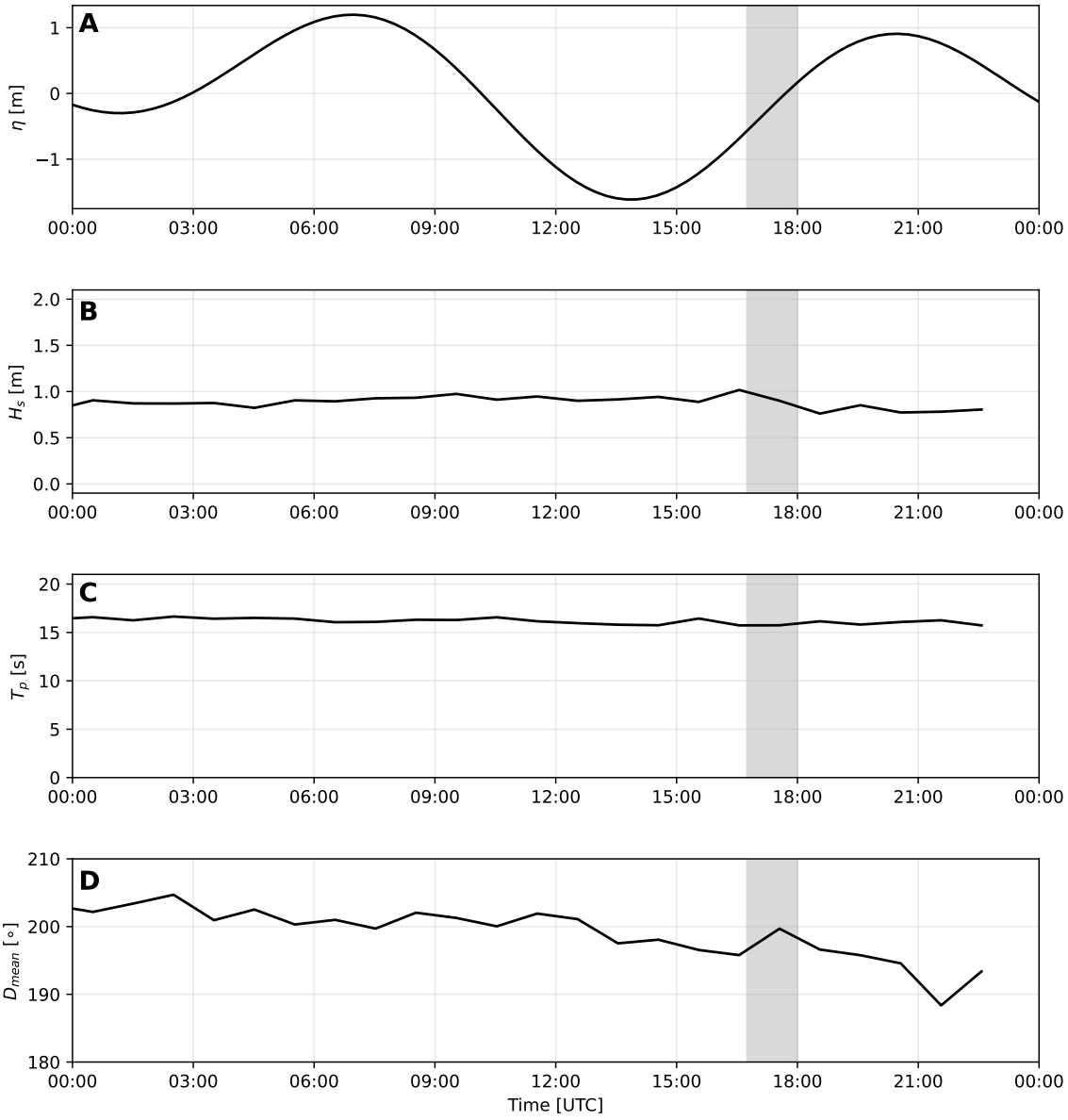

Figure 3.31: Tidal elevation (A), significant wave height (B), peak period (C), and mean wave direction (D) from Spotter buoy 1445 (Schooner Cove) for the 8 August 2025 drifter deployment at Lovekin Rock (Long Beach). The vertical grey shading shows the drifter deployment time.

side of the rock (Figure 3.33 middle). Both drifters were then pushed back onshore before washing up south of Lovekin Rock. There was one case in which a drifter moved along both sides of Lovekin Rock and showed exit and circulatory behaviour during the same release. One of the drifters released on the south side of Lovekin Rock in August 2025 completed four counterclockwise circulations on the south side

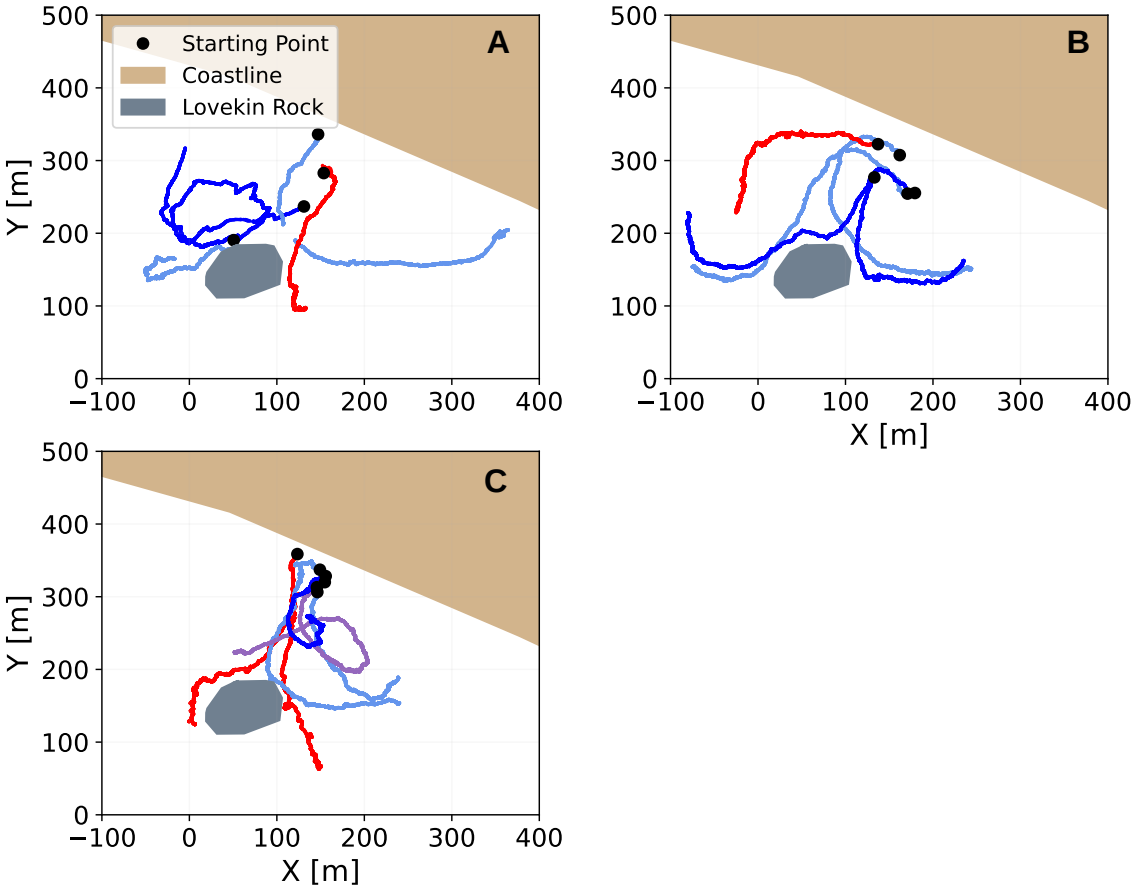

Figure 3.32: Drifter GPS tracks from July 2024 deployment. The coastline is shaded brown and Lovekin Rock is shaded grey. The black dots show the starting point of each drifter release. Drifter GPS tracks are coloured according to circulation behaviour: blue tracks show circulatory behaviour, red tracks show exit behaviour, and purple tracks show a mix of both behaviours. Drifter releases are from 8 and 10 July (A), 30 July (B), and 31 July (C).

of the Lovekin Rock before moving to the north side and completing one clockwise circulation before beginning to exit offshore (Figure 3.33 left). At this point the drifter was retrieved.

Although the drifters in August 2025 were released from different longshore locations relative to Lovekin Rock, all six entered the rip current and showed circulatory behaviour on both sides of the rock (Figure 3.33). Most of the circulations were counterclockwise and occurred on the south side of Lovekin Rock. Five of the six drifters washed up onshore south of Lovekin Rock, while Drifter 9 ended up flowing offshore on the north side (Figure 3.33).

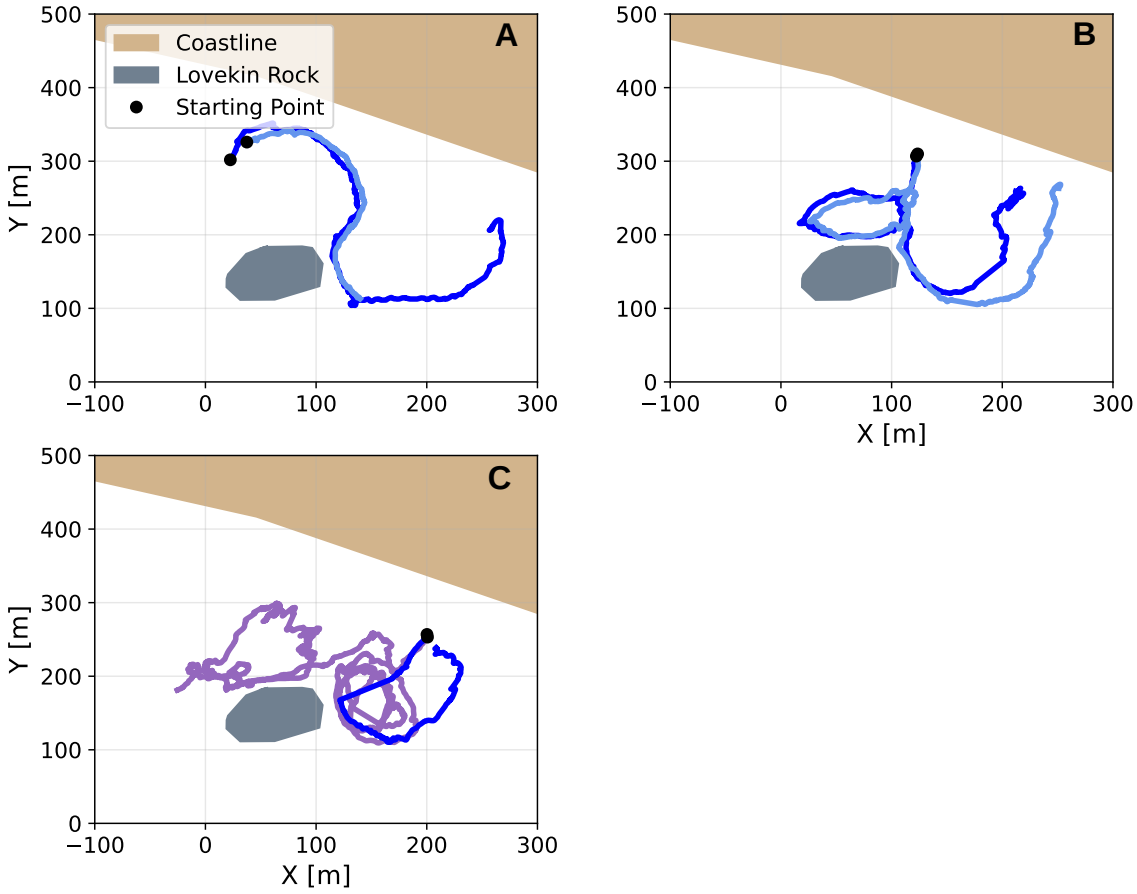

Figure 3.33: GPS drifter tracks for the drifter deployment on 8 August 2025. The coastline is shaded brown, Lovekin Rock is outlined and shaded grey. The black dots show the starting point of each drifter release. Drifter GPS tracks are coloured according to circulation behaviour: blue tracks show circulatory behaviour, red tracks show exit behaviour, and purple tracks show a mix of both behaviours. During the deployment, drifters were released on the north side of the rock (A), in front of the rock (B), and on the south side of the rock (C).

During the deployments on 30 July 2024, four of the five drifters initially moved alongshore towards the northwest before flowing offshore in the rip current (Figure 3.32 middle). This indicates that the longshore current was flowing north-west along the beach on this day. On 31 July, all the released drifters initially moved offshore with no longshore movement (Figure 3.32 right). The longshore current may have been weaker on this day. During the August 2025 deployment, the two drifters released on the north side of Lovekin Rock flowed alongshore in the south-east longshore current until they were in front of Lovekin Rock and then began to flow offshore

(Figure 3.31 left).

The drifter velocities were converted from GPS compass coordinates to a beach coordinate system, using the same conventions as the coordinate system at Wickaninnish Beach in Section 3.2; defined such that x is the alongshore direction (positive north along the beach) and y is the cross-shore direction (positive offshore).

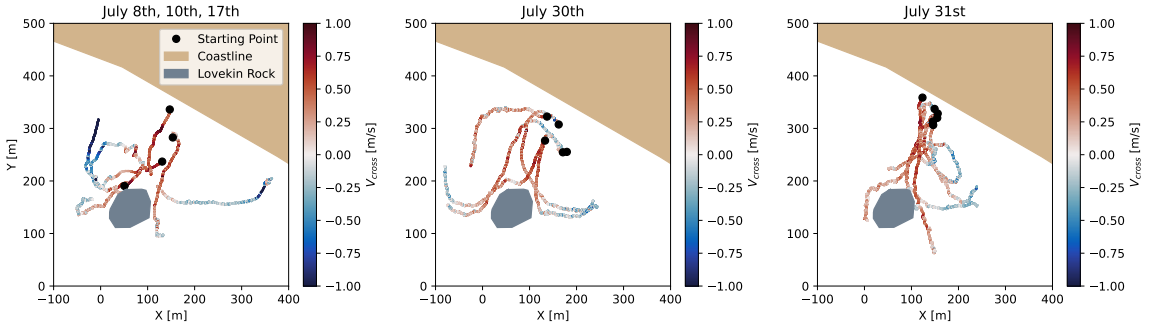

Figure 3.34: Drifter cross-shore velocities from July 2024 deployment. The coastline is shaded brown, Lovekin Rock is shaded grey, and the black dots show the starting point of each drifter release. The GPS tracks are coloured by drifter cross-shore velocity: red is offshore and blue is onshore.

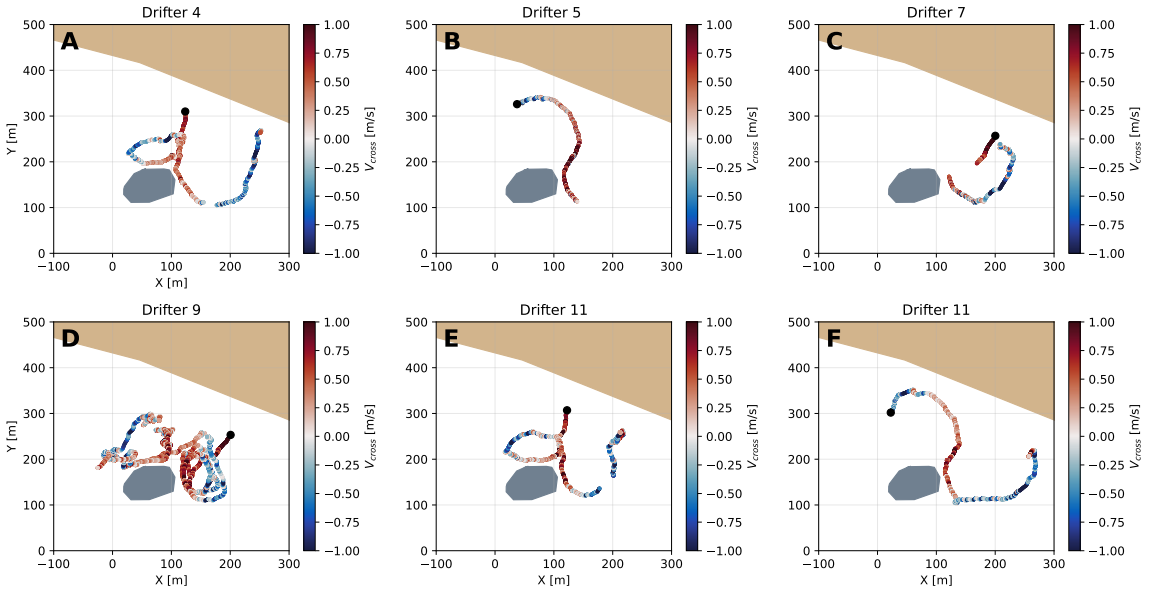

Figure 3.35: Drifter cross-shore velocities from 8 August 2025 deployment. The coastline is shaded brown, Lovekin Rock is shaded grey, and the black dots show the starting point of each drifter release. The GPS tracks are coloured by drifter cross-shore velocity: red is offshore and blue is onshore.

Drifter cross-shore velocities are greatest when the drifters are moving offshore through the rip neck, reaching velocities of 1 m/s or greater (Figures 3.34 and 3.35). The drifters tend to slow as they move closer to the outer edge of the rock. If the rip current shows exit behaviour, drifter cross-shore velocities decrease as they exit the rip and slow down. If the rip current shows circulatory behaviour, drifter cross-shore velocities also decrease towards zero as they begin to move alongshore. Once the drifters start moving back towards the shore, cross-shore velocities become negative.

3.4.2 Dye Release

Two dye releases were performed in collaboration with Parks Canada on 8 August 2025 following the drifter deployment. The first dye release began at 10:07 PDT (17:07 UTC). Two batches of dye were released on the north side of Lovekin Rock, with one batch released in approximately 1 m deep water and the other released beside the rock (Figure 3.36A). The nearshore dye initially moved south alongshore towards the centre of Lovekin Rock where it then entered the rip current and eventually flowed offshore along the north side of the rock (Figure 3.36 B - D). The dye released in deeper water was pushed towards the shore by the incoming waves. The nearshore dye moved offshore and alongside Lovekin Rock in approximately 6 minutes, while the dye released in deeper water showed little movement during this time.

The second dye release began at 10:39 PDT (17:39 UTC). Two batches of dye were released in approximately 1 m deep water on the north and south sides of Lovekin Rock (Figure 3.37A). The green dye released on the north side moved slightly south alongshore then entered the rip current and moved offshore along the north side of the rock (Figure 3.37 A - C). The green dye continued to flow offshore, eventually moving behind Lovekin Rock and out of the surf zone where it began to slow down (Figure 3.37 D-F). A rip head is visible in Figure 3.37F. The purple dye released on the south side moved north alongshore towards the centre of Lovekin Rock where it entered the rip and moved offshore (Figure 3.37B-D). The majority of the purple dye moved towards the south side of the rock and completed a counterclockwise circulation (Figure 3.37E, F). A small amount of the purple dye moved along the north side of the rock with the green dye. It took approximately 8 minutes for the green dye to move out of the surf zone and for the purple dye to complete a circulation.

The dye followed similar flow patterns to the drifters, exhibiting both exit and circulatory behaviour. The purple dye released on the south side of the rock com-

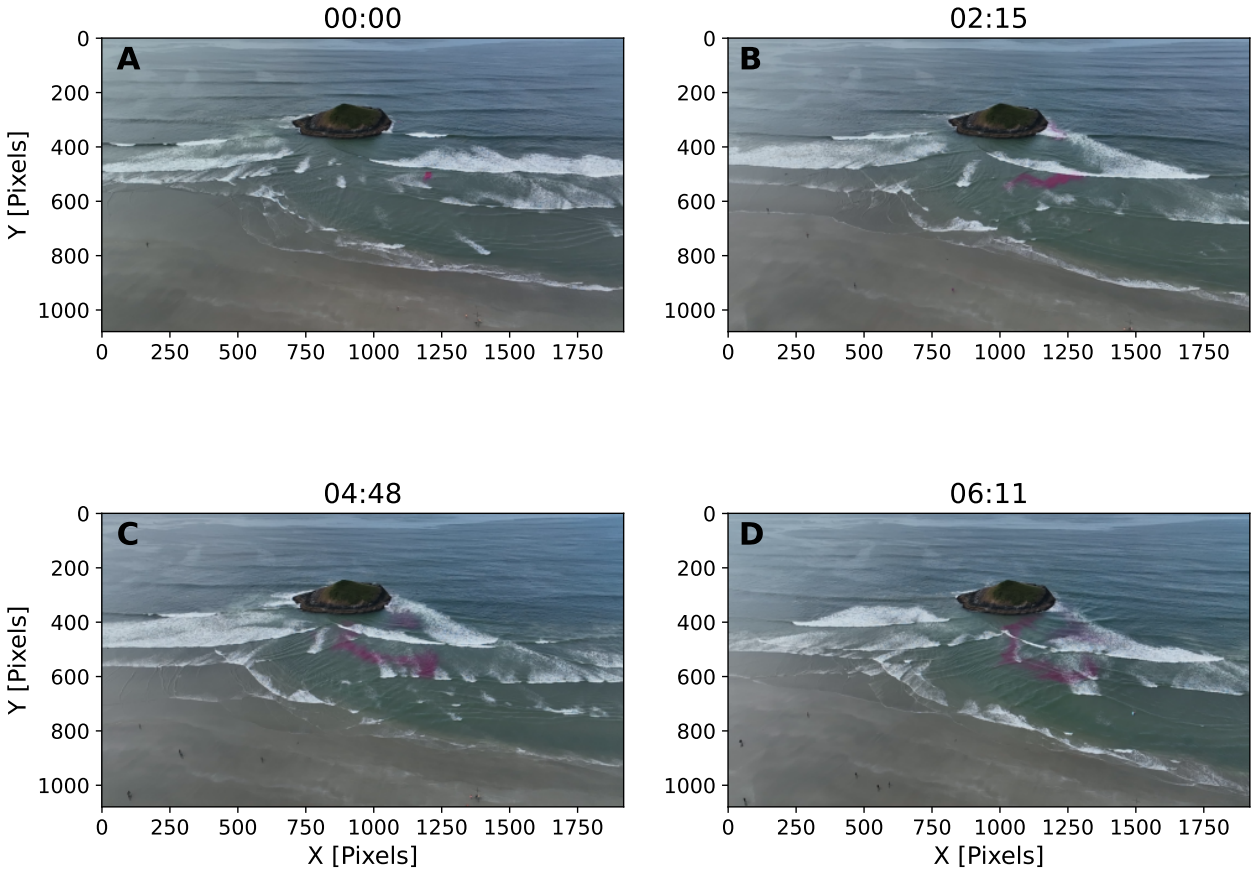

Figure 3.36: Stills from drone video of the first dye release on 8 August 2025. Each frame is labelled with the elapsed time since the dye entered the water (minutes:seconds) and progress from frame A to D. The axes units are in pixels.

pleted a counterclockwise circulation similar to that shown in the drifter GPS tracks (Figures 3.32 and 3.33). When Drifter 9 moved to the north side of Lovekin Rock, it completes a clockwise circulation and then begins to exit the surf zone similar to both dye releases on the north side of the rock.

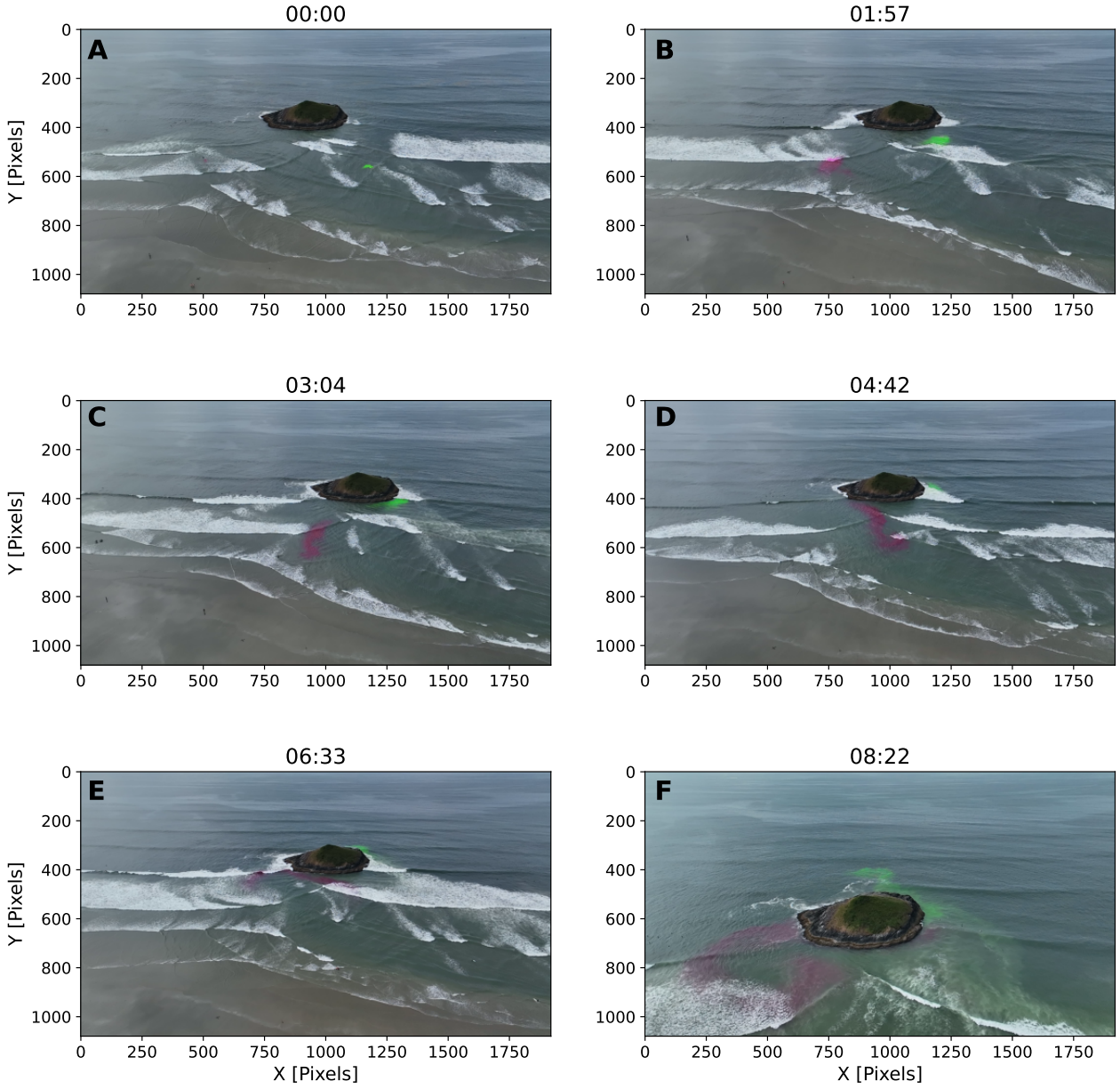

Figure 3.37: Stills from drone video of the first dye release on 8 August 2025. Each frame is labelled with the elapsed time since the dye entered the water (minutes:seconds) and progress from frame A to D. The axes units are in pixels.

Chapter 4

Discussion

4.1 Datasets

Observations of perceived rip current strength were made during the summer months (May to September) when wave energy is relatively low compared to the fall and winter months. While this does limit an examination of the effects of extreme values of wave parameters on perceived rip current strength, the summer season at PRNPR brings in large numbers of tourists, many of whom are inexperienced surfers or swimmers who are more likely to be unaware of the dangers posed by rip currents. It is important to determine when the rip currents are strongest during this time of year, when more people are likely to encounter the rip.

As the estimations of perceived rip current strength and the camera observations are visual observational methods, a level of subjectivity is introduced. However, studies by Dusek and Seim (2013) and Reinhart and Pfaff (2016) have shown that lifeguard observations are an accurate proxy for rip current intensity. While the Parks Canada Coastal Stewards are not lifeguards, they are trained similarly in rip current identification.

Due to limitations in the dataset from the surf zone drifters, conclusions could not be made regarding the influence of wave conditions or the tide on rip current speed and circulation. The rip current perceived strength estimations were averaged over periods of three hours and could not be matched with specific tidal elevations or motions. The July 2024 and August 2025 drifter deployments took place during similar low-energy wave conditions, with little variation in the tide. Logistical challenges in finding a volunteer willing to assist with the drifter deployments and retrievals resulted in a

smaller dataset than anticipated, with a total of 21 releases. Despite these challenges, the deployments did reveal important information about the circulation structure of the Lovekin Rock rip current, confirming that the rip current either exits the surf zone or recirculates back into shallow water, and may move along either side of Lovekin Rock. Both behaviours have been observed by Parks Canada Coastal Stewards and surfers in the area.

Rip current pulsations in the infragravity (25 - 250 s) and very low frequency (4 - 30 minutes) bands have been observed in previous studies (Austin et al., 2010; Bruneau et al., 2009; MacMahan et al., 2004). Since the ADCP velocity measurements are averaged over 5 minutes, information at periods shorter than 10 minutes cannot be resolved. Spectra of the cross-shore and alongshore velocities confirm this, showing that spectral power is concentrated in the tidal frequency band (Figure 4.1).

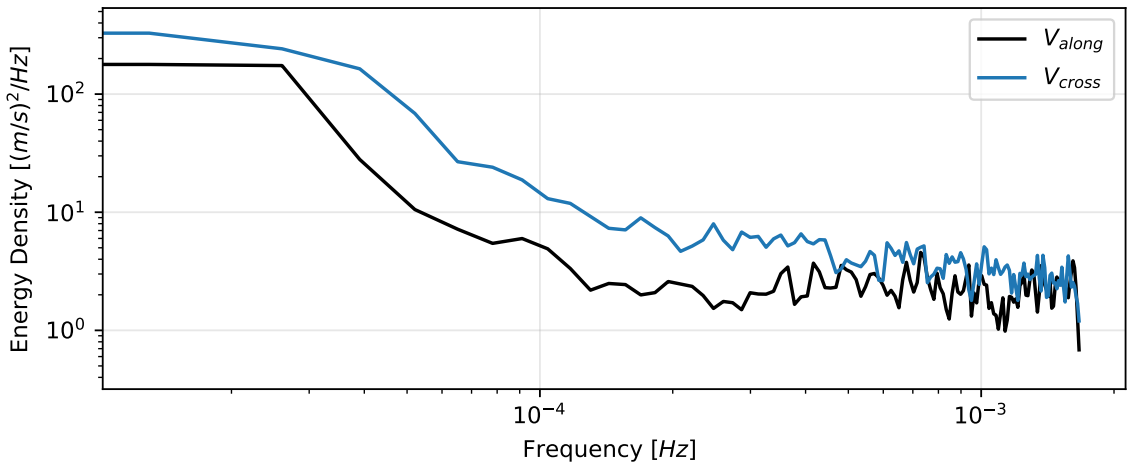

Figure 4.1: Spectra of along- and cross-shore velocities measured by ADCP at Wickaninnish Beach. The 95% confidence intervals are shaded.

This research combines datasets from visual, Eulerian, and Lagrangian observational methods. While each individual dataset has its limitations, combining the four datasets provides a set of comprehensive results about the environmental factors that influence rip current characteristics in Pacific Rim National Park Reserve.

4.2 Environmental Controls

Significant wave height H_s was found to influence structurally-controlled rip current flow characteristics at both study locations. Occurrence and speed of the shadow rip

current at Wickaninnish Beach increased with H_s, with rip occurrence probability exceeding 50% for H_s values greater than 1.8 m. Reinhart and Pfaff (2016) found an increase in rip current events with larger waves. Pattiaratchi et al. (2009) and Scott et al. (2016) similarly found that the speed of rip currents controlled by groynes increases with H_s. A similar influence of wave height on bathymetrically-controlled rips has been well documented (Carpi et al., 2021; Criado-Sudau et al., 2019; MacMahan et al., 2005, 2023; Scott et al., 2018). Rip current perceived strength at Lovekin Rock was also seen to increase with H_s. Dusek and Seim (2013) also found that rip current strength estimations from lifeguards increased with H_s. Wave energy is proportional to H_s^2. Energy is dissipated and transferred from breaking waves to drive nearshore currents. When larger waves break, more energy is transferred to longshore flow and rip currents. The increase in rip occurrence probability with H_s suggests that sufficient energy must be transferred from the breaking waves in order to drive rip current flow. The increased energy transfer from higher waves also results is faster/stronger nearshore currents, as was seen at Lovekin Rock and at Wickaninnish Beach. ADCP results at Wickaninnish Beach also showed a strong positive correlation between rip velocity and H_s^2.

At both locations incident wave period was found to have a secondary influence on rip current flow, with all three rip current characteristics increasing with mean spectral period T_{01}. Peak period T_p was also seen to influence perceived strength, however, to a lesser degree than T_{01}. The mean spectral period T_{01} is more stable over short timescales than peak wave period T_p (Figure 3.11C) and may better reflect changes in the wave field than T_p (Figure 3.11 B and C), performing better as a predictive parameter for rip current characteristics. Pattiaratchi et al. (2009) found that the speed of a shadow rip current increased with longer wave periods, although the influence was less than that of H_s. Engle et al. (2002) found that more rip related rescues took place during long period wave conditions. Carpi et al. (2021), Criado-Sudau et al. (2019), and Dusek and Seim (2013) also found that rip current strength/speed increased with longer period waves.

Higher and longer waves were found to be favourable for increased occurrence, speed, and strength of structurally-controlled rips in PRNPR. The combined influence of these waves can be represented by the two non-standard parameters: wave factor H_sT_{01} (Scott et al., 2014) and a proxy for wave energy flux $H_s^2T_{01}$. Higher and longer waves break further from shore, which results in greater set-up in the surf zone (Battjes, 1988). In the case of a nearshore structure, the wave set-up will be much

lower in the lee, or shadow, of the structure than outside. Increased set-up outside the shadow region will result in a stronger alongshore pressure gradient, and thus, a faster longshore current towards the region of low set-up. The resulting offshore rip current flow will also be faster. H_sT_{01} was found by Scott et al. (2014) to be a key parameter controlling rip behaviour. Castelle et al. (2024) also found the rip current hazard increased with greater wave factor values. Strong correlations were seen between rip velocity and both H_sT_{01} and $H_s^2T_{01}$. As wave height was seen to influence rip current flow more than wave period, $H_s^2T_{01}$ better represents the relative importance of each parameter. An increased rate of wave energy transfer seems to result in faster rip current flow. Both non-standard parameters could be used as predictors of rip current velocity, as wave height and period are standard outputs of wave buoys and models.

Rip current speed at Wickaninnish Beach appeared to have moderate positive correlations with both mean wave direction D_m, as waves approached closer to west-southwest, and directional spread σ. During the 10 day ADCP deployment in October to November 2023, waves that approached from these directions tended to be higher and have greater directional spreading (Figure 3.13). The long-term dataset from the camera observation period shows no clear trend between mean wave direction and significant wave height (Figure 4.2 left). While larger waves do not always have greater directional spread, the range of σ values does increase for larger waves (Figure 4.2 right). Waves with H_s values less than 1.5 m tend to have σ values between 20 and 50°, while σ ranges between 20 and 80 degrees for H_s values greater than 1.5 m. Larger waves can arrive from directions between 180 degrees and 260 degrees (south to west-southwest) at Wickaninnish Beach, so further ADCP deployments at this location during varying wave conditions would be required to fully examine the influence of D_m and σ on rip current speed. Waves approaching from the south with narrow directional spread resulted in stronger rip currents at Lovekin Rock. It was found that during the summer seasons at Long Beach, these waves tended to have greater values of H_s and T_{01}, characteristics that were seen to result in stronger rip currents. As with Wickaninnish Beach, observations of perceived rip current strength at Lovekin Rock during the rest of the year would be required to further examine the influences of D_m and σ.

Rip occurrence at Wickaninnish Beach was not influenced by D_m, although D_m and σ have been seen to influence some structurally-controlled rips. Scott et al. (2016) showed for rip currents controlled by groynes, a larger wave angle results in

stronger rip current flow. Castelle and Coco (2012) found that the presence of a headland rip on an embayed beach increased with greater directional spreading of the wave field. Groynes are regular shore-connected structures, differing from the offshore group of rocks at Wickaninnish Beach. Wickaninnish Beach is also a long sandy beach, differing from the embayed beach in the study of Castelle and Coco (2012).

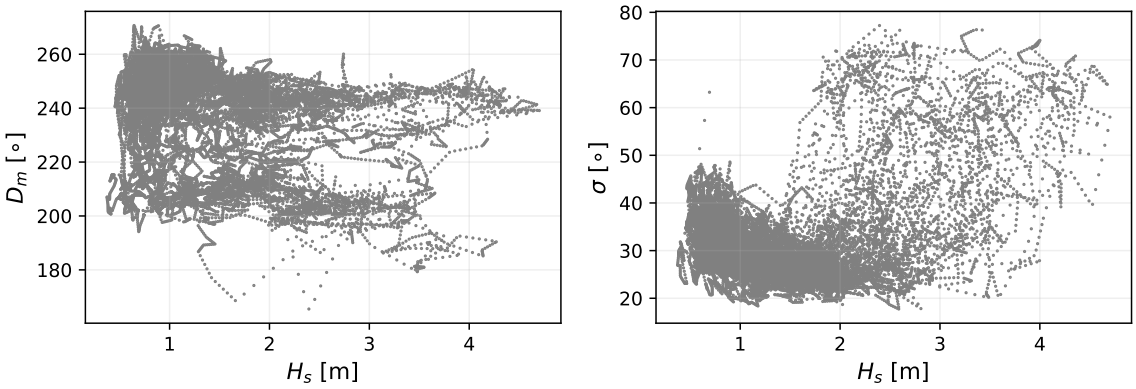

Figure 4.2: Scatter plots of mean wave direction (left) and directional spread (right) vs significant wave height from Spotter buoy 1881 (Wickaninnish Beach) during the camera observational period (August 2023 - January 2025).

Tidal elevation and tidal motion were not found to influence rip current occurrence or speed at Wickaninnish Beach. Bathymetrically-controlled rip currents have been found to be tidally modulated, with rip speeds increasing towards low tide (Austin et al., 2010; Brander and Short, 2001; MacMahan et al., 2005; Winter et al., 2014, for example) when low water levels favourably expose morphological features for rip formation. The influence of tides on structurally-controlled rip currents is less clear. McCarroll et al. (2014) found that on an embayed beach with headland rip currents, rip speed increased towards low tide. This beach type differs from the beaches in Pacific Rim National Park, which are long, sandy and dissipative. The offshore rocks at Wickaninnish Beach and Lovekin Rock also differ from the headland of an embayed beach. As noted by Scott et al. (2016), structurally-controlled rip currents are likely to be tidal modulated in the cases where water level influences the wave field or the exposure of the structure, which would be a characteristic of the beach and structure. At Wickaninnish Beach, there is no time during the tidal cycle where the offshore rocks are left completely dry.

The vertical profiles of cross-shore rip velocity at Wickaninnish Beach were found

to be approximately depth-uniform through the first meter of the water column. Drønen et al. (2002) and Haas and Svendsen (2002) both found that as a first approximation the vertical profiles of cross-shore velocity are relatively uniform, with Haas and Svendsen (2002) finding a decrease in vertical variation in the velocity profiles during larger wave conditions. The strongest rip events at Wickaninnish Beach had a slight vertical shear, with offshore rip velocity increasing with depth. H_s values during these events were greater than 3 m. These profiles may have shown the presence of an undertow, as there was resemblance to the surf zone undertow profiles of Lentz et al. (2008), which show an increasing offshore velocity with depth. The surface rip flow may also be restricted by the onshore transport of the larger waves during these events, as observed by MacMahan et al. (2005). During slightly lower wave conditions, the velocity profiles tended to be more uniform with depth.

4.3 Qualitative Descriptions of Rip Current Flow

4.3.1 Wickaninnish Beach

ADCP measurements show that the longshore current at Wickaninnish Beach flows from north to south towards the rock outcrop (Figure 4.3A). When the rip current is active, the resulting flow at the ADCP location is offshore at an oblique angle relative to the shoreline (Figure 4.3C), and the magnitude of the resulting flow is stronger (Figure 4.3B). The longshore flow appears to be directed offshore by the presence of the offshore rock grouping.

This result indicates that the rip at Wickaninnish Beach behaves similarly to a rip current near a breakwater. Waves approach Wickaninnish Beach from the southwest, resulting in a shadow rip current in the lee of the rock outcrop (Figure 4.4). These waves are diffracted and refracted around the rocks, resulting in higher breaking waves outside of the lee, or shadow, of the rocks. This sets up a longshore pressure gradient towards the shadow region, and the resulting longshore current is driven towards the rocks where it is then directed offshore as a rip current.

The speed of the rip current at Wickaninnish Beach was found to be controlled primarily by wave height, with increasing speeds occurring with larger waves. Larger breaking waves result in greater set-up outside of the shadow region, where wave set-up is much lower. The increased wave set-up causes a greater longshore pressure gradient, a faster resulting longshore current towards the shadow region, and a faster

offshore-directed rip current (Figure 4.3A). The nearshore flow at the ADCP location has a greater magnitude and is more offshore-directed for greater significant wave height values (Figure 4.3B and C).

The rip circulation at Wickaninnish Beach was not mapped using Lagrangian methods, so it is not known if the rip exhibits exit or circulatory behaviour once it has moved offshore. Further observations with surf zone drifter or dye would need to be obtained.

4.3.2 Long Beach

Surf zone drifter deployments show that the rip current at Lovekin Rock can exit the surf zone along either side of the rock or circulate clockwise (counterclockwise) on the north (south) side in the shadow of the rock. This is similar to rip current flow at a single offshore breakwater as described by Liu and Mei (1976) and Suh and Dalrymple (1987).

Waves approaching Lovekin Rock are diffracted and refracted around both sides of the rock (Figure 4.5). The waves outside of the shadow region directly behind Lovekin Rock are larger than the waves inside this region. This results in greater set-up outside the shadow region than inside, and creates a longshore pressure gradient directed towards the shadow region. The longshore currents converge and then flow offshore as a rip current towards Lovekin Rock. When the rip current reaches the rock, it must diverge and flow towards either the north or south side of the rock. At this point the rip current can either exit the surf zone along Lovekin Rock or circulate back into the surf zone (Figure 4.5). The drifter deployment and dye release on 8 August 2025 showed that both behaviours may occur on either side of the rock at the same time. The circular shape of Lovekin Rock may allow more surf zone exits than the single offshore breakwater.

Similarly to the rip current at Wickaninnish Beach, the strength of the rip current at Lovekin Rock is also controlled primarily by wave height, with stronger rip flow resulting from larger waves. These waves result in greater wave set-up outside of the shadow region, where the wave set-up is much lower. Stronger longshore pressure gradients, and thus stronger longshore currents, are directed to the shadow region, where they converge and a stronger rip current flows offshore.

In the case of the offshore breakwater, incident wave direction influences the relative size and location of the circulation cells (Liu and Mei, 1976). In the case of

Lovekin Rock, this would likely influence which side of the rock the rip current tends towards; however, more observations during varying wave conditions would be needed to confirm this.

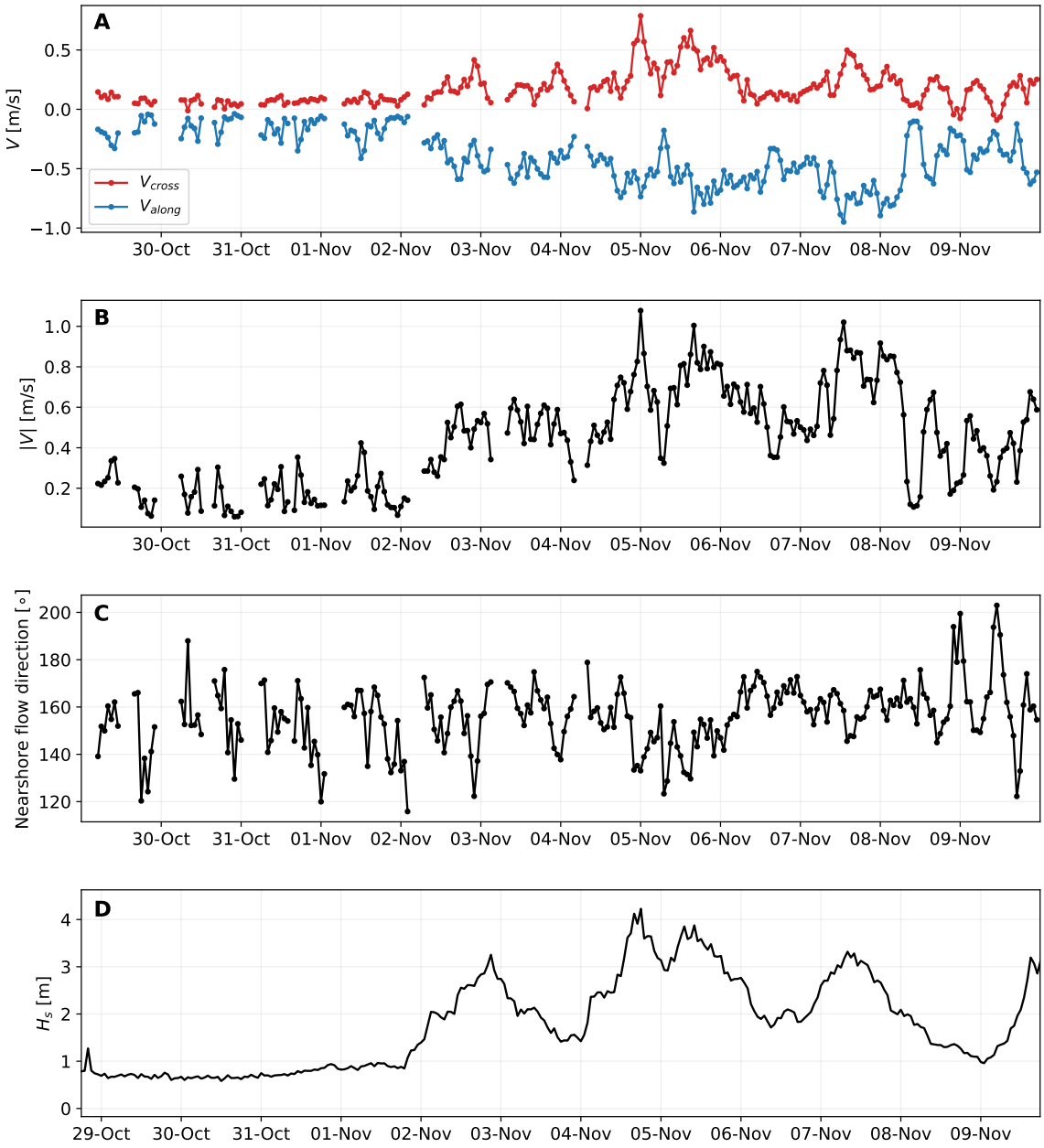

Figure 4.3: Time series of hourly maximum cross- and alongshore velocities (A), velocity magnitude (B), and flow direction (C) of the rip current at Wickaninnish Beach as measured by the ADCP. A time series of significant wave height during the ADCP deployment is also shown (D). The alongshore velocity is negative if it is directed north to south along the beach.

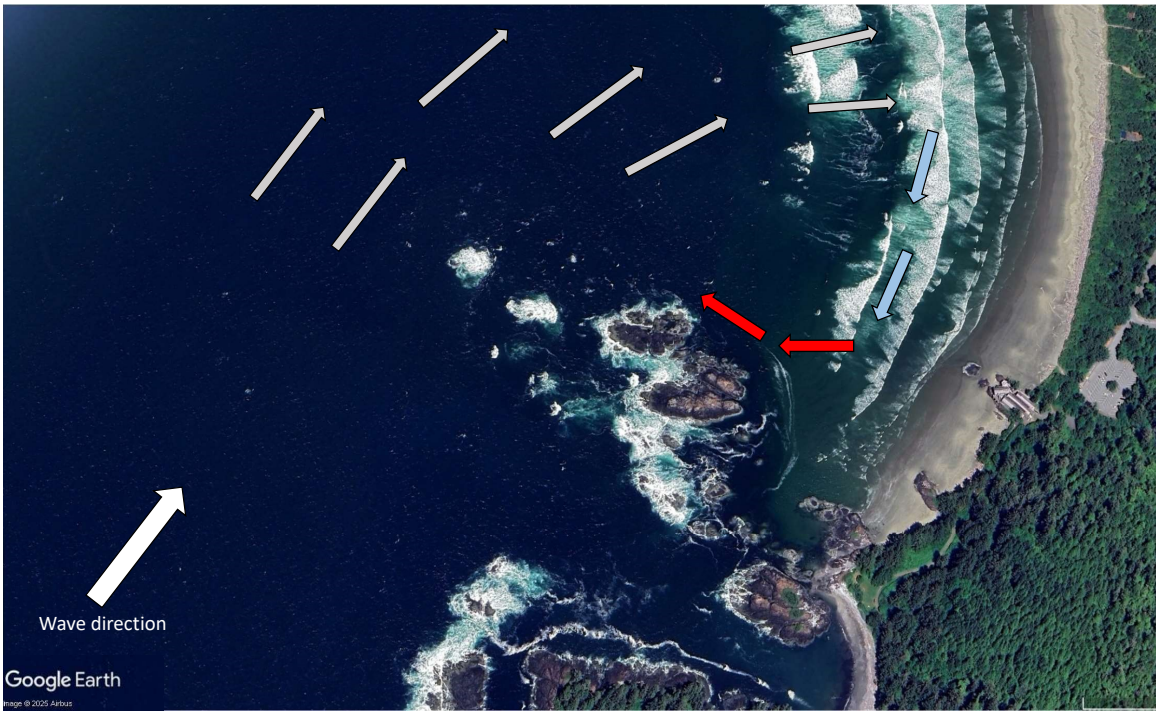

Figure 4.4: Shadow rip current flow at Wickaninnish Beach.

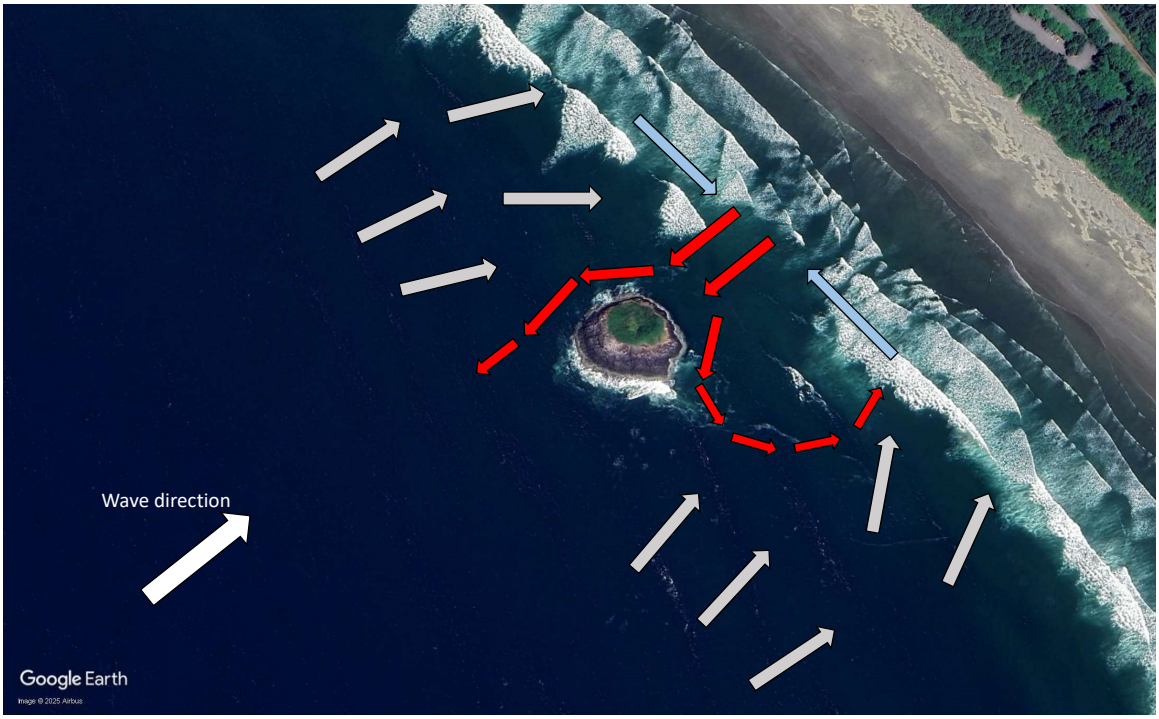

Figure 4.5: Rip current flow at Lovekin Rock as observed on 8 August 2025.

Chapter 5

Summary and Future Work

Field observations of rip currents were made at two locations in Pacific Rim National Park (PRNPR) where rip currents are controlled by the presence of offshore rocks. At Wickaninnish Beach, an infrared camera captured images of the shadow rip current for 300 days and an ADCP was deployed for 10 days to obtain measurements of the rip velocity. At Long Beach, visual estimations of perceived rip current strength at Lovekin Rock were made by Parks Canada Coastal Stewards for the summer months of 2022 - 2024, and surf zone drifters were deployed into the rip current in July 2024 and August 2025. The drifter release in August 2025 was accompanied by a dye release. Wave and tidal effects on rip current occurrence, speed, and strength were examined.

Significant wave height H_s was found to be a key parameter in controlling the occurrence, perceived strength, and speed of the rip currents at both location. Mean spectral period T_{01} was an important secondary factor in controlling rip current characteristics. These findings agree with previous studies concerning wave controls on rip currents near regular shore-connected structures (Pattiaratchi et al., 2009; Scott et al., 2016). Rip currents occur more frequently with larger waves and are stronger when the waves are larger and longer, indicating that increased incident wave energy is an important driver of structurally-controlled rip current flow. Rip speed and strength were also compared to three non-standard parameters: the parameter $\sqrt{H_s\lambda}$ used in predictions of run-up (Stockdon et al., 2006), wave factor H_sT (Scott et al., 2014), and a proxy for deep water wave energy flux H_s^2T (Scott et al., 2011). While both rip characteristics were found to increase with all three parameters, rip current speed showed the best correlation with $H_s^2T_{01}$, a parameter which represents the relative influence of H_s and T_{01} on rip current speed. This indicates that an increased

transfer of incident wave energy results in faster rip current flow.

Mean wave direction and directional spread had some influence on the rip currents at both locations, in that waves favourable for increased rip speed and strength tended to arrive from certain directions. At Wickaninnish Beach, higher waves tended to approach from directions closer to west-southwest and with greater directional spread, while higher and longer waves approached Long Beach from south-southwest with narrow directional spread. Steeper waves seemed to result in increased rip occurrence and speed, primarily driven by increasing wave height. Tidal elevation and motion did not influence rip speed or occurrence at Wickaninnish Beach.

While the rip current flow at Wickaninnish Beach was not mapped using Lagrangian methods, ADCP velocity measurements showed that the longshore current is directed offshore by the presence of the offshore group of rocks. The speed of the shadow rip current at this location was found to be influenced by significant wave height and, to a lesser extent, wave period, agreeing with the findings of Pattiaratchi et al. (2009), who also examined shadow rip currents in the field. As there are fewer field studies of shadow rip currents than deflection rip currents, this study and its results are of particular significance.

Further ADCP deployments could be done at Wickaninnish Beach over a longer time period and during different seasons to obtain observations of the rip current during differing wave conditions. Potential seasonality of the rip current flow could be examined. Sampling at a higher frequency would also allow investigation of rip current infragravity and very low frequency (VLF) pulsations.

Surf zone drifter deployments and a dye release showed the rip circulation at Lovekin Rock to be highly variable. Both exit and circulatory behaviour were observed, even during the same deployments. The rip may exit or recirculation into the surf zone on either side of the rock. The circulation of this rip current behaves similarly to a rip current controlled by a single offshore breakwater (Liu and Mei, 1976).

Changes in structurally-controlled rip circulation have been tied to changes in incident wave angle and/or the tide (Castelle and Coco, 2012, 2013; McCarroll et al., 2014; Scott et al., 2016). Further drifter observations at Lovekin Rock during a variety of wave conditions and tidal elevations would be needed in order to examine potential influences on the rip circulation. The Lagrangian methods (surf zone drifters, dye release) employed at Lovekin Rock could also be used to examine rip circulation at Wickaninnish Beach and determine how the rip behaves once it moves offshore.

Observations of perceived rip current strength at Lovekin Rock are only made during the summer months (May - September). During these months, wave energy in the northeast Pacific is relatively low compared to the fall and winter months. Due to increased tourism to the beach, the summer months are an important time of the year to examine the rip at Lovekin Rock. However, year-round observations of rip current perceived strength would allow for an examination of the effect of extreme wave conditions. A survey of perceived rip current strength has been developed for Lovekin Rock and will be distributed to experienced surfers in the region in an attempt to obtain year-round observations.

This work has been an important first step in studying structurally-controlled rip currents in PRNPR. Larger wave height and longer wave periods have been identified as conditions that lead to increased occurrence and the development of faster and stronger, and thus more dangerous, rip currents. Mapping of the rip current flow at Lovekin Rock revealed the rip circulation to be highly variable. These observations and results can be used not only to further improve beach safety at Wickaninnish and Long Beach, but also in the future development and validation of a rip current forecast system for PRNPR.

Bibliography

Austin, M. J., Masselink, G., Scott, T. M., & Russell, P. E. (2014). Water-level controls on macro-tidal rip currents. *Continental Shelf Research*, *75*, 28–40. https://doi.org/10.1016/j.csr.2013.12.004

Austin, M. J., Scott, T., Brown, J., Brown, J., MacMahan, J., Masselink, G., & Russell, P. (2010). Temporal observations of rip current circulation on a macro-tidal beach. *Continental Shelf Research*, *30*(9), 1149–1165. https://doi.org/10.1016/j.csr.2010.03.005

Austin, M. J., Scott, T. M., Russell, P. E., & Masselink, G. (2012). Rip current prediction: Development, validation, and evaluation of an operational tool. *Journal of Coastal Research*, *29*(2), 283. https://doi.org/10.2112/JCOASTRES-D-12-00093.1

Battjes, J. A. (1988). Surf-zone dynamics. *Annual Review of Fluid Mechanics*, *20*(1), 257–291.

Bosboom, J., & Stive, M. (2023, January). *Coastal Dynamics* (1.2). TU Delft.

Bowen, A. J. (1969). Rip currents: 1. Theoretical investigations. *Journal of Geophysical Research*, *74*(23), 5467–5478. https://doi.org/10.1029/JC074i023p05467

Bowen, A. J., & Inman, D. L. (1969). Rip currents: 2. Laboratory and field observations. *Journal of Geophysical Research*, *74*(23), 5479–5490. https://doi.org/10.1029/JC074i023p05479

Brander, R. W., & Short, A. D. (2001). Flow Kinematics of low-energy rip current systems. *Journal of Coastal Research*, *17*(2), 468–481.

Brewster, B. C., Gould, R. E., & Brander, R. W. (2019). Estimations of rip current rescues and drowning in the United States. *Natural Hazards and Earth System Sciences*, *19*(2), 389–397. https://doi.org/10.5194/nhess-19-389-2019

Bruneau, N., Castelle, B., Bonneton, P., Pedreros, R., Almar, R., Bonneton, N., Bretel, P., Parisot, J.-P., & Sénéchal, N. (2009). Field observations of an evolving rip current on a meso-macrotidal well-developed inner bar and rip morphol-

ogy. *Continental Shelf Research*, *29*(14), 1650–1662. https://doi.org/10.1016/j.csr.2009.05.005

Carpi, L., Mucerino, L., Bonello, G., Besio, G., & Ferrari, M. (2021). Rip currents investigation on a Ligurian pocket beach, NW Mediterranean. *Estuarine, Coastal and Shelf Science*, *262*, 107579. https://doi.org/10.1016/j.ecss.2021.107579

Castelle, B., Almar, R., Dorel, M., Lefebvre, J.-P., Senechal, N., Anthony, E. J., Laibi, R., Chuchla, R., & Penhoat, Y. D. (2014). Rip currents and circulation on a high-energy low-tide-terraced beach (Grand Popo, Benin, West Africa). *Journal of Coastal Research*, *70*, 633–638. https://doi.org/10.2112/SI70-107.1

Castelle, B., & Coco, G. (2012). The morphodynamics of rip channels on embayed beaches. *Continental Shelf Research*, *43*, 10–23. https://doi.org/10.1016/j.csr.2012.04.010

Castelle, B., & Coco, G. (2013). Surf zone flushing on embayed beaches. *Geophysical Research Letters*, *40*(10), 2206–2210. https://doi.org/10.1002/grl.50485

Castelle, B., Dehez, J., Savy, J.-P., Marieu, V., Lyser, S., Bujan, S., Carayon, D., & Brander, R. (2024). Environmental controls on lifeguard-estimated surf-zone hazards, beach crowds, and resulting life risk at a high-energy sandy beach in southwest France. *Natural Hazards*, *120*(2), 1557–1576. https://doi.org/10.1007/s11069-023-06250-0

Castelle, B., Scott, T., Brander, R., & McCarroll, R. (2016). Rip current types, circulation and hazard. *Earth-Science Reviews*, *163*, 1–21. https://doi.org/10.1016/j.earscirev.2016.09.008

Criado-Sudau, F. F., Nemes, D. D., & Gallo, M. N. (2019). Rip currents dynamic of a swell dominated microtidal beach. *Journal of Coastal Research*, *92*(sp1), 121. https://doi.org/10.2112/SI92-014.1

Dalrymple, R. A., MacMahan, J. H., Reniers, A. J. H. M., & Nelko, V. (2011). Rip currents. *Annual Review of Fluid Mechanics*, *43*(1), 551–581. https://doi.org/10.1146/annurev-fluid-122109-160733

Drønen, N., Karunarathna, H., Fredsøe, J., Mutlu Sumer, B., & Deigaard, R. (2002). An experimental study of rip channel flow. *Coastal Engineering*, *45*(3-4), 223–238. https://doi.org/10.1016/S0378-3839(02)00035-2

Dusek, G., & Seim, H. (2013). Rip current intensity estimates from lifeguard observations. *Journal of Coastal Research*, *288*, 505–518. https://doi.org/10.2112/JCOASTRES-D-12-00117.1

ECCC. (n.d.). Historical Climate Data - Environment and Climate Change Canada. Retrieved April 20, 2026, from https://climate.weather.gc.ca/index_e.html

Engle, J., MacMahan, J., Thieke, R. J., Hanes, D. M., & Dean, R. G. (2002). Formulation of a rip current predictive index using rescue data.

Gallop, S. L., Bryan, K. R., Pitman, S. J., Ranasinghe, R., Sandwell, D. R., & Harrison, S. R. (2018). Rip current circulation and surf zone retention on a double barred beach. *Marine Geology*, *405*, 12–22. https://doi.org/10.1016/j.margeo.2018.07.015

Gourlay, M. R. (1974). Wave set-up and wave generated currents in the lee of a breakwater or headland. *Coastal Engineering 1974*, 1976–1995.

Haas, K. A., & Svendsen, I. A. (2002). Laboratory measurements of the vertical structure of rip currents. *Journal of Geophysical Research: Oceans*, *107*(C5). https://doi.org/10.1029/2001JC000911

Holthuijsen, L. H. (2007). *Waves in Oceanic and Coastal Waters*. Cambridge University Press.

Johnson, D., & Pattiaratchi, C. (2004). Transient rip currents and nearshore circulation on a swell-dominated beach. *Journal of Geophysical Research: Oceans*, *109*(C2), 2003JC001798. https://doi.org/10.1029/2003JC001798

Kim, I. H., Kim, I. C., & Lee, J. L. (2011). Rip current prediction system combined with a morphological change model. *Journal of Coastal Research*, (64).

Leatherman, S. B. (2017). Rip current measurements at three South Florida beaches. *Journal of Coastal Research*, *335*, 1228–1234. https://doi.org/10.2112/JCOASTRES-D-16-00124.1

Lentz, S. J., Fewings, M., Howd, P., Fredericks, J., & Hathaway, K. (2008). Observations and a model of undertow over the inner continental shelf. *Journal of Physical Oceanography*, *38*(11), 2341–2357. https://doi.org/10.1175/2008JPO3986.1

Lippmann, T. C., & Holman, R. A. (1989). Quantification of sand bar morphology: A video technique based on wave dissipation. *Journal of Geophysical Research: Oceans*, *94*(C1), 995–1011. https://doi.org/10.1029/JC094iC01p00995

Liu, P. L.-F., & Mei, C. C. (1976). Water motion on a beach in the presence of a breakwater: 2. Mean Currents. *Journal of Geophysical Research*, *81*(18), 3085–3094.

Longuet-Higgins, M., & Stewart, R. (1964). Radiation stress in water waves; a physical discussion with applications. *Deep-Sea Research*, *11*(4), 529–562.

MacMahan, J. H., Brown, J., Brown, J., Thornton, E., Reniers, A., Stanton, T., Henriquez, M., Gallagher, E., Morrison, J., Austin, M. J., Scott, T. M., & Senechal, N. (2010). Mean Lagrangian flow behavior on an open coast rip-channeled beach: A new perspective. *Marine Geology*, *268*(1-4), 1–15. https://doi.org/10.1016/j.margeo.2009.09.011

MacMahan, J. H., Reniers, A. J. H. M., Thornton, E. B., & Stanton, T. P. (2004). Infragravity rip current pulsations. *Journal of Geophysical Research: Oceans*, *109*(C1), 2003JC002068. https://doi.org/10.1029/2003JC002068

MacMahan, J. H., Thornton, E., Patria, N., Gon, C., & Denny, M. (2023). Rip currents off rocky-shore surge channels. *Journal of Geophysical Research: Oceans*, *128*(8), e2022JC019317. https://doi.org/10.1029/2022JC019317

MacMahan, J. H., Thornton, E. B., & Reniers, A. J. (2006). Rip current review. *Coastal Engineering*, *53*(2-3), 191–208. https://doi.org/10.1016/j.coastaleng.2005.10.009

MacMahan, J. H., Thornton, E. B., Stanton, T. P., & Reniers, A. J. (2005). RIPEX: Observations of a rip current system. *Marine Geology*, *218*(1-4), 113–134. https://doi.org/10.1016/j.margeo.2005.03.019

McCarroll, R. J., Brander, R. W., Turner, I. L., Power, H. E., & Mortlock, T. R. (2014). Lagrangian observations of circulation on an embayed beach with headland rip currents. *Marine Geology*, *355*, 173–188. https://doi.org/10.1016/j.margeo.2014.05.020

Moulton, M., Dusek, G., Elgar, S., & Raubenheimer, B. (2017). Comparison of rip current hazard likelihood forecasts with observed rip current speeds. *Weather and Forecasting*, *32*(4), 1659–1666. https://doi.org/10.1175/WAF-D-17-0076.1

Mouragues, A., Bonneton, P., Castelle, B., Marieu, V., Barrett, A., Bonneton, N., Detand, G., Martins, K., McCarroll, J., Morichon, D., Poate, T., Padilla, I. R., Scott, T., & Sous, D. (2020a). Field observations of wave-induced headland rips. *Journal of Coastal Research*, *95*(sp1), 578. https://doi.org/10.2112/SI95-113.1

Mouragues, A., Bonneton, P., Castelle, B., Marieu, V., Jak McCarroll, R., Rodriguez-Padilla, I., Scott, T., & Sous, D. (2020b). High-energy surf zone currents and headland rips at a geologically constrained mesotidal beach. *Journal of Geophysical Research: Oceans*, *125*(10), e2020JC016259. https://doi.org/10.1029/2020JC016259

Murray, T., Cartwright, N., & Tomlinson, R. (2013). Video-imaging of transient rip currents on the Gold Coast open beaches. *Journal of Coastal Research*, *165*, 1809–1814. https://doi.org/10.2112/SI65-306.1

Oakey, S., Chaffey, J., Dupont, F., Chapman, P., Hannah, C., & Greenberg, D. (n.d.). WebTide- Tidal Prediction Model. https://www.bio.gc.ca/science/research-recherche/ocean/webtide/index-en.php

Olsson, D., & Pattiaratchi, C. (2009). Field measurements of rip currents in the vicinity of coastal structures. *Coastal Engineering 2008: (In 5 Volumes)*, 914–926.

Pattiaratchi, C., Olsson, D., Hetzel, Y., & Lowe, R. (2009). Wave-driven circulation patterns in the lee of groynes. *Continental Shelf Research*, *29*(16), 1961–1974. https://doi.org/10.1016/j.csr.2009.04.011

Peregrine, D. (1998). Surf zone currents. *Theoretical and computation fluid dynamics*, *10*(1), 295–309.

Rainville, E., Thomson, J., Moulton, M., & Derakhti, M. (2023). Measurements of nearshore ocean-surface kinematics through coherent arrays of free-drifting buoys. *Earth System Science Data*, *15*(11), 5135–5151. https://doi.org/10.5194/essd-15-5135-2023

Reinhart, B. J., & Pfaff, S. (2016). Wave analysis for rip current forecasting in southeast North Carolina. https://doi.org/10.13140/RG.2.1.4948.9049

Schmidt, W. E., Woodward, B. T., Millikan, K. S., Guza, R. T., Raubenheimer, B., & Elgar, S. (2003). A GPS-tracked surf zone drifter. *Journal of Atmospheric and Oceanic Technology*, *20*(7), 1069–1075. https://doi.org/10.1175/1460.1

Scott, T., Austin, M., Masselink, G., & Russell, P. (2016). Dynamics of rip currents associated with groynes — field measurements, modelling and implications for beach safety. *Coastal Engineering*, *107*, 53–69. https://doi.org/10.1016/j.coastaleng.2015.09.013

Scott, T., Castelle, B., Almar, R., & Senechal, N. (2018). Controls on flash rip current hazard on low-tide terraced tropical beaches in West Africa. *Journal of Coastal Research*, *81*(sp1), 92–99. https://doi.org/10.2112/SI81-012.1

Scott, T., Masselink, G., Austin, M. J., & Russell, P. (2014). Controls on macrotidal rip current circulation and hazard. *Geomorphology*, *214*, 198–215. https://doi.org/10.1016/j.geomorph.2014.02.005

Scott, T., Masselink, G., & Russell, P. (2011). Morphodynamic characteristics and classification of beaches in England and Wales. *Marine Geology*, *286*(1-4), 1–20. https://doi.org/10.1016/j.margeo.2011.04.004

Shepard, F. P. (1936). Undertow, rip tide or "rip current". *Science*, *84*(2173), 181–182. https://doi.org/10.1126/science.84.2173.181

Short, A. (1985). Rip-current type, spacing, and persistence, Narrabeen Beach, Australia. *Marine Geology*, *65*, 47–71.

Stockdon, H. F., Holman, R. A., Howd, P. A., & Sallenger, A. H. (2006). Empirical parameterization of setup, swash, and runup. *Coastal Engineering*, *53*(7), 573–588. https://doi.org/10.1016/j.coastaleng.2005.12.005

Suh, K., & Dalrymple, R. A. (1987). Offshore breakwaters in laboratory and field. *Journal of Waterway, Port, Coastal, and Ocean Engineering*, *113*(2), 105–121. https://doi.org/10.1061/(ASCE)0733-950X(1987)113:2(105)

Thomson, R. E. (1981). *Oceanography of the British Columbia Coast*. Department of Fisheries; Oceans.

Winter, G., Van Dongeren, A., De Schipper, M., & Van Thiel De Vries, J. (2014). Rip currents under obliquely incident wind waves and tidal longshore currents. *Coastal Engineering*, *89*, 106–119. https://doi.org/10.1016/j.coastaleng.2014.04.001

Young, I. (1995). The determination of confidence limits associated with estimates of the spectral peak frequency. *Ocean Engineering*, *22*(7), 669–686. https://doi.org/10.1016/0029-8018(95)00002-3